ABSTRACT

Title of Dissertation:	DIRECT NON-OXIDATIVE METHANE CONVERSION VIA H_2-PERMEABLE TUBULAR CERAMIC MEMBRANE REACTOR
	Mann Sakbodin, Doctor of Philosophy, 2019
Dissertation directed by:	Professor Dongxia Liu & Professor Eric Wachsman Department of Chemical and Biomolecular Engineering

Conversion of methane to higher hydrocarbons has the potential as the substitute for liquid petroleum in petrochemical and other chemical industries. Direct non-oxidative methane conversion (DNMC) reaction has attracted much attention given its unique capability to convert methane into C_2 (acetylene, ethylene, and ethane), aromatics, and hydrogen, while circumventing the intermediate energy intensive steps found in the conventional indirect "syngas" routes. In addition, DNMC has better atom efficiency compared to the indirect routes since CO_x products can be avoided. However, the main drawbacks of the DNMC reaction are due to the low methane equilibrium conversion, high endothermicity, and high rate of carbon formation.

This dissertation aims to development a novel catalyst/membrane system to circumvent the limitations of the DNMC reaction for the efficient and effective

hydrocarbons production. The single iron sites confined in the lattice of silica matrix (Fe/SiO_2) is an emerging methane activation catalyst for the DNMC reaction. By coupling the Fe/SiO_2 catalyst with the H_2-permeable tubular ceramic membrane reactor, part of the hydrogen produced from the DNMC reaction can be removed from the effluent gas, which shifts the equilibrium of the reaction to the product side, and in turn, increases the methane conversion. In addition, different sweep gases (H_2, air, O_2) can be used to promote different additional capabilities of the membrane reactors. The product distribution of the DMNC reaction can be tuned by either removing or adding H_2 to the DNMC reaction. Dual production of higher hydrocarbons and CO (or syngas) from two major global greenhouse gases can be achieved when CO_2 is used as the sweep gas. On one side of the membrane tube, CH_4 upgrading to C_{2+} hydrocarbons was realized via DNMC reaction over the Fe/SiO_2 catalyst, with co-production of H_2 gas. On the opposite side, the hydrogen permeate reacted with CO_2 sweep to form CO and H_2O via the RWGS reaction. Autothermal operation of the membrane reactor is potentially feasible by providing the heat required for the endothermic DNMC reaction from the heat released from the combustion of permeated H_2 when O_2 is used as sweep gas. In addition, a dual DNMC reactor and H_2-permeable membrane system was proposed in order to enhance the production of aromatics from CH_4, with pure H_2 as a beneficial byproduct. By recycling the effluent gas to the DMNC reactor after partial H_2 removal, in certain conditions, the aromatics yield reached >50%, which is significantly higher than single-pass results.

DIRECT NON-OXIDATIVE METHANE CONVERSION VIA H_2-PERMEABLE TUBULAR CERAMIC MEMBRANE REACTOR

by

Mann Sakbodin

Dissertation submitted to the Faculty of the Graduate School of the
University of Maryland, College Park, in partial fulfillment
of the requirements for the degree of
Doctor of Philosophy
2019

Advisory Committee:
Professor Dongxia Liu, Co-chair
Professor Eric Wachsman, Co-chair
Professor Ashwani Gupta
Professor Chunsheng Wang
Professor Chen Zhang

Acknowledgements

The completion of my research for this dissertation would be impossible without the assistance of so many people. First and foremost, I would like to thank my advisors, Dr. Dongxia Liu and Dr. Eric Wachsman, who guided me through my entire PhD career. I am truly grateful for their generosity in sharing their knowledge and insights with me.

I would like to thank the National Science Foundation (NSF-CBET 1264599 and 1351384), the Energy Innovation Seed Grant from the Maryland Energy Innovation Institute (MEI2), and the Harry K. Wells fellowship from University of Maryland Energy Research Center (UMERC) for the support of my research. I would also like to thank my committee members Dr. Ashwani Gupta, Dr. Chunsheng Wang, and Dr. Chen Zhang for their valuable time and contributions to my dissertation.

It has been an incredible experience working in both the Liu Research Group and the Wachsman Research Group at the University of Maryland. I'm grateful for the chance to work with so many wonderful colleagues. I would like to specially thank Su Cheun Oh, Wei Wu, Emily Schulman, Yi-Lin Huang, and Chris Pellegrinelli, whom I have shared ideas and encouragement throughout my PhD career.

Most of all, I would like to thank my family for their support and love throughout my life. They always have faith in me and encourage me to pursue my dreams.

To my late father and my family, this dissertation is dedicated.

Table of Contents

List of Tables

List of Figures

List of Abbreviations and Acronyms

DNMC – Direct non-oxidative methane conversion

FT – Fischer-Tropsch

OCM – Oxidative coupling of methane

GTL – Gas-to-liquid

MTO – Methanol-to-olefins

MTH – Methanol-to-hydrocarbons

MTA – Methanol-to-aromatics

TEM – Transmission electron microscopy

EXAFS – Extended X-ray absorption fine structure

BET – Brunauer-Emmett-Teller

WHSV – Weight hourly space velocity

TOS – time-on-stream

TGA – Thermal gravimetric analysis

SEM – Scanning electron microscopy

XRD – X-ray diffraction

PVB – Polyvinyl butyral

BBP – Benzyl butyl phthalate

PMMA – Poly(methyl methacrylate)

Chapter 1: Introduction

1.1 The abundance of methane

The depletion and the fluctuating prices of crude oil have led to the shift in the market attention to natural gas[1]. In addition, due to the advancement of the oil and gas extraction technologies, the production of natural gas has increased significantly in the past few decades.[2, 3] Methane, which is the main constituent of natural gas, is deemed to be an alternative source to replace crude oil for the production of value-added chemicals and fuel. Compared to crude oil and coal, methane is considered more environmental friendly source of fossil energy since it produces less carbon dioxide. Methane can be used as raw material for the production of light olefins and benzene, which are the important building blocks for wide range of commodities such as polymers, cosmetics and lubricants. Since large reserves of natural gas discovered recently are situated in remote areas, transportation of methane over a long distance through pipelines is therefore an issue since this process is not economically feasible. In addition, large quantities of natural gas are flared since it is cheaper to burn than to capture. However, this causes a huge waste in the world's natural gas resources. In addition, flaring process is also more environmental friendly compared to letting it escape to air since methane is a much stronger greenhouse gas than CO_2. Therefore, in order to properly utilize this valuable resource, new technologies and chemical processes need to be executed to convert methane into liquid fuels and chemical feedstocks such as olefin, aromatics and hydrogen.

The major challenge of methane activation lies on overcoming the rather strong C-H bond in methane, which requires approximately 439 kJ/mol of energy. Methane is a very stable compound of tetrahedral structure, with a melting point of 91.15 K and a boiling point of 111.7 K. It consists of perfectly symmetric zero dipolar and magnetic moments. Therefore, any chemical reactions will not be initiated without the presence of additional functional groups. Elevated temperature or introduction of oxidants is usually crucial to activate methane in the gas phase. Such reaction condition leads to mostly radical reactions with intrinsic low selectivity[4]. Furthermore, the possible products formed through methane conversion reactions are more reactive than methane since the strength of C–H bond in methane is stronger than in the possible products such as ethane or ethylene. Acceptable product selectivity are therefore only achieved at low/moderate conversion levels, which result in extensive recycling of unreacted methane and product separation. Even though catalysts play major role in lowering the activation energy of the chemical processes, extensive fundamental research and commercially viable technology remains elusive.

1.2 Current methane conversion pathways

Since methane is an abundant natural resource as the main constituent of natural gas and oil-associated gases, conversion of methane into higher hydrocarbons, oxygenates, or even more complex molecules is a long-standing challenge. Considerable efforts have been devoted to create methane activation pathways[5, 6]. **Figure 1.1** summarizes the current major CH_4 pathways being utilized, researched and developed, which include (i) indirect multi-step process involving conversion of methane to synthesis gas (a mixture of carbon monoxide (CO) and hydrogen (H_2),

known as syngas) followed by Fischer-Tropsch (FT) synthesis of higher hydrocarbons, (ii) direct oxidative coupling of methane (OCM) to C_2 such as ethylene (C_2H_4) and ethane (C_2H_6), and (iii) direct non-oxidative methane conversion (DNMC) into C_2 (e.g., acetylene (C_2H_2), ethylene, ethane) and aromatics (e.g., benzene (C_6H_6) and naphthalene ($C_{10}H_8$)), combined and referred to as C_{2+} hydrocarbons.

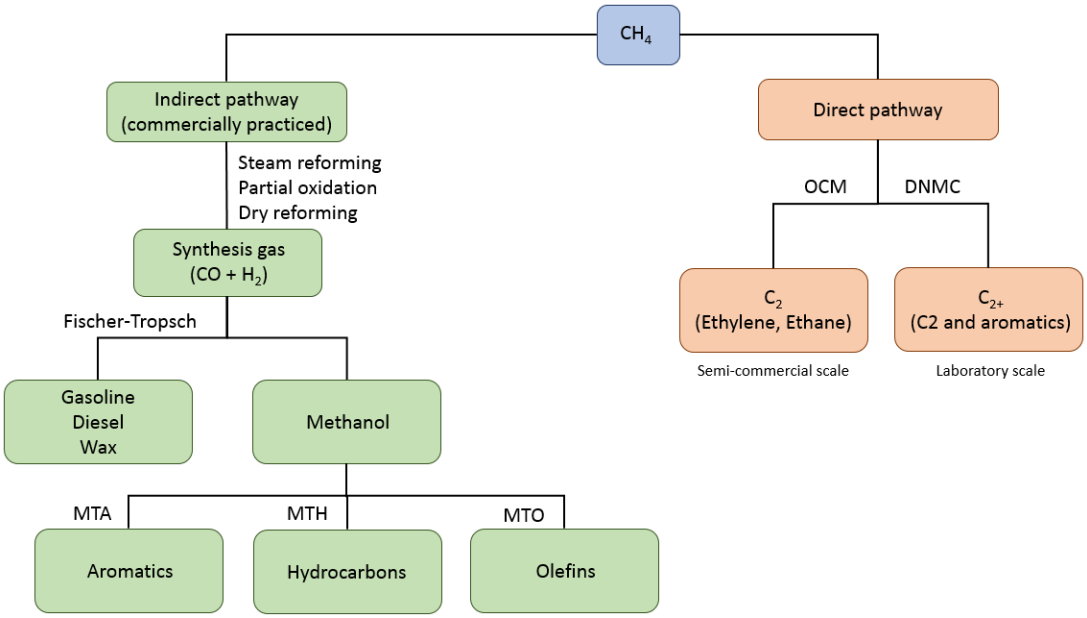

Figure 1.1. Overview of the selected direct and indirect methane conversion pathways.

1.2.1 Indirect methane conversion pathways.

Currently, the state-of-the-art process for the CH_4 upgrading process is an indirect multistep processes. CH_4 is first converted to synthesis gas (CO + H_2) via reforming reactions. Normally, CH_4 can be converted to synthesis gas via these three reforming reactions: (i) steam reforming of CH_4 (Eq. 1.1), (ii) partial oxidation of CH_4 (Eq. 1.2), and dry reforming of CH_4 (Eq 1.3)

$$CH_4 + H_2O \leftrightarrow CO + 3H_2 \qquad \Delta_rH° = +226\ kJ{\cdot}mol^{-1},\ \Delta_rG° = -71\ kJ{\cdot}mol^{-1} \qquad (1.1)$$

$$CH_4 + \frac{1}{2}O_2 \leftrightarrow CO + 2H_2 \quad \Delta_rH° = -44\ kJ{\cdot}mol^{-1}, \Delta_rG° = -254\ kJ{\cdot}mol^{-1} \tag{1.2}$$

$$CH_4 + CO_2 \leftrightarrow 2CO + 2H_2 \ \Delta_rH° = +261\ kJ{\cdot}mol^{-1}, \Delta_rG° = -73\ kJ{\cdot}mol^{-1} \tag{1.3}$$

Each reaction gives different H_2/CO ratio, therefore, the choices of synthesis gas production technology depends mainly on the downstream applications.[1] From the three reaction equations, it can be seen that the steam reforming of CH_4 gives the highest H_2/CO ratio of 3. Commercially, the steam reforming of CH_4 is the main reaction for synthesis gas generation. However, some downstream processes such as Fisher-Tropsch (FT) synthesis and methanol synthesis have the ideal H_2/CO of 2. Therefore, the H_2/CO ratio of the steam reforming has to be adjusted, which can be down via the water-gas-shift reaction. Synthesis gas obtained from the partial oxidation reaction has the ideal H_2/CO ratio of 2. However, the use of O_2 leads to completely oxidation of methane to CO_2 and H_2O, which lowers the overall synthesis gas yield. For dry reforming of CH_4, the synthesis gas produced has the H_2/CO ratio of 1, which is required for the synthesis of formaldehyde, polycarbonates, and the hydroformylation process. In addition, dry reforming also utilizes CO_2 as a reaction, which is a greenhouse gas.

The main products from CH_4 via the synthesis gas route have been ammonia and methanol.[1] Ammonia is a chemical feedstock used for the production of nitric acid and fertilizers. Synthesis gas can be further converted to fuels via the Fisher-Tropsch (FT) synthesis. The overall process is commonly known as gas-to-liquid (GTL) process.[7] The FT synthesis of higher hydrocarbons from syngas has been a well-established technology practiced commercially for decades to produce gasoline

and diesel, as well as waxes. Other alternative pathways of producing hydrocarbons via indirect GTL processes involves the conversion of synthesis gas to methanol, and then from methanol to chemicals via technologies such as methanol-to-olefins (MTO)[8], methanol-to-hydrocarbons (MTH)[9] and methanol-to-aromatics (MTA)[10]. Commercially, the CH_4 conversion pathway via synthesis gas dominates the industry. However, this process requires multiple steps, which results in high capital costs, low overall energy and carbon efficiencies. In addition, since it's an indirect process, the CO_2 emissions are high.

1.3 Direct non-oxidative methane conversion (DNMC) reaction

The expensive cost and inefficiencies of the indirect pathways have led to the search for more simple and efficient pathways for CH_4 to fuels processes. Direct methane conversion processes have been the subjects of academic and industrial interest for the past few decades[11-15]. These processes involve methane activation via the cleavage of a C-H bond, followed by reactive intermediates coupling to form fuels and chemicals in a single catalytic reactor unit. Therefore, direct CH_4 conversion paths can potentially reach higher energy and carbon efficiencies when compared to the synthesis gas route. The direct CH_4 conversion pathways are divided into 2 different categories, oxidative and non-oxidative pathways. One of the most studies oxidative pathways in the oxidative coupling of methane (OCM) reaction. OCM reaction directly converts CH_4 into hydrocarbons, especially C_2 (ethylene and ethane), in the presence of an oxidant, which is normally oxygen. Ethylene is one of the most important feedstocks for many of the petrochemical products.[1] OCM reaction has become one of the most widely studied reaction for methane activation, which could provide an

alternative to traditional ethylene synthesis processes such as naphtha pyrolysis and ethane dehydrogenation. However, methyl radicals can also undergo deep oxidation via the reaction with adsorbed diatomic oxygen species and gas phase molecular oxygen to produce CO_2 and CO, respectively. The main challenge of OCM reaction is that the more reactive nature of C_2 products compared CH_4 leads to the sequential oxidation of C_2 to thermodynamically more favored CO_x (CO or CO_2) products. The attainable C_2 yield in OCM is limited to 28% under fixed-bed, continuous-feed reaction conditions[16]. Additionally, the development of cost-effective and robust membrane separation technologies are needed to significantly improve the economic competitiveness of OCM to ethylene product[17].

In comparison to the synthesis gas pathway and OCM reaction pathway, the direct non-oxidative CH_4 conversion (DNMC) pathway is a more selective approach to upgrade CH_4 into higher hydrocarbons given its capability in forming C_{2+} hydrocarbons and H_2 while circumventing the intermediate energy intensive steps of the synthesis gas route. The DNMC has been studied under non-catalytic conditions for more than a century[18, 19] . The reaction often takes place at temperature above 1400 K, with acetylene as the dominant product and is accompanied by high coke formation[13, 20-23]. The homogeneous DNMC process has been proposed to exhibit three kinetic stages:

(i) an induction period, during which methane conversion is limited by slow initiation steps ($CH_4 \rightarrow CH_3\cdot + H\cdot$),

(ii) (a chain transfer regime as $CH_3\cdot$ and $H\cdot$ radicals accumulate and reach pseudo steady-state and within which most of the methane conversion occurs, and

(iii) a near-equilibrium stage within which most elementary steps become unproductive as they reach thermodynamic equilibrium[23, 24].

However, the rates of the first two steps are insufficient for practical methane reaction rates. Therefore, catalysts have to be considered to increase the induction and chain transfer rates to overcome kinetic barriers in DNMC process. Among the experimental and theoretical studies for catalytic DNMC pathway, molybdenum loaded Zeolite Socony Mobil-5 (Mo/ZSM5) has been the most efficient catalyst since the pioneering work by Wang et al.[25] The mechanism of methane activation over Mo/ZSM5 catalysts has been debated since then[1, 26, 27]. The most widely accepted one involves a bifunctional mechanism with participation of both Mo sites and Brønsted acid sites.

A required induction period takes place at the beginning of the DNMC reaction, where molybdenum is gradually transforming into molybdenum carbide or oxycarbide species upon reduction by CH_4. Methane is first activated on Mo sites (Mo_2C) to form surface CH_x species after the release of hydrogen to the gas phase, and then the products of their dimerization (C_2H_y) are subjected to oligomerization on the zeolite Brønsted acid sites to form benzene and other aromatics, as illustrated in **Figure 1.2**. Active sites activate methane within shape-selective zeolite environments that restrict chain growth and the formation of polynuclear aromatics. Benzene selectivity as high as 80% has been reported at near-equilibrium conversion on Mo/ZSM5 catalysts. However, the one of the major drawbacks of the DNMC reaction is the deactivation due to coke formation. Coke is formed via two pathways: (i) dehydrogenation of C_2Hy intermediates in series with aromatics formation step and (ii) dehydrogenation of

methane (CH_x) in parallel with C-C bond formation step. Further oligomerization of aromatic products could lead to the deposition of heavy polyaromatics-type carbon deposits (hard coke) on the Brønsted acid sites whereas continuous, deep dehydrogenation of CH_x and aromatic compounds could yield the formation of amorphous coke (soft coke).

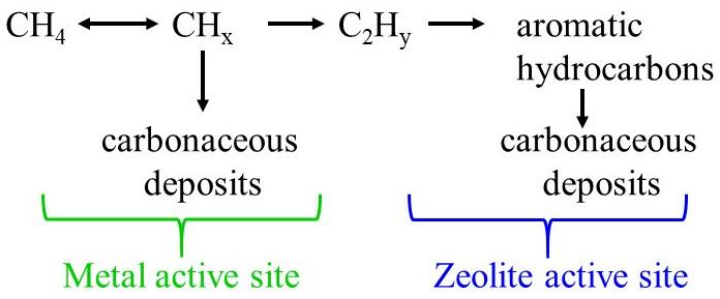

Figure 1.2. Proposed mechanism for DNMC over Mo/ZSM5 bifunctional catalyst.

1.3.1 Challenges in direct non-oxidative methane conversion (DNMC) reaction

The main challenges for the commercialization of the DNMC process is the thermodynamic limitation of the reaction. **Figure 1.3** shows the thermodynamic parameters, i.e., Gibbs free energy of reaction (Δ_rG) and equilibrium conversion, of methane upgrading to ethylene or benzene via the DNMC process. The formation of carbon (C) and hydrogen from methane conversion is also included for comparison. From **Figure 1.3**, by comparing the Δ_rG among these three reactions, carbon formation is more thermodynamically favorable compared to the main products of DNMC like ethylene and benzene. Another limitation of the DNMC process is the deactivation of the catalyst due to coke formation. As the carbonaceous product deposits on the surface of the catalyst, the active sites are blocked, which eventually causes the catalyst

deactivation**. Figure 1.3** shows the equilibrium CH_4 conversion for the formation of ethylene, benzene, and carbon. The products of DNMC such as ethylene and benzene show significantly lower CH_4 conversion compared to carbon even at extreme temperatures. Therefore, the reaction conditions have to be properly controlled in order to minimize the carbon formation. Additionally, methane conversion in the DNMC pathway is a highly endothermic process. The high coke selectivity in product formation, low equilibrium methane conversion, and high temperature endothermicity are three major challenges in DNMC technology.

From the reaction stoichiometry, the DNMC reaction results in the formation of H_2 as by-product since the larger hydrocarbons are formed from CH_4. For example, 2 mol H_2/1mol of C_2H_4 and 9 mol H_2/1 mole of C_6H_6 are formed, respectively. Since the number of moles of products are higher than the number of moles of reactants, the DNMC pathway favors low pressure and is limited by the equilibrium conversion.

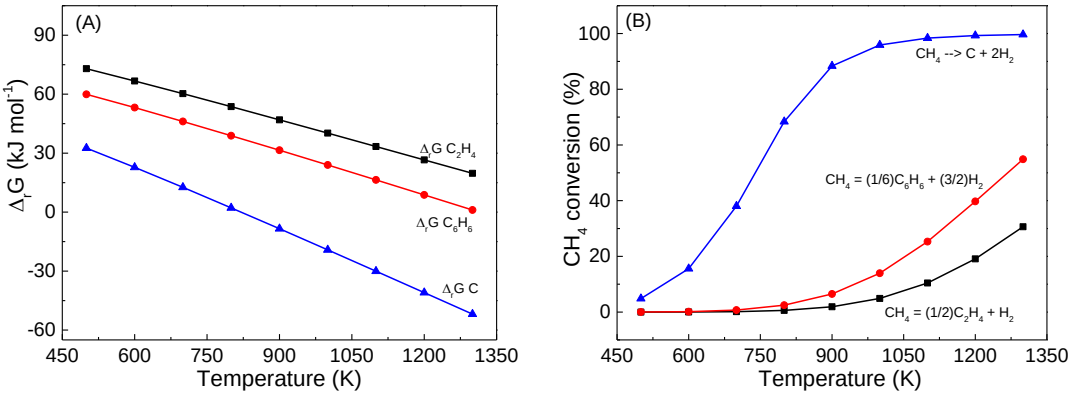

Figure 1.3. Gibbs free energy of reaction ($\Delta_r G$) for the formation of ethylene, benzene and carbon, respectively, from methane in DNMC (A) and equilibrium methane conversion in these reactions (B).

One of the strategies to circumvent the thermodynamic limitation in order to enhance the CH_4 conversion is to take advantage of the Le Châtelier's principle. By

removing H_2 from the effluent of the DNMC reaction, the equilibrium will be shift toward the product side, which will enhance the CH_4 conversion. Therefore, by coupling the DNMC catalyst with a H_2-permeable membrane to form a reactive-separative membrane reactor, the CH_4 conversion can be improved. In addition, pure H_2 can also be produced as by-product from the membrane reaction separation. **Figure 1.4** illustrates the effects of H_2 removal on methane conversion enhancement in DNMC. Methane conversion as high as 100% can even be achieved at mild temperature conditions as long as the formed hydrogen can permeate effectively from the effluent of the DMNC reaction through the membrane reactor. Because of the promising theoretical analysis results, research efforts have been devoted to the development of the DNMC pathway in the 2000s[28-30]. The experimental results did show the increase in methane conversion and hydrocarbon formation, but conversion was still lower than that predicted from theoretical analysis[31, 32]. The experimental results also showed that H_2 removal accelerated catalyst deactivation[31, 33]. In recent years, research efforts have been focused on mitigating the low methane conversion and catalyst deactivation in membrane reactors by application of oxygen permeable membranes[34, 35], design of hollow fiber membranes[36, 37], or employment of coke resistant catalyst[38].

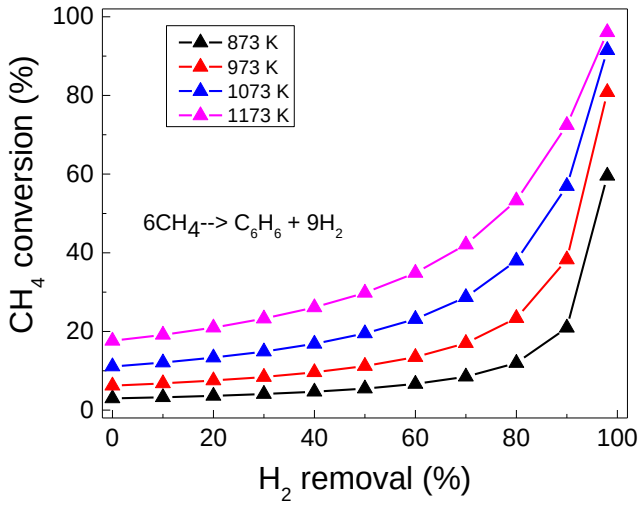

Figure 1.4. Enhancement in methane conversion to benzene and hydrogen due to equilibrium shift driven by hydrogen removal according to Le Châtelier's principle.

1.3.2 Catalysts for DNMC reaction

1.3.2.1 Metal/zeolite catalyst. Zeolites are crystalline aluminosilicates with various structures, pore connectivity, and framework compositions with typical pore sizes of less than 2 nm[39-41]. In chemical and petrochemical industries, zeolites have been widely utilized in adsorption, separation, and catalytic processes[42-46]. The conversion of CH_4 via the DNMC pathway utilizing zeolite-based catalysts was first reported by Wang et al using the Mo/ZSM5 catalyst[25]. The discovery of the Mo/ZSM5 catalysts has let to research interest to explore their structure-function relationships in DNMC chemistry during the past years. A range of experimental and theoretical studies have been conducted over this catalyst system since its first report.

Given the diversity of metal types and zeolite framework structures, a lot of different catalyst formulations have been investigated for DNMC reaction. Among all the studied metal/zeolite catalysts, ZSM5 and Mobil Composition of Matter No.22

(MCM22) are by far the most widely studied zeolite materials for this reaction. Even though a number of metal ions dispersed on zeolite to introduce bifunctionalities to the catalysts have been tested for the reaction (including Cr, Fe, Mo, W, Re, Zn, Cu, Ga, etc.), Mo remains the most active and selective catalyst for DNMC reaction, followed by Zn and W. In order to improve the catalyst performance and stability in DNMC reaction, a second metal can be incorporated as additives to the metal/zeolite catalysts. The effects of noble metals (Pt, Pd, Rh, Ru, Ir and Re) and transition metals (Fe, Ni, Zn, Co, Cr, W) addition have been evaluated.

On the basis of these studies, the following structure-function relationships in Mo/ZSM5 catalysts can been obtained: (i) the medium-pore zeolites like ZSM5 with a pore system consisting of two types of intersecting straight and zig-zag channels without large cavities favors the synthesis of small aromatic molecules but prevents accumulation of polycondensed aromatic substances. As a comparison, the small pore zeolites such as SAPO-34 hamper diffusion of aromatic molecules, while large pore materials like zeolites FAU are active in accumulating carbonaceous deposits[47-49]; (ii) The Mo species are dispersed in the zeolite support, and are converted into Mo carbide or Mo oxycarbide in the induction period of the DNMC reactions; and (iii) C/Mo of ~10 is noted for methane pyrolysis on Mo/ZSM-5 by Weckhuysen and Lunsford on the basis of X-ray photoelectron spectroscopy studies[50, 51] and a ratio of ~7-10 C/Mo ratio has been reported by Iglesia and coworkers[27, 52] for catalysts operating at 3 h on-stream. These fundamental understanding forms the basis for the choice of feed composition or reactor type for optimization of DNMC reactions over Mo/ZSM5 catalysts in DNMC chemistry. By going through all the studies in membrane

reactors, Mo/ZSM5 is the most widely used catalyst, similar to that in fixed-bed reactors. The coking of catalyst in membrane reactors, however, is severer due to hydrogen removal. The variation of catalyst composition or constitution to improve Mo/ZSM5 performance in membrane reactors has not been reported, but the fundamentals and experiences gained from the fixed-bed reactor conditions can be applied to membrane reactor cases to assist such studies in the future.

1.3.2.2 Iron/silica catalyst. The conventional metal/zeolite catalyst for DNMC reaction typically occur at the temperature below 1023 K due to the instability of the catalyst structures, which limited the CH_4 conversion (~16% at 1023 K) and led to the fast deactivation of the catalysts[5, 12, 53, 54]. This has led to the search for more efficient DNMC catalysts with higher CH_4 conversion and less coke formation. The iron/silica (Fe/SiO_2) is such a catalyst effective in the DNMC reaction discovered by Bao et al[55]. In comparison to the Mo/ZSM5 catalysts or non-catalytic CH_4 pyrolysis, the DNMC over Fe/SiO_2 catalyst operates at the temperature range between 1173 - 1373 K, which lies between the operation ranges of Mo/ZSM5 and non-catalytic pyrolysis, producing ethylene and aromatic products with negligible coke formation when reaction temperature and space velocity are properly controlled. The product in DNMC over Fe/SiO_2 contains ~50% ethylene, ~20% benzene and ~30% naphthalene, and the methane conversion reaches up to ~48%.

Characterization technique such as TEM has shown that the iron oxide nanoparticles in the size ranges from 3 nm to 4 nm distributed homogeneously throughout the fresh catalyst. Upon catalyst activation in the reaction atmosphere, coordinatively unsaturated iron sites was formed and acted as active sites for C-H bond

breakage. **Figure 1.5(A)** shows the embedment of iron oxide species within the silica matrix through bonding of C and Si atoms. Extended X-ray absorption fine structure (EXAFS) data also verify that the iron species is confined in silica lattices where they are coordinated to a Si atom and two C atoms (**Figure 1.5(C)**). The isolation of the iron atoms in the silica matrix through bonding of Si and C atoms achieves high selectivity toward hydrocarbons and prohibits coke formation under extreme temperature conditions. The Fe/SiO_2 catalyst contains 0.5 wt % of Fe and its BET surface area is < 1 m^2/g.

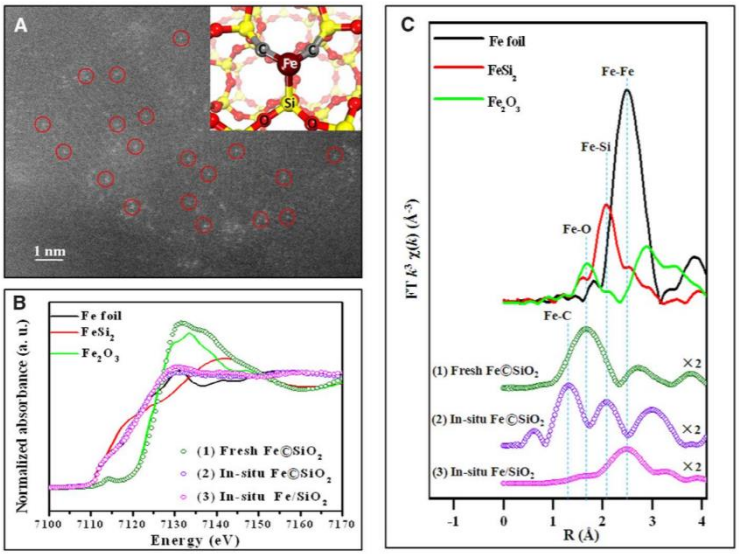

Figure 1.5. (A) STEM-HAADF image of spent Fe/SiO_2 catalys, (B) in-situ XANES of the Fe/SiO_2 catalyst upon activation and (C) Fourier transformed (FT) k^3-weighted χ(k)-function of the EXAFS spectra for Fe/SiO_2 catalyst. (Reproduced with permission from reference 55. Copyright 2014 the American Association for the Advancement of Science.)

1.4. Membrane reactor for non-oxidative methane conversion

The membrane reactor comprised of a methane activation catalyst and a H_2-permeable membrane is the viable solution to shift the thermodynamic equilibrium to enhance methane conversion in DNMC pathway. There are a wide range of membrane materials available for the separation of hydrogen from a mixture of other gases. Mainly, these materials include polymer membranes (e.g., Nafion), nanoporous ceramic membranes, dense metal membranes, and dense mixed ionic-electronic conductive (MIEC) ceramic membranes. Since DNMC has been mainly studied under very high temperature (typically, above 873 K) conditions[25, 26, 30, 31, 52], this prevents the consideration of polymer membrane as a candidate for the hydrogen separation in DNMC process. In addition, it should be noted that polymer membranes often have low separation factor, and thus it is very difficult to obtain high purity hydrogen from the reactor system[56]. As for nanoporous ceramic membrane materials, although there is a small range of temperature overlap, the main drawbacks are in the fabrication process. It is very difficult to fabricate thin defect-free membranes with a discrete pore structure in order to achieve high flux and large separation factor. The separation mechanism determines that the nanoporous membranes not only allow hydrogen to diffuse through, but also allow feed gas and desired products to pass through. Therefore, high purity of hydrogen in the permeate side of the membrane reactor is hard to achieve. Therefore, the two main types of membranes considered for DNMC reaction are dense metal membranes and MIEC ceramic membranes.

1.4.1 Different types of hydrogen-permeable membrane

1.4.1.1 Palladium membrane. The knowledge of hydrogen diffusion through palladium (Pd) has been known since the 1800s[53]. Membranes made of certain metals, such as Ni, Pd and Pt, have the capability to dissociate and dissolve hydrogen. However, only Pd membrane has the ability to transport hydrogen through the metal. This is because Pd has a much higher hydrogen solubility compared to other metals[57]. Therefore, Pd and Pd-alloy metal membranes have been promising candidates for hydrogen removal from a mixture of gases[53, 58], including hydrogen removal from DNMC in membrane reactors[59-61]. Different from nanoporous polymer or ceramic membranes, the dense Pd metal membranes can produce high purity hydrogen from the separation process.

The effective H_2 flux (J_{H_2}) through Pd-based membranes is governed by Sieverts Law[58], which can be expressed as

$$J_{H_2} = \frac{P}{L}\left(p_{H_2,1}^{n} - p_{H_2,2}^{n}\right) \quad (1.5)$$

where P represents the permeance (mol m^{-2} s^{-1} Pa^{-n}), L represents membrane thickness, $p_{H_2,1}$ and $p_{H_2,2}$ represent hydrogen partial pressure of the feed and permeate sides, respectively. The ideal value of n is 0.5. However, defects such as pinholes and micro-cracks can influence the value of n, which cause n to increase. In addition, hydrogen selectivity also decreases with formation of defects. The mechanism for the hydrogen transport proceeds in the following steps: (i) adsorption and dissociation of H_2 on the surface of the membrane to form H^+; (ii) dissolution of H^+ into the matrix of the Pd-based membranes; (iii) diffusion of the H^+ and through the membrane; and (iv)

recombination of H^+ and to form H_2 and desorption of H_2 molecules. Since hydrogen has to be dissociated before it can be transported through the dense Pd-based membrane, there is a possibility that the hydrogen transport is limited by the dissociation reaction on the surface. However, it is generally assumed that bulk diffusion dominates the overall hydrogen transport.

Pd-based membranes have a unique ability to permeate hydrogen. However, they suffer from some limitations. Firstly, absorption of hydrogen below its critical point (571 K and 2 MPa) results in two different phases, α and β. While both phases retain the pure Pd fcc phase, the crystal unit cell lattice parameter for the two phases are different[57]. This change in volume as a result of phase transformation can lead to strain and recrystallization, which in turn give rise to membrane defects[58]. Secondly, exposure to hydrogen can lead to a process called hydrogen embrittlement, where Pd loses its ductility[62]. Hydrogen embrittlement can result in membrane cracking[62]. Finally, Pd can react strongly with carbon-containing species[63], sulfur[64], or carbon monoxide[64], which deactivates the surface of the membrane. Pd can be alloyed with other metals in order to prevent phase transformation, and lessen the hydrogen embrittlement, and poisoning issues[65-70]. But still, in order to have Pd membranes as a viable option for hydrogen removal from DNMC process, reasonable membrane cost, resistance to coking and high hydrogen flux under extreme temperature conditions are required.

1.4.1.2 Dense MIEC ceramic membrane. Given the reaction temperature of DNMC, the H_2-permeable membrane materials should be thermally and chemically stable at temperature above 873 K, dense MIEC ceramic membranes are the best candidates

compared to other types of membranes. Dense MIEC ceramic membranes have the best temperature match (i.e., temperature required for hydrogen separation) with the temperature needed for the state-of-the-art DNMC catalyst activation. For MIEC ceramic membranes, hydrogen is conducted through the membrane electrochemically[56, 71, 72]. First, hydrogen is dissociated, and ionized to form the hydroxide defects (proton defects), which migrate through the membrane via proton hopping between adjacent oxygen ions at normal lattice sites via the Grotthuss-type mechanism[73]. At the permeate side of the membrane, the defects are then reduced to form hydrogen molecules and desorbed from the membrane surface. Based on the Wagner equation[74],

$$J_{OH_O^{\cdot}} = -\frac{1}{L}\left[\frac{RT}{2F^2}\int_{P'_{H_2}}^{P''_{H_2}} \sigma_{amb}\, d\ln P_{H_2}\right] \quad (1.6)$$

, four different parameters affect the hydrogen permeation ($J_{OH_O^{\cdot}}$ is flux of the hydroxide ion) through the membrane, which include hydrogen partial pressure gradient across the membrane (P'_{H_2} and P''_{H_2} stand for the H_2 partial pressure on both sides of the membrane), membrane thickness (L), ambipolar conductivity of the membrane material (σ_{amb}), and operating temperature (T). R and F are gas constant and Faraday constant in the equation. Since the membrane can only conduct hydroxide defects, the biggest advantage of this type of membrane is 100% selective for hydrogen. To be suitable for H_2 separation, the membrane material must contain both ionic and electronic conductivity in order to maintain electroneutrality. In order to maximize the hydrogen permeation, the ionic and electronic transference numbers should be comparable. At high temperatures, these materials can also transport oxygen ions. The

absence of external circuit, unlike a fuel cell that requires an external circuit for the movement of electrons, simplifies the membrane reactor design and operation, as well as cost and energy.

One type of the most promising dense MIEC ceramic materials for hydrogen permeation is perovskite-type oxides. These are the materials with the general formulation ABO_3 (shown in **Figure 1.6**), where the A site is occupied by an alkaline earth, alkaline and lanthanide element, such as Ba, Sr, and Ca, while the B site is occupied by tetravalent element, such as Ce and Zr[75]. Realistically, perovskite exists as $ABO_{3\pm\delta}$ where δ represents oxygen anion excess or deficient, depending on the total valence amount of A-site and B-site cations. The total positive valence of A and B cations is equal to 6 (the total negative valence of oxygen anions). Generally, A-site cation is larger in size (0.11-0.18 nm) compare to B-site cation, which is medium in size (0.062-0.100 nm). To promote electronic conductivity, aliovalent metals such as Y, Yb, Pr, Eu, Gd can be doped to the B-site of the perovskite materials. For example, $SrCeO_3$ does not have high electronic conductivities, but can be increased significantly by substituting Ce^{4+} with aliovalent ions (Y, Yb, Gd and Eu)[56, 76]. The partial substitution of the B-site cation with a trivalent dopant M results in the creation of oxygen vacancies, which is very important for proton conductivity[77-79]. Oxygen vacancies are created in order to balance the charges from the M dopant. In Kroger-Vink notation[72], the substitution can be written as

$$2B_B^X + O_O^X + M_2O_3 \leftrightarrow 2M_B' + V_O^{\cdot\cdot} + 2BO_2 \quad (1.7)$$

, where $B_B^X, O_O^X, M_2O_3, M_B', V_O^{\cdot\cdot}, BO_2$ stands for B-site ion in a B-site ion lattice, oxygen ion in an oxygen ion lattice, trivalent metal oxide, trivalent metal ion in a B-site ion lattice, oxygen vacancies, and B-site metal oxide. Ambipolar conductivity of $SrCeO_3$ increases with Eu dopant in the B-site.

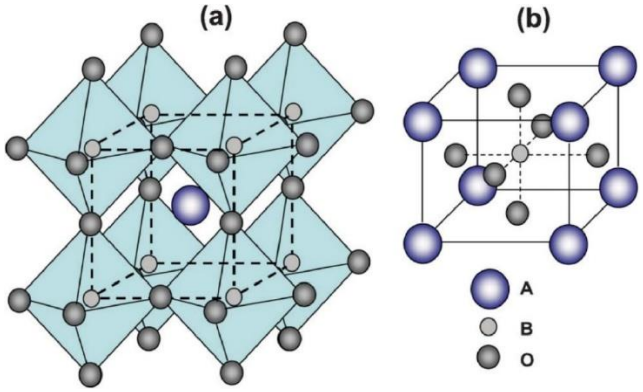

Figure 1.6. The structure of perovskite ABO_3. (a) Corner-sharing (BO_6) octahedral with A ions located in 12-coordinated interstices. (b) B-site cation at the center of the cell. (Adapted from reference 75 with permission from The Royal Society of Chemistry)

In addition to the high ambipolar conductivity, to be commercially useful as H_2 separation membranes, the perovskite oxides should be stable at the operating conditions. The defect chemistry of the doped ABO_3 can be very complex due to the possibility that the dopant M can also goes into the A-site, not the B-site as intended[72]. When metal M goes into the A-site instead of the B-site, oxygen vacancies are consumed instead of being created[80, 81], which is detrimental for proton conduction. Several experimental studies and simulations have shown that A-site substitution occurs preferentially using cations with relatively large ionic radius[82-85]. Lattice distortions resulted from doping can also influence the conductivity of the perovskites as well. Doping cations with ionic radius significantly

larger than the host B-site metal, or doping with high dopant concentrations can have a significant impact on the conductivity performance of the materials[86]. In general, when metal M is doped into a perovskite structure, the difference in ionic radius results in strains to the overall structure, which in turn changes the volume of the unit cell. Therefore, it can be stated that the change in unit cell is the measurement of the strain applied to the structure resulted from doping. Goldschmidt tolerance factor (t) is given by:

$$t = \frac{(R_A + R_O)}{\sqrt{2}(R_B + R_O)} \tag{1.9}$$

is an equation that is used to describe the extent of distortion from the ideal cubic perovskite structure, where R_A and R_B are the ionic radii of the A-site and B-site cations, and R_O is the ionic radius of oxygen. When $0.75 < t < 1.0$, stable perovskite structures can be obtained. For cubic perovskites, the t values generally fall between 0.95 and 1.04. For orthorhombic perovskites, the t values usually range from 0.75 to 0.9[87]. For example, partial substitution of Zr for Ce in $SrCeO_3$ can improve its chemical stability, which is attributed to the higher stability of $SrZrO_3$ against CO_2[72, 88].

Protons are normally incorporated in the perovskite structure as hydroxide defects. These hydroxide defects are created in the presence of water vapor and/or hydrogen-containing gases. In the presence of water, the formation of protonic defects is based on the dissociative adsorption of water reaction. In Kroger-Vink notation, the reaction is given by:

$$H_2O + V_O^{\cdot\cdot} + O_O^X \leftrightarrow 2(OH)_O^{\cdot} \tag{1.10}$$

In this reaction, water in the gas phase is dissociated into a proton and a hydroxide ion. The hydroxide ion will fill the oxygen vacancy, while the proton will form a covalent bond with the lattice oxygen. In the dry hydrogen atmosphere, the hydroxide ion is formed according to the reaction

$$H_2 + 2O_O^X \leftrightarrow 2(OH)_O^{\cdot} + 2e' \quad (1.11)$$

In practice, humidified gases, either in the feed side or permeate side of the membrane reactors are used in order to improve proton conduction, and thus hydrogen permeation in separation applications[71, 72, 81].

Normally, in a H_2-free and water vapor-free environment, $BaCeO_3$-based and $SrCeO_3$-based materials are p-type conductors. However, in the presence of hydrogen and water vapor, $SrCeO_3$ is a protonic conductor with high protonic conductivity and relatively low electronic conductivity. However, the most crucial issue dealing with $SrCeO_3$ and $BaCeO_3$ is their low chemical stability in the presence of acidic gases and water vapor. For example, in the presence of CO_2, CO_2 can react with $SrCeO_3$ and $BaCeO_3$ to form carbonates, hydroxides can be formed in the presence of water vapor. Degradation of the membrane would lead to a lower rate of H_2 permeation. Compared to cerates, $BaZrO_3$ and $SrZrO_3$-based oxides are more chemically stable. However, zirconates require much higher sintering temperatures in order to achieve dense structures free of pores. In addition, the conductivity of zirconates are generally lowered in comparison to cerates. This is the consequence of poor conduction of grain boundary regions. Zirconates have poor sinterability, which result in small average

grain size, and therefore, contain large grain boundary volume content, which have lower conductivity compared to inside the grains.

To be commercially useful as H_2 separation membranes, the perovskite oxides should have both high electronic and protonic conductivity, and be stable at the operating conditions. For example, while the electronic conductivities of $SrCeO_3$ is relatively low, it can be increased significantly by substituting Ce^{4+} with aliovalent ions (Y, Yb, Gd and Eu). The oxygen vacancies, typically created by acceptor doping to maintain electroneutrality, play an important role for proton conduction. Another advantage of perovskites is that these materials have the ability to conduct both protonic defects and electrons in a single phase. To be suitable for H_2 separation, a membrane material must have comparable protonic and electronic transference numbers. In addition, the proton transference number must be much higher than the transference number for oxygen ion. For example, ambipolar conductivity increases with Eu dopant in the B-site. In addition, partial substitution of Zr for Ce can improve the chemical stability of $SrCeO_3$ which is attributed to the higher stability of $SrZrO_3$ against CO_2

1.4.2 DNMC in Pd-based membrane reactors

The initial attempt to study DNMC reaction in Pd-based membrane reactor was started in 1989 by using a tubular membrane and Pt-Sn/Al_2O_3 catalyst[28]. The DNMC performance was not encouraging due to severe coke formation in the reactor system. The emergence of Mo/ZSM5 catalyst for DNMC in 1993 sparked new research interest for Pd-based membrane reactors in the early 2000s. As summarized in **Table 1.1**, several research groups reported the coupling of Mo/ZSM5 catalysts with Pd or Pd-

alloy membranes in an attempt to circumvent thermodynamically limited methane conversion. Both disk-shaped and tubular Pd-based membranes were tested. Tubular Pd-based membranes were rather popular since they are available commercially. The metal/zeolite catalyst formulations were slightly different across all these studies. Overall, the following results have been consensually reported: (1) methane conversion and C_{2+} yield were improved in Pd-based membrane reactor compared to fix-bed reactor without in-situ hydrogen removal; (2) up to ~75% hydrogen produced from the DNMC reaction was selectively removed by the Pd-based membranes; and (3) carbon deposition on the membrane reactors significantly decreased the hydrogen flux of the Pd-based membranes.

Table 1.1. Overview of the catalyst and Pd-based H_2-permeable membrane reactor types used for DNMC reactions in literature.

Membrane type	Catalyst and reaction condition	Membrane geometry/dimension	Performance	Year/ Reference
Pd membrane	Temperature: 400 K Pressure: ~ 101 kPa Catalyst: Pt-Sn/Al_2O_3	Tubular (5 mm outer diamter x 0.3 mm thickness x 1000 mm length)	CH_4 conv.: < 1.0% Selectivity: coke and trace of C_2 H_2 removal: N/A	1989 [[28]]
Pd-coated alloy membrane	Temperature: 773-873 K Pressure: ~ 1 atm Catalyst: 0.5% Ru-3% Mo/ZSM5	Tubular (2.38 mm outer diameter x 178 mm length, unknown thickness)	CH_4 conv.: 2.5% Selectivity: highly selective toward benzene H_2 removal: up to ~210 mL STP min^{-1} H_2 permeation rate	2001 [[59]]
Pd-Ag alloy membrane	Temperature: 858 K Pressure: ~ 101 kPa Catalyst: Re/ZSM5 and Mo/ZSM5	Tubular (3.175 mm outer diameter x 177.8 mm length, unknown thickness)	CH_4 conv.: 7.5% Selectivity: > 95% aromatics H_2 removal: 75% removed	2001 [[60]]
Pd-Ag alloy membrane	Temperature: 873-973 K Pressure: ~ 101 kPa Catalyst: 0.5% Ru−3% Mo/ZSM5	Tubular (9.5 mm outer diameter x 70 mm length, unknown thickness)	CH_4 conv.: ~17% Selectivity: increased coke H_2 removal: N/A	2002 [[61]]

Pd-coated Ta/Nb alloy membrane	Temperature: 873 K Pressure: ~ 101 kPa Catalyst: 0.5% Ru−3% Mo/ZSM5	Tubular (2.38 mm outer diameter x 178 mm length, unknown thickness)	CH_4 conv.: < 12% Selectivity: increased coke, highly selective toward benzene H_2 removal: up to ~200 mL STP min^{-1} H_2 permeation rate	2002 [[89]]
Pd-Ag alloy membrane on porous stainless steel support	Temperature: up to 973 K Pressure: ~ 101 kPa Catalyst: 0.5% Ru−3% Mo/ZSM5	Tubular (9.5 mm outer diameter x 0.005 mm thickness x 70 mm length)	CH_4 conv.: ~17% Selectivity: increased coke, highly selective toward benzene H_2 removal: up to ~0.0016 m^3 STP m^{-2} s^{-1} H_2 permeation rate	2003[[90]]
Pd membrane	Temperature: 883 K Pressure: ~ 101 kPa Catalyst: 3 wt% Mo/ZSM5	Disk (20 μm thickness)	CH_4 conv.: 5-8% Selectivity: increased by 2-10 times for aromatics H_2 removal: 50-60%	2003 [[91]]
Pd tubular membranes	Temperature: 973 K Pressure: ~ 101 kPa Catalyst: 4 wt% Mo/ZSM5	Tubular (6.6 mm outer diameter x 0.125 mm thickness x 46.4 mm length)	CH_4 conv.: ~10% Selectivity: ~80% benzene H_2 removal: 6.8-48.3% H_2 recovery	2015 [[92]]

After the feasibility demonstration of Pd-based membranes for hydrogen removal from DNMC, the research was focused on the understanding of the mechanism and process control of DNMC in membrane reactors to optimize performances. For example, Larachi et al.[61] studied the types of coke formed on the catalyst (3wt% Mo-0.5wt% Ru/ZSM5) in the membrane reactor at the temperature range of 873 K-973 K. It was found that three types of carbon (carbidic, graphite-like and aromatic-aliphatic species) were formed. The H/C ratio of the carbonaceous deposits in the membrane reactor was lower than that in the fix-bed reactors without hydrogen removal. The chemical states of carbon and molybdenum on the metal/zeolite catalyst was not influenced by hydrogen removal. The catalyst can be regenerated when exposed to a

mixture of CH_4/H_2 for a short period of time in order to recover the coke-deactivated sites. Later on, Larachi's group studied the strategy of improving membrane permeability and mechanical stability by placing Pd-Ag membrane on porous stainless steel via electroless plating.[59, 61, 93] The results showed that a significant increase in methane conversion was achieved at 973 K, reaching levels well beyond the thermodynamic conversion, but followed by a quite sharp decrease. It was concluded that carbonaceous species were formed under very low hydrogen pressure and high reaction temperature, which negatively affected mainly the catalyst activity. Additionally, the method for removal of hydrogen permeate in the membrane reactor system has also been tested. Most cases, inert gas flow was used to carry away the hydrogen permeate to form a hydrogen-inert gas mixture. Wang et al.[60] reported the use of a vacuum pump to remove permeated hydrogen, which can produce pure hydrogen from DNMC reaction in the membrane reactor.

In order to balance methane conversion, product selectivity, coke formation as well as hydrogen removal, Natesakhawat et al.[92] carefully studied effects of WHSV on the DNMC in a Pd membrane reactor coupled with 4wt% Mo/ZSM5 catalyst. The membrane reactor performance was investigated as a function of WHSV ranged from 750 to 9000 mL g_{cat}^{-1} h^{-1}, at 973 K and 101 KPa pressure. It reported that CH_4 conversion and aromatic product yield decreased with increasing WHSV. The H_2 recovery was also negatively influenced with increasing WHSV, dropped from 48.3% to 6.8%. At intermediate WHSV (3000 mL g_{cat}^{-1} h^{-1}), a trade-off between catalytic activity and hydrogen recovery existed, which resulted in the maximum enhancement (~360%) in benzene yield. At this intermediate WHSV, the largest concentration of

hydrogen was found in the retentate stream and helped alleviate coke accumulation, particularly on ZSM5 zeolite. It was also found that the carbon deposited on the inner surface of the membrane reactor portion in contact with the catalyst bed and transported to the outer surface, thus causing decrease in hydrogen permeability over the time-on-stream (TOS) of 15 h.

The hydrogen removal via Pd-based membrane reactors did show positive effects on DNMC reaction, represented by the enhancement in methane conversion and C_{2+} yield. However, hydrogen removal can only enhance short-term methane conversion and C_{2+} yield. The long-term stability dramatically decreased with the TOS due to carbon deposition onto both catalyst and membrane materials. The lack of coke-resistant catalyst is a barrier for further advancement of Pd-based membrane reactors for DNMC process. Further improvement of hydrogen removal from DNMC could be realized by increasing the reaction temperature (for example, > 973 K), but both membrane and catalyst materials lack stability under very high temperature conditions.

1.4.3 DNMC in MIEC ceramic membrane reactors

In parallel with the attempts to utilize Pd-based membrane reactors for DNMC, dense MIEC ceramic membrane reactors (listed in **Table 1.2**) were developed for *in-situ* hydrogen removal to enhance methane conversion. The concept of using MIEC membranes for DNMC was first reported by Hamakawa et al.[29] In this study, Ag was used as catalyst and thus the methane conversion was very low (< 1%). It should be mentioned that metal catalyst, especially in porous bulk phase, often favours coke

formation in DNMC. Later on, Iglesia's group carried out detailed studies (both simulation[30] and experimental[30, 31]) on DNMC over Mo/ZSM5 catalyst in the MIEC membrane reactor. The simulation results showed that the maximum C_2-C_{10} yields of 14% for the catalytic CH_4 pyrolysis at 1038 K[30] could be reached. By continuously removing H_2 from the membrane reactor system, the maximum product yields can be increased to 88%. Product yields are limited by thermodynamics, kinetic inhibition by H_2, and carbon deposition on the surface of the catalyst. However, the results of experimental studies were not favorable due to the insufficient H_2 flux of membrane reactors and accelerated catalyst deactivation under H_2 removal conditions[30, 31]. For example, in their first experimental attempt, the H_2 transport membrane made of dense $SrZr_{0.95}Y_{0.05}O_3$ disk (16 mm dimeter x 1 mm thickness) was used to remove hydrogen. However, no observable effects on the CH_4 conversion was obtained, which was attributed to the insufficient H_2 flux[30]. This is because disk-shaped membranes have low surface-to-volume ratio, and therefore do not have appreciable effective surface area.

Table 1.2. Overview of the catalyst and dense ceramic membrane-based H_2-permeable membrane reactor types used for DNMC reactions in literature.

Membrane type	Catalyst and reaction condition	Membrane geometry/dimension	Performance	Year/Reference
$SrCe_{0.95}Yb_{0.05}O_{3-\delta}$	Temperature: 1173 K Pressure: ~ 101 kPa Catalyst: Ag	Disk (12 mm diameter x 1 mm thickness)	CH_4 conv.: < 1% Selectivity: observed C_2 product, no analysis for other products. H_2 removal: N/A	1994 [[29]]
$SrZr_{0.95}Y_{0.05}O_3$	Temperature: 950 K Pressure: ~ 101 kPa Catalyst: 4 wt% Mo/ZSM5	Disk (16 mm diameter x 1 mm thickness)	CH_4 conv.: 10-12% Selectivity: > 90% C_{2+} H_2 removal: < 5%	1998 [[30]]

$SrCe_{0.95}Yb_{0.05}O_{3\delta}$	Temperature: 950-1000 K Pressure: ~ 101 kPa Catalyst: 4 wt% Mo/ZSM5 Co-feed: CO_2	Disk (2 μm thickness on 1 mm thickness porous substrate, unknown diameter)	CH_4 conv.: < 13.3% Selectivity: ~73% C_2-C_{10} and 6% C_{12+} H_2 removal: 7-16%	2002 [[31]]
$SrCe_{0.95}Yb_{0.05}O_{3-\delta}$	Temperature: 1023-1273 K Pressure: ~ 101 kPa Catalyst: No catalyst	Hollow fiber (1.45 mm outer diameter x 0.65 mm inner diameter x 260 mm length)	CH_4 conv.: ~6 % Yield: ~13.4 % C_2 H_2 removal: N/A	2006 [[36]]
$BaZr_{0.7}Ce_{0.2}Y_{0.1}O_{3-\delta}$ (external circuit needed)	Temperature: 983 K Pressure: ~ 101 kPa Catalyst: 6 wt% Mo/MCM22	Tubular (10 mm outer diameter x 7 mm inner diameter x 250-300 mm length x 0.025-0.030 mm electrolyte thickness)	CH_4 conv.: < 12% Selectivity: > 80% aromatics H_2 removal: varies depending on applied current density	2016 [[35]]
$La_{5.5}W_{0.6}Mo_{0.4}O_{11.25-\delta}$	Temperature: 973 K Pressure: ~ 101 kPa Catalyst: 6 wt % Mo/ZSM5	Hollow fiber U-shape (~0.2 mm thickness)	CH_4 conv.: ~10% Selectivity: 30-40% aromatics, 60-70% coke H_2 removal: 40-60%	2016 [[37]]

In addition, according to the Wagner equation, the thickness of the membrane significantly affects the H_2 permeation flux. Inspired by this fundamental analysis, Liu et al.[31] fabricated a much thinner $SrZr_{0.95}Y_{0.05}O_3$ membrane (~2 μm in thickness) supported on a 1 mm thick porous support. The results showed that higher H_2 removal efficiencies were achieved at 993 K (16%) compared to 950 K (< 7%), which resulted in a slight increase in CH_4 conversion. Higher rate of H_2 removal also led to a higher catalyst deactivation rate. Addition of small amount of CO_2 slowed down the deactivation rate, and prolonged the lifetime of the catalyst. Still, the advancement of MIEC membrane reactors for DNMC is constrained primarily by low hydrogen flux, which is due to insufficient membrane design and fabrication as well as coking on catalyst during reaction.

In recent years, Xue et al.[37] has demonstrated an enhancement in CH_4 conversion and product yield for the DNMC reaction in the MIEC membrane reactors by employment of a new reactor geometry, i.e., hollow fiber membrane. The membrane reactor comprised of 6wt% Mo/HZSM5 catalyst and $La_{5.5}W_{0.6}Mo_{0.4}O_{11.25-\delta}$ (LWM0.4) membrane, in which the membrane was designed into "U" shape to enable the highest surface-to-volume ratio compared to disk or tubular configurations. The group has demonstrated the performance of the DNMC reaction in the fixed-bed reactor (without H_2 removal) and the membrane reactor (with H_2 removal). First, the CH_4 conversion for the membrane reactor is higher than that of the fixed-bed reactor. In addition, the CH_4 conversion of the membrane reactor is slightly higher than the thermodynamic value of 12% at 973 K. The yield of aromatics (~47%) in the membrane reactor is also higher than that in the fixed-bed reactor. However, as the TOS increased, the differences between membrane and fixed-bed reactors become smaller due to accelerated catalyst deactivation under H_2 removal conditions.

1.5 Thesis overview

Chapter 1 represents the motivation and rationale behind our research to develop the DNMC catalyst and H_2-permeable membrane reactor system to enhance the performance of the DNMC reaction. Chapter 1 also includes a comprehensive review of the existing DMNC catalysts and H_2-permeable membranes. Chapter 2 details the fabrication of the $SrCe_{0.7}Zr_{0.2}Eu_{0.1}O_{3-\delta}$ tubular membrane reactor and the synthesis of the Fe/SiO_2 catalyst. Chapter 3 studies the performance of the Fe/SiO_2 catalyst coupled with the $SrCe_{0.7}Zr_{0.2}Eu_{0.1}O_{3-\delta}$ tubular membrane reactor in order to circumvent to thermodynamic limitations of the DMMC reaction. The effects of

temperature, space velocities of the DMNC reaction, sweep gases (He, H_2), and sweep gas flow rates are analysed. Chapter 4 demonstrates the effects of using CO_2 as sweep gas for the dual utilization of greenhouse gases (CH_4, CO_2) to produce C_{2+} hydrocarbons (feed side) and syngas (sweep side) in the Fe/SiO_2 catalyst and $SrCe_{0.7}Zr_{0.2}Eu_{0.1}O_{3-\delta}$ H_2-permeable membrane reactor system. Chapter 5 demonstrates the autothermal operation of the Fe/SiO_2 catalyst and $SrCe_{0.7}Zr_{0.2}Eu_{0.1}O_{3-\delta}$ H_2-permeable membrane reactor system. This is achieved by using the O_2 sweep gas to combust the permeated H_2 in order to utilize the heat released for the combustion to provide heat for the endothermic DMNC reaction. Chapter 6 demonstrates the enhancement of the production of liquid hydrocarbons (aromatics) for the DNMC reaction via a dual DNMC reactor/H_2-membrane separator. Lastly, chapter 7 highlights some concluding remarks and potential future works for the project.

Chapter 2: Fabrication of the $SrCe_{0.7}Zr_{0.2}Eu_{0.1}O_{3-\delta}$ Hydrogen Permeable Tubular Membrane Reactor and synthesis of the Fe/SiO_2 catalyst

2.1 Introduction

In this research, we propose a tubular membrane reactor system that is comprised of a H_2 permeable $SrCe_{0.7}Zr_{0.2}Eu_{0.1}O_{3-\delta}$ membrane and the Fe/SiO_2 catalyst to improving methane conversion while maintaining catalyst durability and selectivity to C_2 and aromatic products under H_2 removal condition. The $SrCe_{0.7}Zr_{0.2}Eu_{0.1}O_{3-\delta}$ membrane was designed with thickness around ~25 μm and was supported on a porous $SrCe_{0.8}Zr_{0.2}O_{3-\delta}$ tube. The hydrogen permeable tubular membrane reactors have been studied for various applications such as hydrogen separation, water-gas-shift reaction, and CO_2 reforming reaction in our previous work.[94-97] The tubular reactor design increases the H_2 permeable surface area and avoids need for sealing of membrane in the heating zone, and thus reaches stable and higher H_2 permeation from the reactor compared to the disk-shaped membrane design in most previous studies. The Fe/SiO_2 catalyst has lattice-confined single iron sites embedded in the silica matrix, which has been demonstrated with superior methane conversion, selectivity to hydrocarbons and durability by Bao and co-authors.[55] Details of the synthesis method of the Fe/SiO_2, and the fabrication of the H_2-permeable $SrCe_{0.7}Zr_{0.2}Eu_{0.1}O_{3-\delta}$ membrane reactor are detailed below

2.2 Materials Synthesis

2.2.1 Synthesis of $SrCe_{0.8}Zr_{0.2}O_{3-\delta}$ and $SrCe_{0.7}Zr_{0.2}Eu_{0.1}O_{3-\delta}$ powder. The H_2 permeable membrane reactor consists of the $SrCe_{0.8}Zr_{0.2}O_3$ porous tubular support and

the thin and dense $SrCe_{0.7}Zr_{0.2}Eu_{0.1}O_{3-\delta}$ membrane coated on the porous support. The $SrCe_{0.8}Zr_{0.2}O_3$ porous tubular support was made of $SrCe_{0.8}Zr_{0.2}O_3$ powder. $SrCe_{0.8}Zr_{0.2}O_3$ powder was prepared by the conventional solid-state synthesis method using $SrCO_3$ (Aldrich, ≥99.9%), CeO_2 (Alfa Aesar, 99.9%) and ZrO_2 (Inframat, 99.9%) as starting materials. In a typical synthesis, stoichiometric amounts of $SrCO_3$, CeO_2, and ZrO_2 were mixed by a ball milling process. Sufficient amount of ethanol (Pharmco-AAPER, 200 proof) and milling media (yttria-stabilized zirconia) were also added to help create homogeneity in the milling process. The resultant slurry was ball milled for 24 hours, followed by drying, grinding into fine powder, and then calcination at 1573K for 10 hours. The as-obtained material was $SrCe_{0.8}Zr_{0.2}O_3$ perovskite ceramic powder.

The $SrCe_{0.7}Zr_{0.2}Eu_{0.1}O_{3-\delta}$ membrane was made of the $SrCe_{0.7}Zr_{0.2}Eu_{0.1}O_{3-\delta}$ powder, which was synthesized via a citrate precipitation method using $Ce(NO_3)_3{\cdot}6H_2O$ (Alfa Aesar, 99.5%), $Sr(NO_3)_2$ (Alfa Aesar, 99%), $ZrO(NO_3)_2{\cdot}H_2O$ (Chemsaver, 99.9%), and $Eu(NO_3)_3{\cdot}6H_2O$ (Alfa Aesar, 99.9%) as starting materials. In order to synthesize $SrCe_{0.7}Zr_{0.2}Eu_{0.1}O_{3-\delta}$, stoichiometric amounts of $Ce(NO_3)_3{\cdot}6H_2O$, $Sr(NO_3)$, $ZrO(NO_3)_2{\cdot}H_2O$, and $Eu(NO_3)_3{\cdot}6H_2O$ were dissolved in de-ionized water (DI-water). Citric acid (Alfa Aesar, 99+%) and ethylene glycol (Alfa Aesar, 99%) were added to the solution. The molar ratio of the total metal nitrates to citric acid and ethylene glycol was 1:2:2. This is used to prevent the formation of secondary phases, and decrease the calcination temperature. The solution was heated to 393 K, and maintained at that temperature in order to evaporate the DI-water under constant stirring. Once all the DI-water was evaporated, a gel was formed. The temperature was then raised to 673 K in order to auto-ignite the combustion of the gel. Once the gel was

combusted, the resultant material was ball milled for 24 hours in ethanol, followed by drying, grinding into fine powder, and then calcination at 1473 K for 10 hours. The as-obtained material was $SrCe_{0.7}Zr_{0.2}Eu_{0.1}O_{3-\delta}$ perovskite ceramic.

2.2.2 Fe/SiO_2 catalyst synthesis. The iron source used for synthesis of Fe/SiO_2 catalyst is fayalite (Fe_2SiO_4), which was prepared via a sol-gel synthesis method reported by DeAngelis et al.[98] The synthesis typically required a 1000 mL three-neck flask and an oil bath which was used to heat the reactants in the flask. The left and right necks of the flask were sealed with rubber septa. The left one was pushed through with a syringe needle to deliver the argon gas to purge the flask before and in the process of the reaction. The right one was used to add solvents and reactant when needed via a syringe equipped with a needle. The center neck of the flask was connected to a condenser that was sealed at the top with a septum. A syringe needle was pushed through the center septum to vent excess argon gas. A re-circulating cooling bath was attached to the condenser to condense the evaporated solvents in the synthesis process. The flask was heated by an oil both to keep the solvent under reflux condition. A magnetic stirring bar (stirred at 500 rpm) was used to mix the solvents and reactants in the synthesis.

In the synthesis of Fe_2SiO_4, firstly, the three-neck flask was purged with a flowing argon gas (100 $mL \cdot min^{-1}$) for 30 min at room temperature. Secondly, 375 mL toluene (ACS Reagent grade, Fischer) and 175 mL methanol (ACS Reagent grade, Fisher) were added into the three-neck flask under magnetic stirring condition. The mixture was continuously purged by the flowing argon for ~30 min. Thirdly, 8.7g of iron(II) chloride ($FeCl_2$, 99.5% metal basis, Alfa Aesar) and 9.3g of sodium ethoxide ($NaOC_2H_5$, 96%, Acros) were added to the liquid mixture in the flask in sequence.

Afterwards, the mixture was heated to a refluxing condition by the oil bath and 7.9g tetraethyl orthosilicate (TEOS, 98% purity, Sigma-Aldrich) was added in the temperature ramp process. The mixture was kept under refluxing condition for ~30 min. Fourthly, 10 mL of 0.2 M NaOH (99%, Sigma-Aldrich) solution was added to the flask via a syringe pump (New Era Pump Systems NE-1000) at the rate of 0.5 $mL \cdot min^{-1}$. Then, the mixture was kept under refluxing condition for 12 hours before it was finally cooled to room temperature for the next step. Argon gas was continuously flowed through the flask throughout the whole synthesis process.

The gel-like mixture in the flask was transferred to a rotary evaporator (Heidolph Laborota 4000) to remove solvents and form a powder-like sample. Afterwards, the powder sample was calcined in a tube furnace (Thermo Scientific Lindberg Blue M) under flowing N_2 gas (100 $mL \cdot min^{-1}$) at 1073 K for 4 h. The temperature ramp rate was 2 $K \cdot min^{-1}$. After calcination, the fayalite sample was washed with hot (~353 K) deionized H_2O to remove NaCl. The sample was then collected by centrifugation. The washing and centrifugation steps were repeated three times. Finally, the fayalite sample was rinsed with methanol and dried with the rotary evaporator.

Fe/SiO_2 catalyst was prepared by fusing the resultant Fe_2SiO_4 sample and quartz particles (SiO_2, BDH) at 1973 K for 6 hours in stagnant air in a high temperature furnace (MTI Corporation KSL1700X). Before the fusing process, the Fe_2SiO_4 and quartz particles were mixed and ball milled for 12 hours. After cooling to room temperature, the Fe/SiO_2 particles were crushed and sieved to 40-80 mesh for catalysis tests.

2.3 Fabrication of the tubular membrane reactor

2.3.1 Tape casting of the $SrCe_{0.8}Zr_{0.2}O_{3-\delta}$ tubular support. Tape casting is one of the most important advances in ceramic processing technology. Tape casting turns ceramic powder into a thin, flat tape, with a large surface area. The tape can be thought of as a two-dimensional configuration, large in the x and y directions, and very small in the z direction. There are 6 main components to the tape casting slurry: (1) Ceramic material; (2) Solvent; (3) Dispersant; (4) Binder; (5) Plasticizer; and (6) Pore formers. Ceramic material is the most important part of the tape casting slurry. It is the only material that remains at the end of the fabrication process. The other materials are used to assist in the fabrication of the ceramic material into the desired shapes and properties. Tape casting is a "fluid" process, and therefore some types of solvent are needed. The main role of solvent is to aid in the mixing process, and distribute all the components homogenously. In this application, ethanol is used as solvent. When particles are in close contact with each other, they tend to form loosely bounded agglomerations through attractive forces such as van de Waals and other inter-particle forces. The role of the dispersant, in this case, fish oil, is to keep the ceramic powder in homogeneous suspension. This is a desirable phenomenon because binder and plasticizer need to coat each ceramic particle individually in order to produce a good tape. Binder is the network that holds the system together. Plasticizer allows motion within the tape, therefore, permits the tape to be bent without cracking. The binder and platicizer used for this application are polyvinyl butyral (PVB) and benzyl butyl phthalate (BBP), respectively. Thermoplastic 5-μm poly methyl methacrylate (PMMA) is used as the

pore former in this recipe. PMMA leaves pores in its place after burn-off during the sintering process in the preparation of the tubular membrane tube.

Below is the flow chart (**Figure 2.1**) illustrating the steps to prepare the tape casting slurry. Since there is no set formulation of materials to use in the slurry preparation, the tape casting formulation is customized and optimized for the particular $SrCe_{0.8}Zr_{0.2}O_3$ perovskite material used for the tubular membrane support.

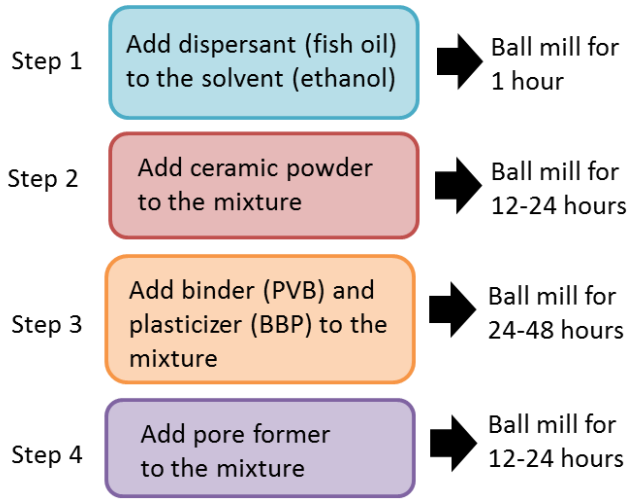

Figure 2.1. Flow chart showing the steps involved in preparation of the tape casting slurry

Once the slurry is ready, it has to be de-aired before the tape casting process. Air can enter into the slurry during the milling and mixing process. If the air bubbles are not removed, they can create defects in the tape, which can leads to fractures and cracks during the sintering process. **Figure 2.2 (A)** below is the apparatus used for the de-airing process. The slurry is put under vacuum and in constant stirring to remove the air bubbles from the slurry. The vacuum is turned on for about 1 min, and is turned

off for 15 min. The cycle is repeated until all the air bubbles are removed, which usually takes about 2 hrs. Once the de-airing process is complete, the slurry is ready to be tape casted.

The thickness of the tape ranges from 0.025 mm to 1.27 mm. The gap between the blade and the carrier dictates the thickness of the tape. During the tape casting process, the carrier is set in motion, and then the slurry is poured into the reservoir. Then the wet tape passes into the drying chamber. In the drying chamber, the solvent is evaporated, and what is left is the dried tape. **Figure 2.2 (B) and (C)** show the apparatuses used for the tape casting and the as-produced $SrCe_{0.8}Zr_{0.2}O_3$ tape in the process.

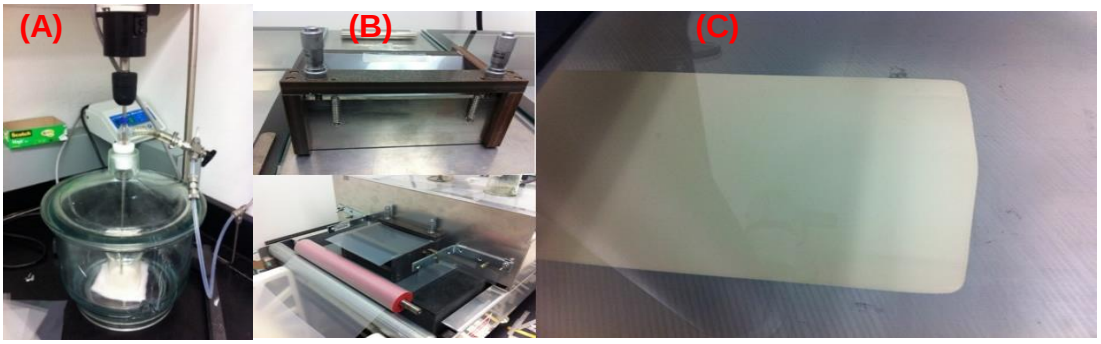

Figure 2.2. (A) The apparatus used for de-air of the tape casting slurry; (B) and (C) show the tape caster and the as-produced $SrCe_{0.8}Zr_{0.2}O_3$ tape in the process.

2.3.2 Fabrication of the green body $SrCe_{0.8}Zr_{0.2}O_{3-\delta}$ tubular support. The dried tape is then rolled with a rolling rod into a tubular membrane support. Once rolled, the rolling rod is removed, and the tubular membrane support is capped. A lamination solution, PVB-ethanol mixture, is acted as glue to bind the layers together. The rolling process for the casted flat tape is shown in **Figure 2.3**. The as-obtained tubular membrane support is ready for the pre-sintering followed by the coating with thin layer

of a hydrogen permeable membrane to produce hydrogen permeable tubular membrane reactor.

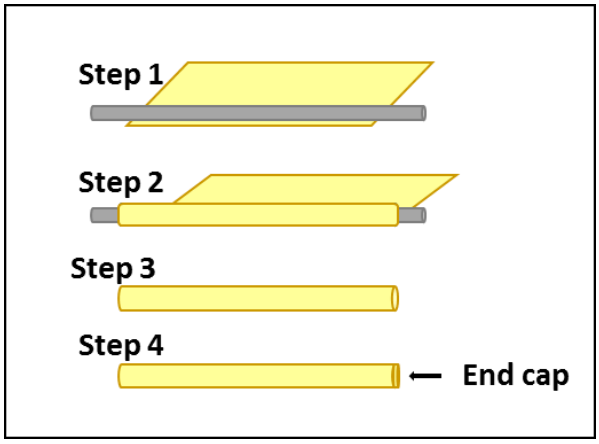

Figure 2.3. Flow chart showing the steps involved in tape rolling process.

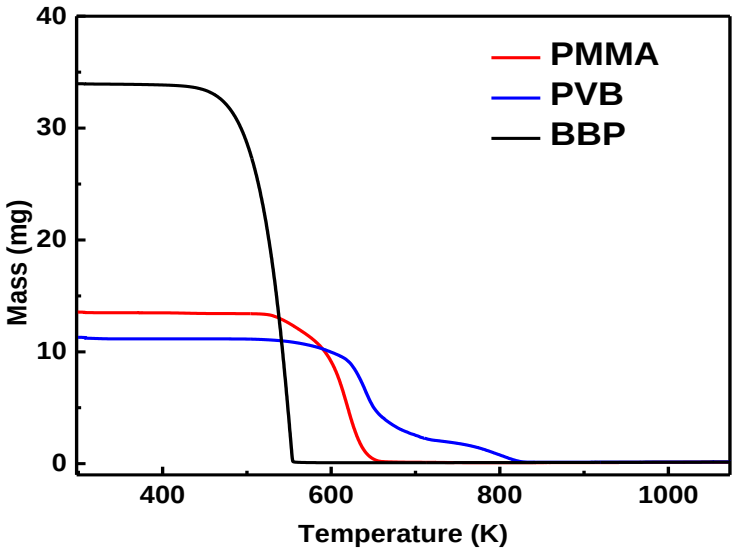

Figure 2.4. TGA data showing the burning off temperatures for the organic components in the tubular membrane support.

Figure 2.4 shows the TGA spectrums of the organic components included in the tape casting slurry, which included PVB, BBP, and PMMA. First, most of the

organic materials are burned off at 673 K, and the rest of the organic (PVB) can be burned off at 873 K. Therefore, the pre-sintering procedure is designed as follow. The first step is to heat the tubular membrane support at a low heating rate of 1.5 K/min to 423 K. This is to remove any leftover organic solvent, and moisture that are adsorbed on the surface of the tubular membrane support. The temperature is hold at 423 K for 2 hours. The second step is to heat the tubular membrane support from 423 K to 673 K at the rate of 1.5 K/min, and hold the temperature at 673 K for 2 hours. This step is to remove the majority of the organic materials, which include the binder, plasticizer, and pore former. The third step is to increase the temperature from 673 K to 873 K at 2 K/min for 30 minutes. This step is to remove the rest of the organic materials. The final step is to escalate the temperature to the final pre-sintering temperature of 1423 K at the rate of 2.5 K/min for 4 hours.

2.3.3 Colloidal coating of $SrCe_{0.7}Zr_{0.2}Eu_{0.1}O_{3-\delta}$ membrane on porous tubular membrane support. In order to prepare the $SrCe_{0.7}Zr_{0.2}Eu_{0.1}O_{3-\delta}$ slurry for colloidal coating, $SrCe_{0.7}Zr_{0.2}Eu_{0.1}O_{3-\delta}$ membrane paste was synthesized. $SrCe_{0.7}Zr_{0.2}Eu_{0.1}O_3$ powder was ball milled with ethanol for 24 hours. Then a commercial system, ESL441 (ESL ElectroScience), was added to the mixture. ESL441 is an ester alcohol-based system with binder and plasticizer. The planetary centrifugal mixer was used to mix and evaporate all the ethanol until the final system left was just a homogeneous paste consisted of the ceramic powder and ESL441 system. The paste was diluted with ethanol prior to the colloidal coating process. After the colloidal coating process, the paste can be recovered by re-evaporating the ethanol via the planetary centrifugal

mixer. Once coated, the tubular membrane reactor was sintered at 1793 K for 6 hours. The surface of the membrane reactor was characterized by scanning electron microscopy (SEM) (Hitachi S-3400 Variable Pressure SEM) to ensure that the membrane was dense without pinholes and cracks.

2.4 Membrane and catalyst characterization.

Scanning electron microscopy (SEM) images were taken on a Hitachi S-3400 Variable Pressure SEM microscope to visualize the surfaces and the cross-sections of the $SrCe_{0.7}Zr_{0.2}Eu_{0.1}O_{3-\delta}$ membrane reactor. N_2 adsorption-desorption isotherms of the samples were measured using an Autosorb-iQ analyzer (Quantachrome Instruments) at 77 K. The samples were outgassed at 523 K for 8 hours and 1 mm Hg prior to measurements. (Brunauer, Emmett and Teller) (BET) method were used to determine the specific surface areas of the samples. X-Ray diffraction (XRD) patterns of the catalyst samples were obtained on Bruker D8 Advance Lynx Powder Diffractometer (LynxEye PSD detector, sealed tube, *Cu Kα* radiation with *Ni β*-filter).

2.4.1 Characterization of the $SrCe_{0.7}Zr_{0.2}Eu_{0.1}O_{3-\delta}$ tubular membrane reactor. The X-Ray diffraction (XRD) patterns (**Figure 2.5**) show the correct perovskite phase, which confirmed the successful synthesis of $SrCe_{0.8}Zr_{0.2}O_3$ and $SrCe_{0.7}Zr_{0.2}Eu_{0.1}O_{3-\delta}$ membrane materials.

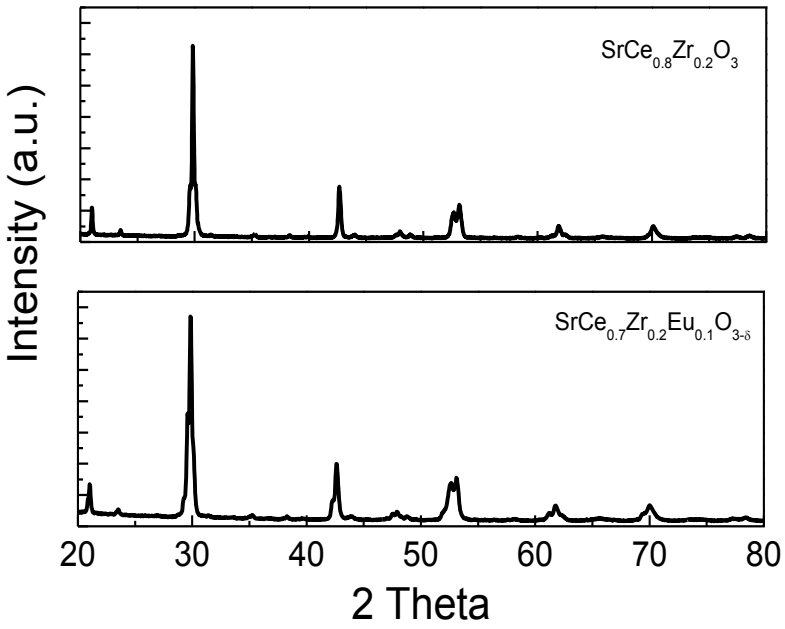

Figure 2.5. XRD patterns of $SrCe_{0.8}Zr_{0.2}O_3$ and $SrCe_{0.7}Zr_{0.2}Eu_{0.1}O_{3-\delta}$ materials.

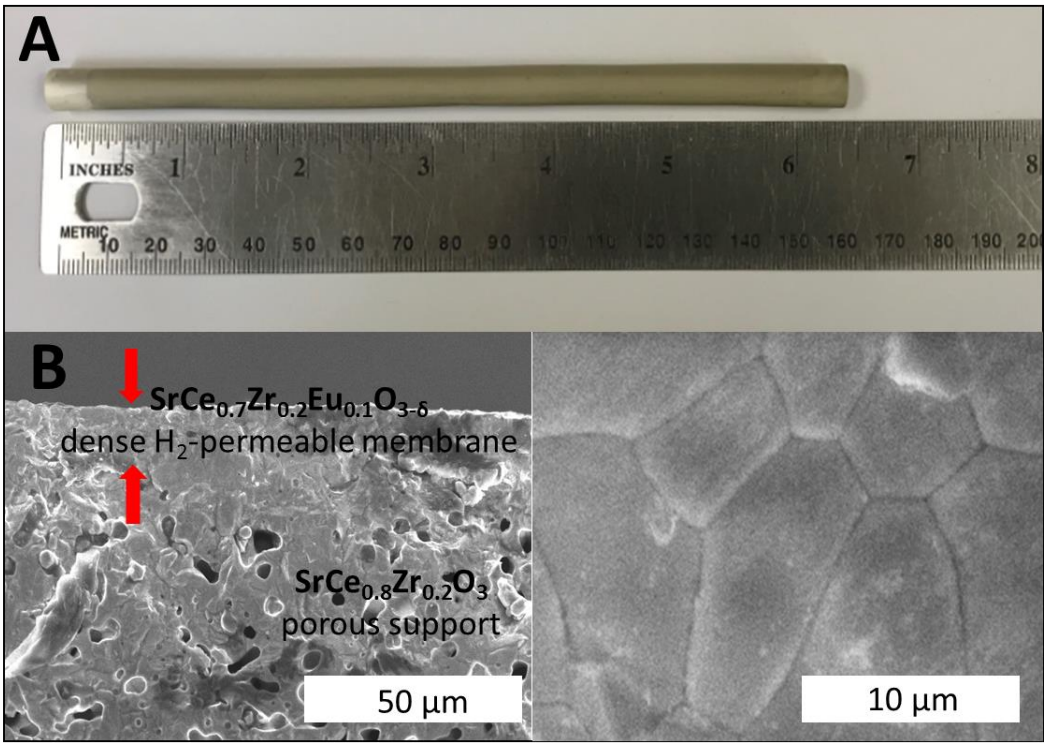

Figure 2.6. (A) As-prepared $SrCe_{0.7}Zr_{0.2}Eu_{0.1}O_{3-\delta}$ tubular membrane reactor, (B) SEM image showing the cross-sectional image of membrane tube reactor comprised of $SrCe_{0.7}Zr_{0.2}Eu_{0.1}O_{3-\delta}$ thin film on the porous $SrCe_{0.8}Zr_{0.2}O_{3-\delta}$ tubular support

The surface of the membrane reactor was characterized by scanning electron microscopy (SEM) to ensure that the membrane was dense without pinholes and cracks. (**Figure 2.6 (B)**)

2.4.2 Characterization of the Fe/SiO_2 catalyst. XRD data in **Figure 2.7(A)** shows that crystalline phase of SiO_2 in the Fe/SiO_2 sample. Neither Fe nor FeO_x diffraction peaks were observed in the XRD pattern. **Figure 2.7(B)** shows the N_2 adsorption/desorption isotherm of the Fe/SiO_2 sample. The surface area of the catalyst was found to be <1 $m^2 \cdot g^{-1}$.

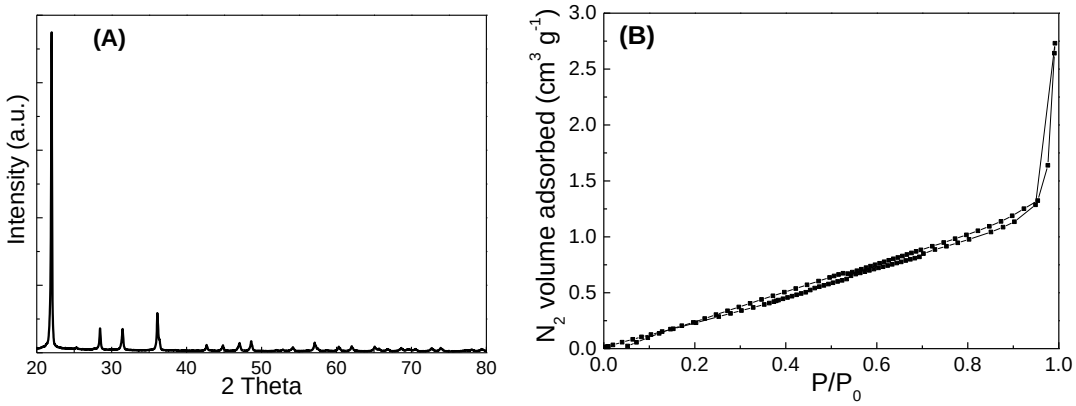

Figure 2.7. (A) XRD pattern and (B) N_2 adsorption/desorption isotherm of Fe/SiO_2 catalyst used for the DNMC reaction.

Chapter 3: Hydrogen Permeable Tubular Membrane Reactor: Promoting Conversion and Product Selectivity for Non-oxidative Activation of Methane over Fe/SiO_2 Catalyst

3.1 Introduction

As mentioned in Chapter 1, methane (CH_4), an abundant natural resource, is the main constituent of natural gas and oil-associated gases. Studies on CH_4 conversion have explored indirect conversion of CH_4 to synthesis gas ($CO + H_2$) followed by Fischer-Tropsch synthesis of higher hydrocarbons[12, 99-102], oxidative coupling of CH_4 to C_{2+} hydrocarbons[103-105], and direct non-oxidative CH_4 conversion (DNMC) to H_2, light hydrocarbons and aromatics[11, 14, 106, 107]. In comparison with the first two approaches, DNMC is more simple and selective given its unique capability in forming C_{2+} hydrocarbons and H_2 while circumventing the intermediate energy intensive steps[11, 12, 108]. However, kinetic and thermodynamic constraints in DNMC lead to low CH_4 conversion at practical reaction conditions[13, 109].

Considerable efforts have been placed on the development of membrane reactors comprised of active catalysts and H_2 permeable membranes for DNMC reactions[37, 110-116]. The molybdenum/zeolite (Mo/ZSM-5) has been the most extensively studied catalyst[27, 52, 117, 118]. H_2 or O_2 permeable membranes, such as metal alloys[89, 92] and ionic/electronic conducting ceramics[113-115, 119-121], capable of H_2 withdrawal from or O_2 addition into the reactor were exploited to alleviate the barriers for equilibrium conversion. Although a substantial enhancement of the CH_4 conversion has been predicted when a H_2 permeable membrane was used in conjunction with a DNMC catalyst, the parallel experimental studies on NMC process in membrane

reactors were not favorable due to the lack of membranes with sufficient H_2 permeation flux and the accelerated catalyst deactivation under H_2 removal conditions[111, 113, 122-124].

In this chapter, we report a tubular membrane reactor that is comprised of a mixed ionic-electronic conducting $SrCe_{0.7}Zr_{0.2}Eu_{0.1}O_{3-\delta}$ membrane and the iron/silica (Fe/SiO_2) catalyst to improving CH_4 conversion while maintaining catalyst durability and selectivity to C_2 and aromatic products under H_2 removal conditions. The $SrCe_{0.7}Zr_{0.2}Eu_{0.1}O_{3-\delta}$ membrane was designed with thickness around ~20 μm with an active surface area of ~12 cm^2 supported on ~1 mm thick $SrCe_{0.8}Zr_{0.2}O_{3-\delta}$ tube with a diameter of ~6 mm. This type of tubular membrane reactors have been studied for H_2 production from water-gas-shift and CO_2 reforming of CH_4 reactions in previous reports.[94, 96, 98, 125] Fe/SiO_2 catalyst has lattice-confined single iron sites embedded in the silica matrix, which has been demonstrated to have superior DNMC performance by Bao and co-authors[55]. The integration of the Fe/SiO_2 (containing 0.5 wt% Fe) catalyst in the $SrCe_{0.7}Zr_{0.2}Eu_{0.1}O_{3-\delta}$ membrane reactor for DNMC showed an enhancement in CH_4 conversion compared to that in a fixed-bed reactor. The DNMC reaction showed up to ~30% CH_4 conversion, 99% selectivity to C_2 and aromatics, and a long catalyst lifetime at the tested conditions. The product selectivity towards light hydrocarbon (acetylene and ethylene) or heavy aromatics (benzene and naphthalene) was manipulated by adding H_2 into or removing H_2 from the $SrCe_{0.7}Zr_{0.2}Eu_{0.1}O_{3-\delta}$ membrane reactor. The tubular membrane reactor design increases the H_2 permeable surface area and avoids need for sealing of membrane in the high temperature heating

zone, leading to more stable and higher H_2 permeation compared to the disk-shaped membrane design in most previous studies[37, 110-116].

3.2 Experiments

3.2.1. H_2 permeation and Leakage tests for H_2 permeable tubular membrane reactor. Prior to the usage of the H_2 permeable membrane reactor for DNMC over Fe/SiO_2 catalyst, the membrane reactor underwent leakage and H_2 permeation tests. The tubular membrane reactor was used for these experiments. The feed side (inside of the membrane) was exposed to H_2 diluted to the tested concentration using Ar tracer. The total flow rate of the feed gas (mixture of H_2 and Ar) was set at 20 $mL \cdot min^{-1}$. The sweep side (outside of the membrane) was exposed to He at 20 $mL \cdot min^{-1}$, and connected to a mass spectrometer (Dycor QuadLink IPS Quadruple Gas Analyzer) for quantifying the permeated H_2. **Figure 3.1(A)** shows the assembly of H_2-permeable membrane reactor for the permeation tests. In addition to being a diluent, the Ar in the feed gas was used as a tracer. A leak will be indicated by an increase in Ar signal in the mass spectrometer. The H_2 permeable membrane tubular reactor without any leakage was indicted by the measured gas profiles shown in **Figure 3.1(B).**

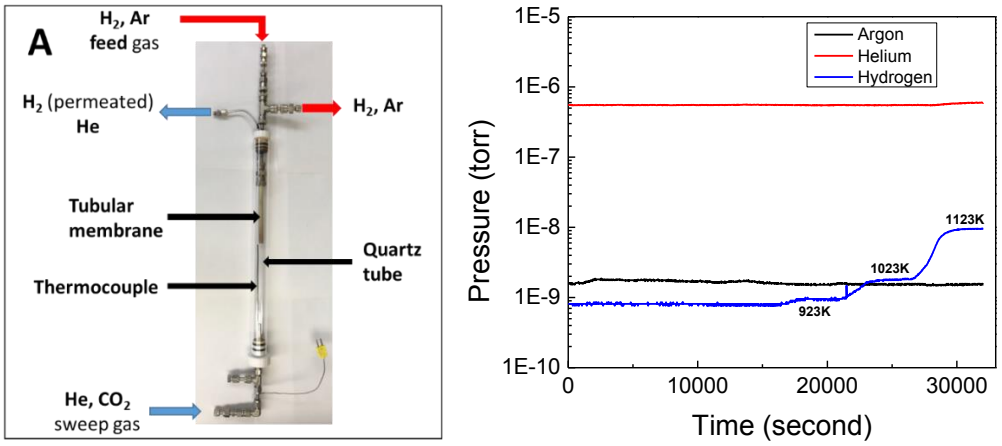

Figure 3.1. (A) the assembly of H_2-permeable membrane reactor for the permeation tests. (B) Typical profile of the permeation test for the H_2 permeable tubular membrane reactor without leakage (feed and sweep gas flow rates = 20 mL·min^{-1}).

3.2.2. DNMC reaction in fixed-bed and H_2 permeable $SrCe_{0.7}Zr_{0.2}Eu_{0.1}O_{3-\delta}$ membrane reactors. The DNMC reaction was run at atmospheric pressure in either a fixed-bed (without H_2 permeation, **Figure 3.2(B)** or tubular membrane reactor (with H_2 permeation, **Figure 3.2(A)**). In a typical experiment, 0.375 g of catalyst was loaded at the center of the reactor and then heated to the desired temperature in pure Ar at the rate of 20 mL·min^{-1}. After the reaction gas mixture (90%CH_4-10%Ar) was introduced, the reaction was run at the temperature range of 1223-1323 K and at a feed gas space velocity of 3200 mL·g^{-1}·h^{-1}. During the reaction in the tubular membrane reactor, the sweep gas, either He or H_2, was introduced. The reactant (CH_4 mixed with a 10 mol% Ar tracer) was introduced through the inner tube in the top center section of the reactor and the products exited through the top left side of the reactor. The outer annular region of the membrane reactor was exposed to He or H_2 sweep gas to carry the permeated H_2 away from the reactor system or to feed H_2 into the reactor system. The product effluents were analyzed on-line by Agilent 6890 Gas Chromatograph, and the

permeated gas by mass spectrometer (Dycor QuadLink IPS Quadruple Gas Analyzer) to determine the CH_4 conversion and product selectivity.

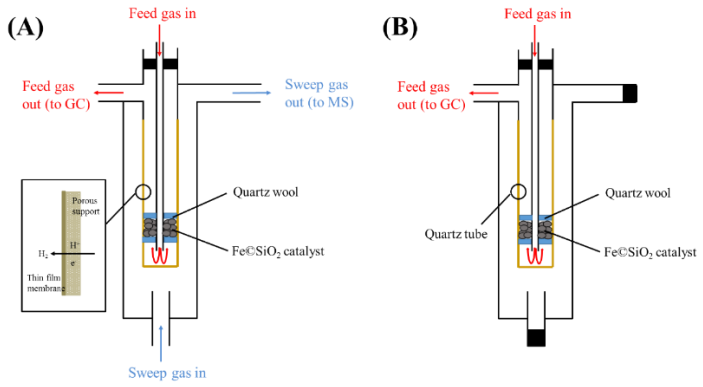

Figure 3.2. Detailed reactor set-up for (A) H_2 permeable $SrCe_{0.7}Zr_{0.2}Eu_{0.1}O_{3-\delta}$ membrane reactor and (B) fixed-bed reactor.

3.3 Results and Discussions

3.3.1 H_2 permeation through the $SrCe_{0.7}Zr_{0.2}Eu_{0.1}O_{3-\delta}$ tubular membrane reactor.

The H_2 permeation through the $SrCe_{0.7}Zr_{0.2}Eu_{0.1}O_{3-\delta}$ membrane in the membrane reactor was measured prior to the catalysis tests. **Figure 3.3(A)** shows that the permeated H_2 flux was increased with the H_2 concentration on the feed side. In addition, the H_2 permeation flux increased as the temperature increased due to the increase in ambipolar ionic/electronic conductivity of the $SrCe_{0.7}Zr_{0.2}Eu_{0.1}O_{3-\delta}$ membrane. A further analysis shows that the H_2 permeation flux was proportional to the transmembrane H_2 partial pressure gradient with a 1/4 dependence (**Figure 3.3(B)**). At ~20 μm membrane thickness, H_2 permeation rates are controlled by bulk diffusion through the dense $SrCe_{0.7}Zr_{0.2}Eu_{0.1}O_{3-\delta}$ membrane[126]. According to the Wagner

equation[127], H_2 permeation flux ($J_{OH_O^{\cdot}}$) through a proton conducting membrane can be expressed:

$$J_{OH_O^{\cdot}} = -\frac{1}{L}\left[\frac{RT}{4F^2}\int_{P'_{O2}}^{P''_{O2}} \sigma_t t_{OH_O^{\cdot}} t_{V_O^{\cdot\cdot}} dlnP_{O_2} + \frac{RT}{2F^2}\int_{P'_{H2}}^{P''_{H2}} \sigma_t t_{OH_O^{\cdot}} (t_{V_O^{\cdot\cdot}} + t_{e'}) dlnP_{H_2}\right] \quad (3.1)$$

where L is the membrane thickness in meter; R is gas constant in J mol^{-1} K^{-1}; T is temperature in K; t_i (i=e´, $OH^{\bullet}_O$, $V^{\bullet\bullet}_O$) is the transference number of *i*; σ_t is total conductivity in S m^{-1}; P'_{O2}, P''_{O2}; P'_{H2}, and P''_{H2} are the O_2 and H_2 partial pressure in atm at both sides of the membrane, respectively. When the membrane is exposed to H_2 atmosphere, protons and electrons are the dominating defects and Eq. (2) is obtained after integrating the Wagner equation.

$$J_{OH_O^{\cdot}} \propto -\frac{1}{L}((P_{H_2}^{f})^{\frac{1}{4}} - (P_{H_2}^{p})^{\frac{1}{4}}) \quad (3.2)$$

which results in a $P_{H2}^{\,1/4}$ dependence consistent with the results in **Figure 3.3(B)**.

The Wagner equation[127] explains the H_2 permeation behaviors through the $SrCe_{0.7}Zr_{0.2}Eu_{0.1}O_{3-\delta}$ membrane in the tubular reactor

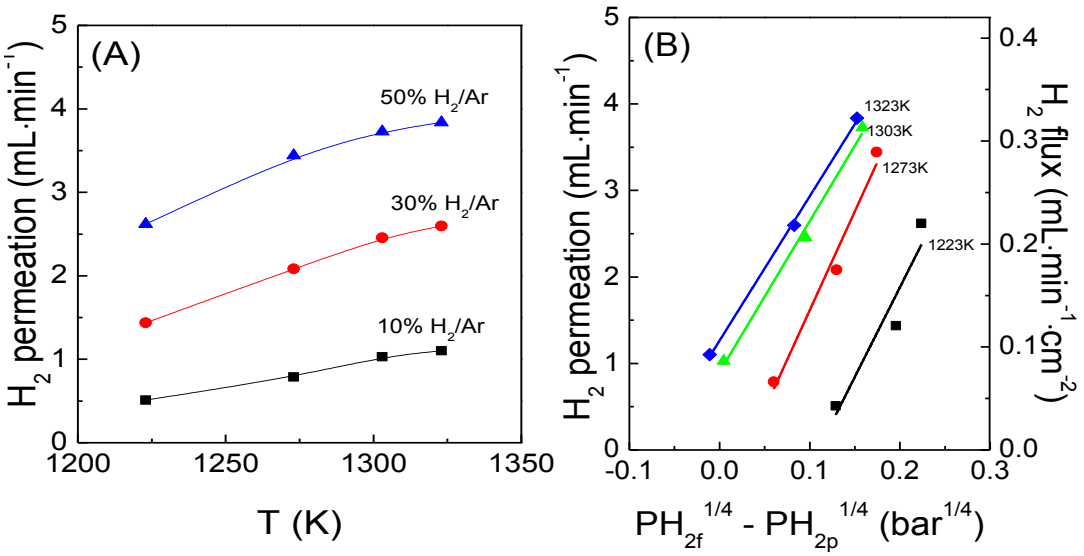

Figure 3.3. H_2 permeation flux through $SrCe_{0.8}Zr_{0.2}O_{3-\delta}$ membrane in the packed-bed membrane reactor as a function of temperature (A) and H_2 partial pressure (B), respectively.

3.3.2 Performance of the $SrCe_{0.7}Zr_{0.2}Eu_{0.1}O_{3-\delta}$ tubular membrane reactor coupled with Fe/SiO_2 catalyst. The CH_4 conversion and product selectivity as a function of reaction temperature in both fixed-bed and H_2 permeable membrane reactors are shown in **Figure 3.4.** An increase in CH_4 conversion with increasing temperature was observed in both types of reactors due to the endothermic nature of the NMC reaction. The simultaneous removal of H_2 from the membrane reactor shifted the reaction to the product side, and thus increased the CH_4 conversion. Higher H_2 permeation flux athigher temperature and higher H_2 partial pressure differences are expected, according to Wagner equation[127] and **Figure 3.4**, to lead to an increase in CH_4 conversion. The percent increase in CH_4 conversion from fixed-bed to membrane reactors, comparing **Figures 3.4(A) and 3.4(B)**, however, showed a decreasing trend. The discrepancy in CH_4 conversion between this analysis and experimentally measurement might be caused by deposition of carbon species on the membrane surface in the catalyst

activation stage that reduced the H_2 flux or by complex chemistry in membrane reactor which involved multiple types of hydrocarbon species influencing H_2 permeation dynamics. The production and permeation rates of H_2 at each reaction temperature have been quantified (**Appendix A**). The enhancement in CH_4 conversion caused by H_2 removal has been evaluated by considering a right-hand side shift of the reaction equation (CH_4 = 3/52 C_6H_6 + 5/104 $C_{10}H_8$ +7/104 C_2H_4 +2/104 C_2H_2 + 19/13 H_2) according to the Le Châtelier's principle. The calculated CH_4 conversion is nearly the same as those measured (**Appendix A**), which indicated the effectiveness of the H_2 permeable membrane reactor in shifting the CH_4 conversion in the NMC chemistry.

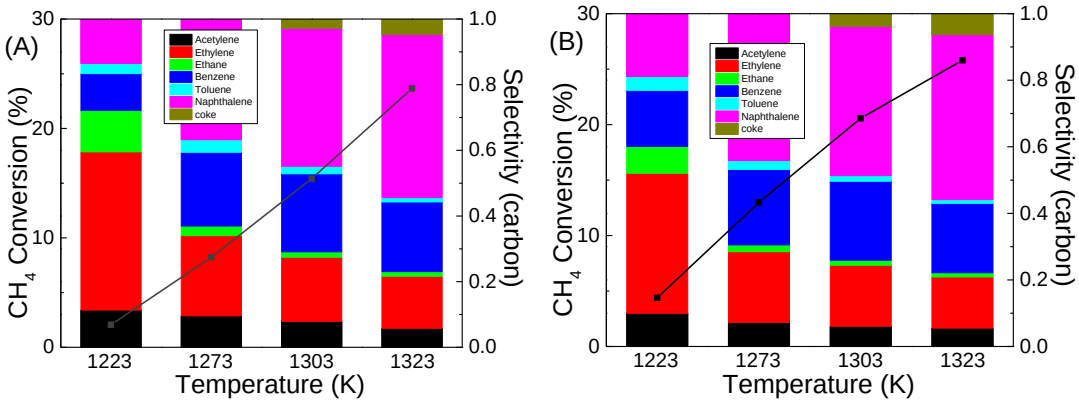

Figure 3.4. CH_4 conversion and product selectivity over Fe/SiO_2 catalyst in a fixed-bed (A) and packed-bed membrane reactor (B) at different temperatures (space velocity = 3200 $mL \cdot g^{-1} \cdot h^{-1}$)

Figure 3.4 also shows the effects of H_2 removal on the product selectivity of the DNMC reaction. In the fixed-bed reactor, the reaction was very selective toward C_2 (ethylene, acetylene and ethane, ~ 70%), and only small amount of aromatics (< ~30%) were formed at 1223 K. As the temperature increased, the selectivity shifted from smaller C_2 products to aromatics (benzene, toluene and naphthalene). Comparing the

product selectivities between the fixed-bed and the H_2 permeable membrane reactors, the membrane reactor was slightly less selective for C_2 and more selective for aromatic products. The yields for both C_2 and aromatics of the membrane reactor are higher at all temperatures tested compared to the fixed-bed reactor.

The manipulation of the sweep side environment which is expected to influence the catalysis chemistry inside the membrane reactor was carried out by flowing sweep He gas at different flow rates (20, 50 and 100 $mL \cdot min^{-1}$) and switching He to H_2 sweep gas, respectively. **Figure 3.5(A)** shows that CH_4 conversion increased with an increase of He flow to 50 $mL \cdot min^{-1}$ and doubled at 100 $mL \cdot min^{-1}$ He flow compared to that in fix-bed reactor. The high sweep He flow carried away more H_2 through the membrane reactor. The CH_4 conversion was calculated based on the permeated H_2, and matched well with the measured conversion in the membrane reactor. For comparison, H_2 was purposely added back to the membrane reactor by flowing H_2 as sweep gas. The CH_4 conversion was slightly reduced (**Figures 3.5(A) and 3.5(B)**) because the reaction was shifted to the reactant side according to Le Châtelier's principle.

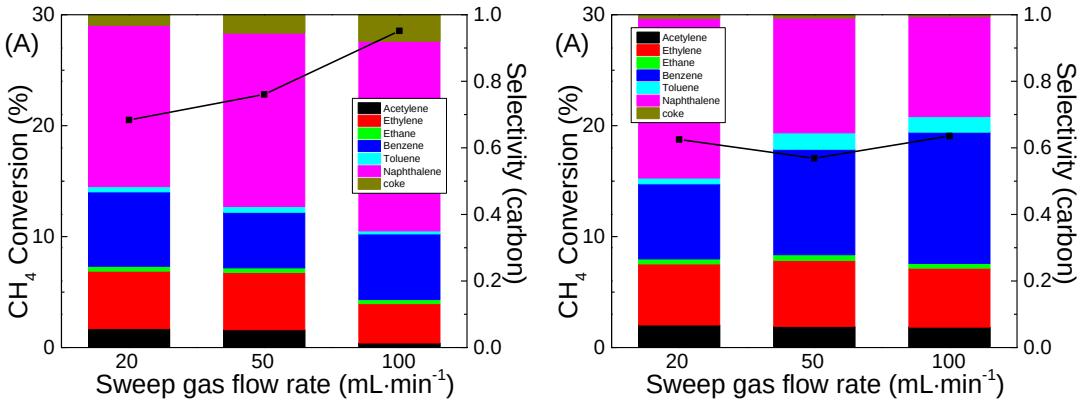

Figure 3.5. CH_4 conversion and product selectivity over Fe/SiO_2 catalyst in a packed-bed membrane reactor at different He (A) or H_2 (B) sweep gas flow rates (temperature = 1303K, space velocity = 3200 $mL \cdot g^{-1} \cdot h^{-1}$).

The product selectivity towards C_2 or aromatics was tuned by varying the type of sweep gases and their flow rates. The selectivity to naphthalene increased with increasing He flow rate (**Figure 3.5(A)**) while the C_2 and benzene products increased with increasing H_2 flow rates (**Figure 3.5(B)**). Bao and co-authors[55] hypothesized that the lattice confined single Fe site initiates CH_4 dehydrogenation to generate methyl ($\cdot CH_3$) and hydrogen ($\cdot H$) radicals, which subsequently release from the surface and undergo a series of gas-phase reactions to form dehydrogenated and cyclized products. The manipulation of sweep gas type influences the concentrations and types of hydrogen species in the reactor which impacts the product selectivity.

Table 3.1 and **Table 3.2** show the theoretical analysis for the increase in CH_4 conversion due to the removal of H_2 at different temperatues and flow rates of He sweep gas. By comparing the CH_4 conversions in membrane reactors upon H_2 removal between predictions from theoretical analysis and experimental measurements, it was found that the values generally matched with each other, which proved the validity of the enhancement of CH_4 conversion from H_2 removal via the membrane reactor.

Table 3.1. Theoretical analysis for CH_4 conversion increase due to H_2 removal from the membrane reactor at different reaction temperatures.

Reaction temperature (K)	H_2 production in fixed-bed reactor [a] ($mL \cdot min^{-1}$)	H_2 permeation in membrane reactor [b] ($mL \cdot min^{-1}$)	Fraction of H_2 removal [c] (%)	CH_4 conversion (%)		
				fixed-bed reactor [d] (measured)	membrane reactor [e] (calculated)	membrane reactor [f] (measured)
1223	0.54	0.25	47	2.1	3.9	4.4
1273	2.17	0.51	23	8.2	10.6	12.9
1303	4.06	0.77	19	15.4	19.4	20.6
1323	6.22	0.83	13	23.7	28.8	25.8

[a] Quantified by TCD detector in GC instrument; [b] Determined by mass spectrometer instrument; [c] Divided [a] by [b]; [d] Quantified by TCD detector in GC instrument (calculated based on method in

Appendix A); [e] Theoretical calculation based on a and c; [f] Quantified by TCD detector in GC instrument (calculated based on method in Appendix A)

Table 3.2. Theoretical analysis for CH_4 conversion increase due to H_2 removal from the membrane reactor at different He sweep gas flow rate (T = 1303 K).

He flow rate ($mL \cdot min^{-1}$)	H_2 production in fixed-bed reactor [a] ($mL \cdot min^{-1}$)	H_2 permeation in membrane reactor [b] ($mL \cdot min^{-1}$)	Fraction of H_2 removal [c] (%)	CH_4 conversion (%)		
				fixed-bed reactor [d] (measured)	membrane reactor [e] (calculated)	membrane reactor [f] (measured)
0	4.06	0.00	0	15.4	15.4	-
20	4.06	0.77	19	15.4	19.4	20.5
50	4.06	1.02	25	15.4	20.4	22.8
100	4.06	2.27	55	15.4	29.0	28.5

[a] Quantified by TCD detector in GC instrument; [b] Determined by mass spectrometer instrument; [c] Divided [a] by [b]; [d] Quantified by TCD detector in GC instrument (calculated based on method in Appendix A); [e] Theoretical calculation based on a and c; [f] Quantified by TCD detector in GC instrument (calculated based on method in Appendix A)

A control experiment was done by co-feeding H_2 in the CH_4 feed to examine the influence of H_2 addition through the membrane reactor. A fixed-bed reactor was used for testing the influences of H_2 co-feeding in the reactant stream on methane conversion and product selectivity in non-oxidative activation of methane over Fe/SiO_2 catalyst. The experimental conditions were the same as those set for DNMC reactions in the fixed-bed reactor at different reaction temperatures discussed above, except that a fraction of H_2 was added in the feed stream.

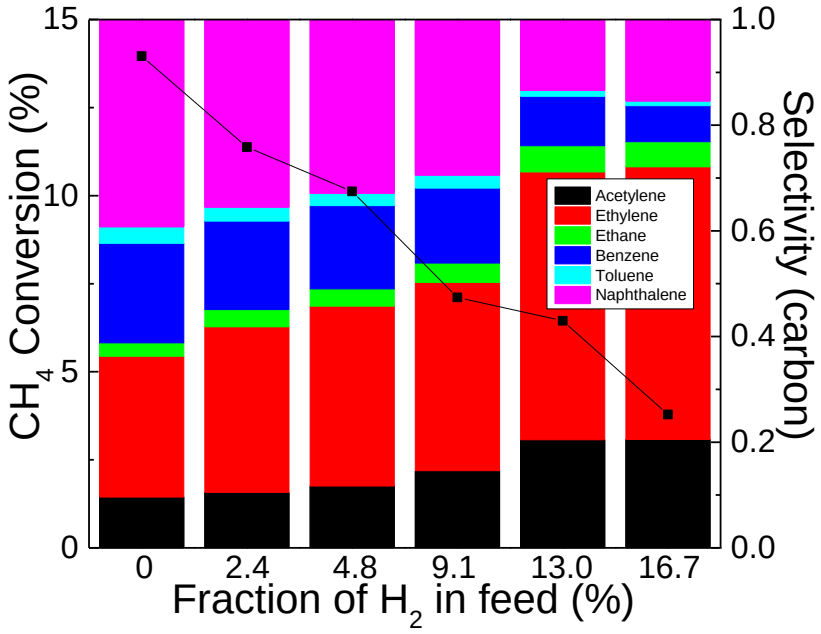

Figure 3.6. Methane conversion and product selectivity over Fe/SiO_2 catalyst in a fixed-bed reactor at different H_2 composition in methane feed (temperature = 1303 K, space velocity = 3200 $mL \cdot g^{-1} \cdot h^{-1}$).

Figure 3.6 shows the measured CH_4 conversion and product selectivity when the fraction of H_2 was varied from 0% to 16.7% in the feed stream. The increase in H_2 concentration in the feed stream increased the C_2 (acetylene, ethylene and ethane) selectivity from ~60% to ~85%, while the methane conversion was decreased from ~15% to 4%. In comparison to the H_2 addition into the reactor on the permeate sweep side (data shown in **Figure 3.5(B)**), the increase in C_2 selectivity with H_2 on feed side significantly decreased the methane conversion. Overall, the H_2 permeable membrane reactor shows a great potential in shifting the product selectivity to C_2 products while maintaining methane conversion (i.e., product yield) in the non-oxidative methane conversation chemistry. To significantly mitigate naphthalene formation, a concentration of ~15% H_2 in the CH_4 feed was needed, which led to a severe reduction in CH_4 conversion.

The slight sacrifice of CH_4 conversion but tuning product to C_2 and benzene compared to naphthalene is unique for the DNMC reaction in the H_2 permeable $SrCe_{0.7}Zr_{0.2}Eu_{0.1}O_{3-\delta}$ membrane reactor. On the other hand, an increase in CH_4 conversion and aromatic product formation were achieved with the H_2 permeable membrane reactor with He sweep gas flow. Both ends of products are attractive chemicals used in industry. The employment of the H_2 permeable membrane reactor in the present study could shift the building block supplies from the CH_4 catalysis chemistry.

The stability of the Fe/SiO_2 catalyst in DNMC reaction in the H_2 permeable membrane reactor was tested by running the reaction at 1303 K for 60 hours. No obvious deactivation was observed during this test (**Figure 3.7**). The CH_4 conversion remained at ~18% throughout this run at this tested reaction condition. Selectivities to C_2 (33%) and aromatics (64%) were constant, and the total selectivity to these products remained >97%. In contrast, H_2 removal resulted in accelerated coking on the Mo/ZSM-5 catalyst in other membrane reactors.[89, 114] This has been a major obstacle to realize a practical DNMC reaction in H_2 permeable membrane reactors. In addition to the stability of the Fe/SiO_2 catalyst, this long-term test also demonstrated the stability of the $SrCe_{0.7}Zr_{0.2}Eu_{0.1}O_{3-\delta}$ tubular ceramic membrane reactor under reducing hydrocarbon atmosphere. The combination of high CH_4 conversion, high and tunable selectivity, and durability in the H_2 permeable membrane reactor is notable.

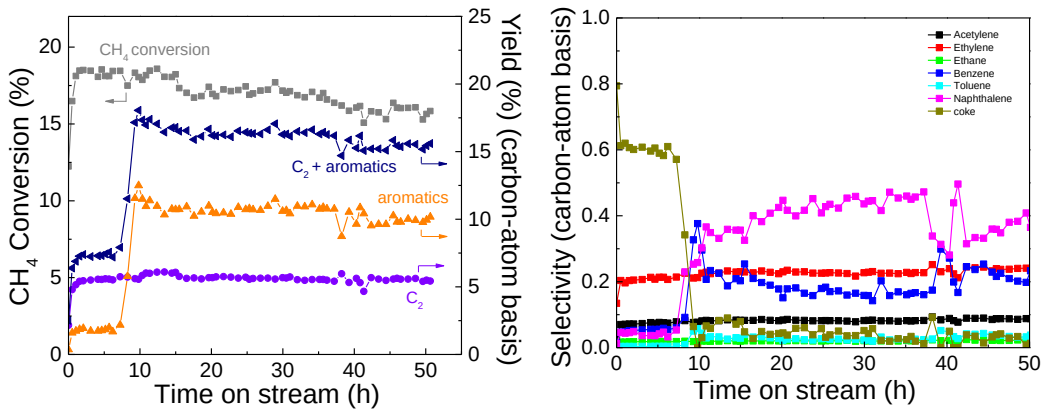

Figure 3.7. Long-term stability test of the packed-bed H_2 permeable tubular membrane reactor with the Fe/SiO_2 catalyst at 1303 K and 3200 $mL \cdot g^{-1} \cdot h^{-1}$ space velocity.

3.3.3. Stability of catalyst and membrane material at operating temperatures. In order to test the stability of both Fe/SiO_2 and $SrCe_{0.7}Zr_{0.2}Eu_{0.1}O_{3-\delta}$ membrane reactor materials at the reaction temperatures, the catalyst loaded membrane reactor were assembled and tested for DNMC reaction at 1323 K for 24 hours. Afterwards, the membrane reactor was regenerated by flowing air through to burn off the carbon species in the reaction system. The used catalyst and membrane reactor were taken for XRD measurement. For comparison, the as-prepared fresh Fe/SiO_2 catalyst and $SrCe_{0.7}Zr_{0.2}Eu_{0.1}O_{3-\delta}$ membrane materials were examined with XRD measurement. **Figure 3.8** shows the XRD patterns of the catalyst and membrane before and after the DNMC catalysis test. Both XRD patterns, either for Fe/SiO_2 or $SrCe_{0.7}Zr_{0.2}Eu_{0.1}O_{3-\delta}$, show no difference, which proves that both the Fe/SiO_2 and the $SrCe_{0.7}Zr_{0.2}Eu_{0.1}O_{3-\delta}$ membrane reactor are stable at 1303 K reaction temperature.

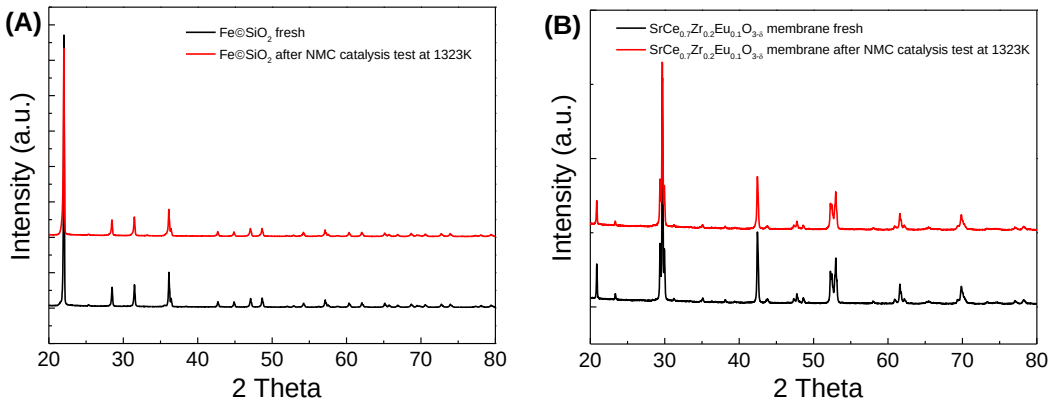

Figure 3.8. XRD patterns of fresh and used (A) Fe/SiO_2 and (B) $SrCe_{0.7}Zr_{0.2}Eu_{0.1}O_{3-\delta}$ membrane reactor materials (1303 K for 24 hours).

3.4 Conclusion of Chapter 3

In summary, the integration of a mixed ionic-electronic H_2 permeable $SrCe_{0.7}Zr_{0.2}Eu_{0.1}O_{3-\delta}$ membrane and Fe/SiO_2 catalyst into a catalytic tubular membrane reactor was demonstrated for the first time for DNMC reaction. The removal of H_2 from DNMC reactions led to a significant increase in CH_4 conversion. The product selectivity to C_2 and aromatics as well as catalyst durability were not influenced significantly by the H_2 removal, which is distinctly different from all the previous studies[89, 114] on H_2 permeable membrane reactor for DNMC reactions. The present work is the first successful demonstration of the H_2 permeable ceramic membrane reactor on shifting reaction equilibrium to benefit CH_4 conversion while not impacting product selectivity and catalyst durability in DNMC reactions. The capability of tuning products towards C_2 (ethylene and acetylene) or aromatic (benzene and naphthalene) products with high single pass yields open up new possibilities for DNMC processes. The integration of Fe/SiO_2 catalyst in the high temperature H_2 permeable

$SrCe_{0.7}Zr_{0.2}Eu_{0.1}O_{3-\delta}$ tubular membrane reactor enables new routes for transformation of CH_4 into high value-added chemicals and fuels.

Chapter 4: Dual Utilization of Greenhouse Gases to Produce C_{2+} Hydrocarbons and Syngas in a Hydrogen-Permeable Membrane Reactor

4.1 Introduction

The increase in carbon dioxide (CO_2) emissions from the utilization of carbon-rich fossil fuels is a major contributor to climate change due to its greenhouse effects. Intensive research has been conducted during the past decades on CO_2 conversion to reduce CO_2 emissions in order to alleviate global climate change[128-134]. The catalytic hydrogenation of CO_2 into valuable hydrocarbon fuels/chemicals represents a promising route for CO_2 utilization[135-137]. However, the cost of hydrogen (H_2) generation is high, and H_2 storage and transport remain problematic. Thus, chemically transforming CO_2 is currently economically impractical.

The abundance of methane (CH_4), another major greenhouse gas, from resources such as shale gas and natural gas, creates tremendous potential to supply H_2 and C_{2+} (C_2 and aromatics) fuels and chemicals. However, the current state-of-the-art process for C_{2+} production utilizes steam reforming of CH_4 reaction to produce syngas (CO + H_2), followed by Fischer-Trøpsch process, leading to low carbon and energy efficiencies[6, 12, 100-102]. Direct conversion of CH_4 processes, such as oxidative coupling of CH_4 to C_{2+} hydrocarbons[103-105], and direct non-oxidative CH_4 conversion (DNMC) to H_2, light hydrocarbons and aromatics[11, 25, 38, 106, 138], have gained a lot of attention. Among all the processes, DNMC is simple, and selective toward the formation of C_{2+} hydrocarbons and H_2 without formation of oxidative (e.g.,

CO_2) products. The processes, however, are typically hindered by high rates of coke production, either in thermal pyrolysis[13, 18, 21, 22] or catalytic DNMC over molybdenum/zeolite catalyst[27, 48, 50, 52, 106, 139]. Moreover, thermodynamic equilibrium constrains CH_4 conversion which has prevented the commercialization of the DNMC process[13, 109].

In this chapter, we report a hydrogen-permeable tubular membrane reactor **(Figure 4.1)** for simultaneous upgrading of CO_2 and CH_4 into value-added products, i.e., C_{2+} and CO (or syngas). The membrane reactor is comprised of a mixed ionic-electronic conducting $SrCe_{0.7}Zr_{0.2}Eu_{0.1}O_{3-\delta}$ membrane with thickness around ~20 μm and an active surface area of ~12 cm^2. It is supported on a $SrCe_{0.8}Zr_{0.2}O_{3-\delta}$ porous tube (~0.90 cm in diameter) and closed at one end. As noted in our previous work[38, 74, 88, 96], such tubular membrane reactor design increases the hydrogen permeable surface area and avoids need for sealing of membrane in the high temperature reaction zone, leading to stable and high hydrogen permeation performance in catalytic reactions[30, 31]. The inner side (interior) of the membrane reactor is packed with a DNMC catalyst, iron/silica (Fe/SiO_2), for conversion of methane into C_{2+} hydrocarbons and hydrogen via the equation, $CH_4 = 3/52\ C_6H_6 + 5/104\ C_{10}H_8 + 7/104\ C_2H_4 + 2/104\ C_2H_2 + 19/13\ H_2$. On the opposite side (outer surface) of the membrane reactor, the reverse water gas shift (RWGS) reaction (i.e., $CO_2 + H_2 = CO + H_2O$) takes place to convert the permeated H_2 and CO_2 sweep into CO and water (H_2O). The control of CO_2 concentration in the sweep side tunes the conversion of hydrogen permeate and thus creates the potential for production of syngas from CO product and unreacted hydrogen permeate. As shown in **Figure 4.1**, the tubular hydrogen-permeable membrane reactor

achieves the dual production of higher hydrocarbons and CO (or syngas) from two major global greenhouse gases, CH_4 and CO_2. Moreover, the thermodynamic equilibrium is shifted due to *in-situ* transfer of H_2 from feed to the permeate side of the membrane. The requirement for H_2 supply for CO_2 conversion is resolved since CH_4 functions concurrently as a H_2 source and feedstock for C_{2+} hydrocarbons.

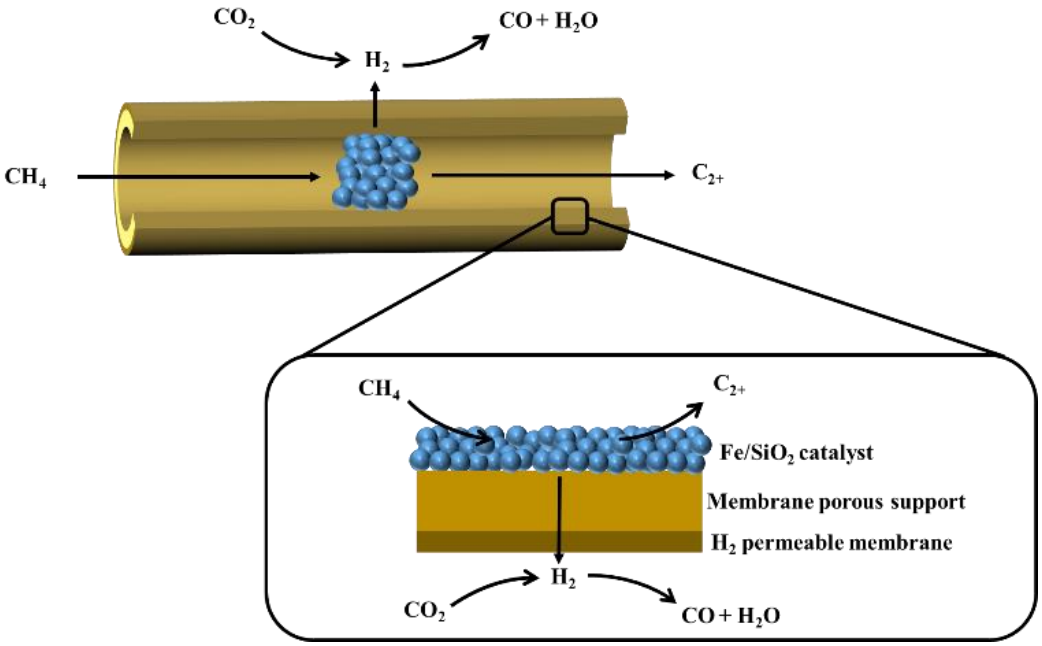

Figure 4.1. Schematic of tubular H_2 permeable membrane for dual production of value-added hydrocarbons and syngas from DNMC and RWGS reactions on opposite sides of the membrane.

$SrCe_{0.7}Zr_{0.2}Eu_{0.1}O_{3-\delta,}$ a mixed ionic-electronic conductor, with high ionic and electronic conductivities was utilized for this research. The combination of primarily protonic and electronic conductivity results in lattice diffusion of hydrogen from the CH_4 feed side to the CO_2 sweep side with essentially infinite selectivity. To a smaller extent $SrCe_{0.7}Zr_{0.2}Eu_{0.1}O_{3-\delta}$ also has oxygen-ion conductivity which combined with

electronic conductivity results in lattice diffusion of oxygen from the CO_2 sweep side to the CH_4 feed side that can minimize or prevent coke formation during the DNMC reaction. Similar membranes were employed previously in our group for water gas shift (WGS)[76, 88, 140] and CO_2 reforming of CH_4 reactions[96]. The hydrogen-permeable membrane reactor was prepared by tape casting of the $SrCe_{0.8}Zr_{0.2}O_3$ slurry and rolling end-capped tubular-type supports, and then followed by colloidal coating of a thin dense $SrCe_{0.7}Zr_{0.2}Eu_{0.1}O_{3-\delta}$ layer on the supports. Details on the synthesis of the membrane materials and the fabrication of the membrane reactor are described in previous publication[38, 96, 125].

The Fe/SiO_2 catalyst utilized in this research is based on the work of Guo et al.[55] wherein the DNMC reaction over Fe/SiO_2 in the temperature range of 1173K-1373 K produces ethylene and aromatic products with negligible coke formation when reaction temperature and space velocity are properly controlled. From TEM, iron oxide nanoparticles in the range of 3-4 nm are distributed homogeneously throughout the catalyst.[55] The embedment of iron oxide species within the silica matrix through bonding of C and Si atoms has also been verified.[55] The isolation of the iron atoms in the silica matrix achieves high selectivity toward hydrocarbons and prohibits coke formation under extreme temperature conditions. In this work, the Fe/SiO_2 catalyst was prepared by ball milling of a mixture of Fe_2SiO_4 and SiO_2 for 12 hours, followed by fusing at 1973 K for 6 hours. Ball milling was utilized in order to homogeneously mix the Fe_2SiO_4 and SiO_2 particles. Fe_2SiO_4 was prepared via the sol-gel method published by DeAngelis et al[98]. XRD and BET measurements of our Fe/SiO_2 can be found in the previous report.[38] The tests for leakage, hydrogen permeation and DNMC

reactions in the tubular membrane reactors were described in details in our previous work[38].

4.2 Experiments

4.2.1. H_2 permeation and Leakage tests for H_2 permeable tubular membrane reactor. Prior to the usage of the H_2 permeable membrane reactor for DNMC over Fe/SiO_2 catalyst, the membrane reactor underwent leakage and H_2 permeation tests. The tubular membrane reactor was used for these experiments. The feed side (inside of the membrane) was exposed to H_2 diluted to the tested concentration using Ar tracer. The total flow rate of the feed gas (mixture of H_2 and Ar) was set at 20 $mL \cdot min^{-1}$. The sweep side (outside of the membrane) was exposed to He at 20 $mL \cdot min^{-1}$, and connected to a gas chromatography (Agilent 6890) for quantifying the permeated H_2. **Figure 4.2** shows the assembly of H_2-permeable membrane reactor for the permeation tests. In addition to being a diluent, the Ar in the feed gas was used as a tracer. A leak will be indicated by an increase in Ar signal in the gas chromatography. A CO_2 leakage test was also performed on the H_2 permeable tubular membrane reactor. The procedure is similar to the H_2 permeation test, but with CO2/He mixtures in the feed gas.

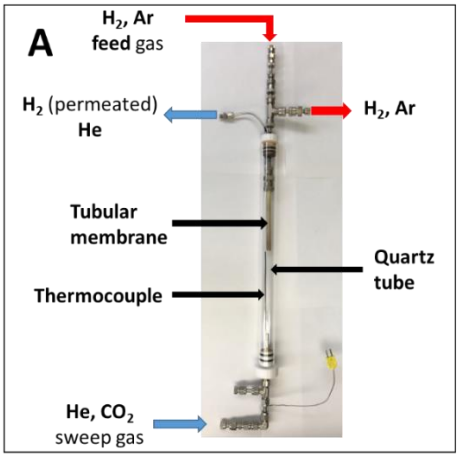

Figure 4.2. The assembly of H_2-permeable membrane reactor for the permeation tests

4.2.2. DNMC reaction in fixed-bed and H_2 permeable $SrCe_{0.7}Zr_{0.2}Eu_{0.1}O_{3-\delta}$ membrane reactors. The DNMC reaction was run at atmospheric pressure in either a fixed-bed (without H_2 permeation, **Figure 4.3(B)** or tubular membrane reactor (with H_2 permeation, **Figure 4.3(A)**). In a typical experiment, 0.375 g of catalyst was loaded at the center of the reactor and then heated to the desired temperature in pure Ar at the rate of 20 $mL \cdot min^{-1}$. After the reaction gas mixture (90%CH_4-10%Ar) was introduced, the reaction was run at the temperature range of 1223-1323 K and at a feed gas space velocity of 3200 $mL \cdot g^{-1} \cdot h^{-1}$. During the reaction in the tubular membrane reactor, the sweep gas, mixture of CO_2 and He, was introduced. The reactant (CH_4 mixed with a 10 mol% Ar tracer) was introduced through the inner tube in the top center section of the reactor and the products exited through the top left side of the reactor. The outer annular region of the membrane reactor was exposed to CO_2/He sweep gas to carry the permeated H_2 away from the reactor system or to feed H_2 into the reactor system. The effluent gases from the feed side and the sweep side were analyzed on-line by Agilent 6890 Gas Chromatograph to determine the CH_4 conversion and product selectivity.

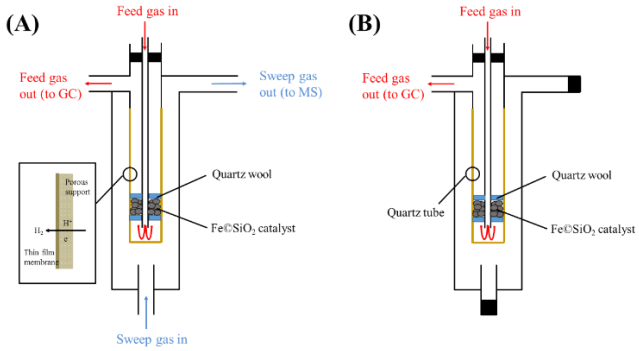

Figure 4.3. Detailed reactor set-up for (A) H_2 permeable $SrCe_{0.7}Zr_{0.2}Eu_{0.1}O_{3-\delta}$ membrane reactor and (B) fixed-bed reactor.

4.3 Results and Discussions

4.3.1 H_2 permeation and CO_2 leakage through the $SrCe_{0.7}Zr_{0.2}Eu_{0.1}O_{3-\delta}$ tubular membrane reactor. The H_2 permeation through the $SrCe_{0.7}Zr_{0.2}Eu_{0.1}O_{3-\delta}$ membrane in the membrane reactor was measured prior to the catalysis tests. **Figure 4.4(A)** shows that the permeated H_2 flux was increased with the H_2 concentration on the feed side. In addition, the H_2 permeation flux increased as the temperature increased due to the increase in ambipolar ionic/electronic conductivity of the $SrCe_{0.7}Zr_{0.2}Eu_{0.1}O_{3-\delta}$ membrane.

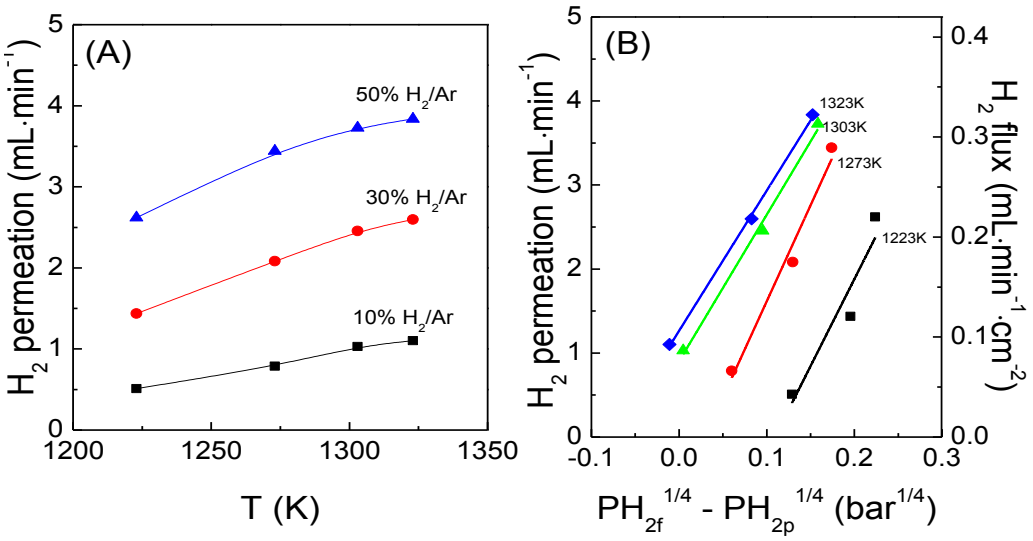

Figure 4.4. H_2 permeation flux through $SrCe_{0.8}Zr_{0.2}O_{3-\delta}$ membrane in the packed-bed membrane reactor as a function of temperature (A) and H_2 partial pressure (B), respectively.

The CO_2 leakage test was performed at the DNMC operating temperature (1303 K). In the experiment, the feed side (inside of the membrane) was exposed to 5%N_2-He gas. N_2 acted as the internal standard for the GC in order to quantify the amount of CO_2 leakage. The total flow rate of the feed gas was set at 20 mL·min^{-1}. The sweep side (outside of the membrane) was exposed to CO_2-He at 20 mL·min^{-1} at different CO_2 concentrations. The effluent of the feed side was connected to a gas chromatography (Agilent 6890) for quantifying the CO_2 leakage. **Table 4.1.** summarizes the amount of CO_2 leakage at different CO_2 concentrations on the sweep side.

Table 4.1. CO_2 leakage at different CO_2 concentrations.

CO_2 concentration in the sweep gas He : CO_2 ($mL \cdot min^{-1}$)	Amount of CO_2 leakage in the feed side ($mL \cdot min^{-1}$)
19 : 1	0.03
17 : 3	0.06
15 : 5	0.10
10 : 10	0.17
0 : 20	0.31

From **Table 4.1**, it can be seen that a small CO_2 leakage from the sweep side to the feed side was observed at all concentrations. The overall leakage was lower than 3% for all CO_2 concentrations. Understandably, an increase in CO_2 concentration in the sweep side led to a higher CO_2 leakage in the feed side. This CO_2 leakage contributed partly to the CO formation in the feed side. In addition, $SrCe_{0.7}Zr_{0.2}Eu_{0.1}O_{3-\delta}$ membrane can also act as an oxygen-permeable membrane at high temperatures. Therefore, small amount of CO was observed as byproduct on the feed side when CO_2 is included on the sweep side at all concentration.

4.3.2 Coke formation analysis. To quantify the coke formed in DNMC reaction in both membrane and fixed-bed reactors, analysis based on the carbon balance between CH_4 consumption and C_{2+} products formation was used. An example calculation can be found in **Appendix A**. In addition, the weighing method was used to confirm the amount of coke formed. The mass of the tubular membrane reactor with the Fe/SiO_2 was measured before and after the DNMC reaction. The weight difference was

attributed to the amount of coke formed during the DNMC reaction. One example of coke quantification using weight difference method is shown below.

Sample calculation of coke formation rate using weight-difference method:

Reaction condition: 1303 K, total reaction time = 12 hours
Mass of membrane reactor with catalyst before DNMC reaction: 13.3172 g
Mass of membrane reactor with catalyst after DNMC reaction: 13.4158 g
Average coke formation rate = $\frac{13.4158\text{g} - 13.3172\text{g}}{720\ \text{minute} * 12\ \text{g/mole}} = 1.14 \times 10^{-5}\ \text{mole}\cdot\text{min}^{-1}$

4.3.3 Performance of the $SrCe_{0.7}Zr_{0.2}Eu_{0.1}O_{3-\delta}$ tubular membrane reactor coupled with Fe/SiO_2 catalyst.

Figure 4.5 shows the effects of sweep gas types on DNMC in the inner side of the hydrogen-permeable membrane reactor, and compares to that of a fixed-bed reactor without hydrogen removal capability. **Figure 4.5(A)** shows an increase in CH_4 conversion was observed when comparing the quartz tube fixed-bed reactor to the membrane reactor with both helium (He) and CO_2 as sweep gas. Without a sweep gas, CH_4 conversion in DNMC in the membrane reactor was similar, albeit slightly higher (most likely due to higher catalytic activity of the ceramic tube surface as compared to non-catalytic quartz), to the case of fixed-bed reactor due to lack of a H_2 concentration gradient to drive H_2 removal. In accordance with Le Chatelier's principle, with a sweep gas simultaneous removal of H_2 from the membrane reactor shifts the reaction to the product side, and therefore increases the CH_4 conversion. In addition, the yield of all products also increased, especially for aromatics when comparing the membrane reactor with both helium (He) and CO_2 as sweep gas to the fixed-bed reactor. Based on **Figure 4.5(B)**, in further comparing the fixed-bed and hydrogen-permeable membrane

reactors, the membrane reactor with no sweep had slightly higher selectivity to benzene than ethylene with both having small selectivity toward coke formation. Adding the He sweep drove hydrogen permeation resulting in both greater CH_4 conversion and a small increase in coking at expense of naphthalene selectivity.

When CO_2 was used as sweep gas the least amount of coke was observed. However, a fraction of CO was observed as byproduct. This is due to the fact that $SrCe_{0.7}Zr_{0.2}Eu_{0.1}O_{3-\delta}$ membrane can also act as an oxygen-permeable membrane at high temperatures[72] so some of the carbon species can be oxidized to CO by the back diffusion of oxygen from the sweep side to the DNMC side. This co-permeation flux of H_2 and O_2 can be used to control or prevent coke formation as reported by Morejudo et al[35]. However, in contrast to that work we report a much simpler system that does not require use of electricity to drive the reaction (which given majority of current sources of electricity would generate additional CO_2). A similar idea was employed by Cao et al.[141] to supply O_2 to the DNMC reaction via the oxygen-permeable membrane to alleviate coke formation by forming CO. In addition, a small CO_2 leak from the permeated side of the membrane also contributed to the appearance of CO in the DNMC reaction side (interior) of the reactor (**Table 4.1**).

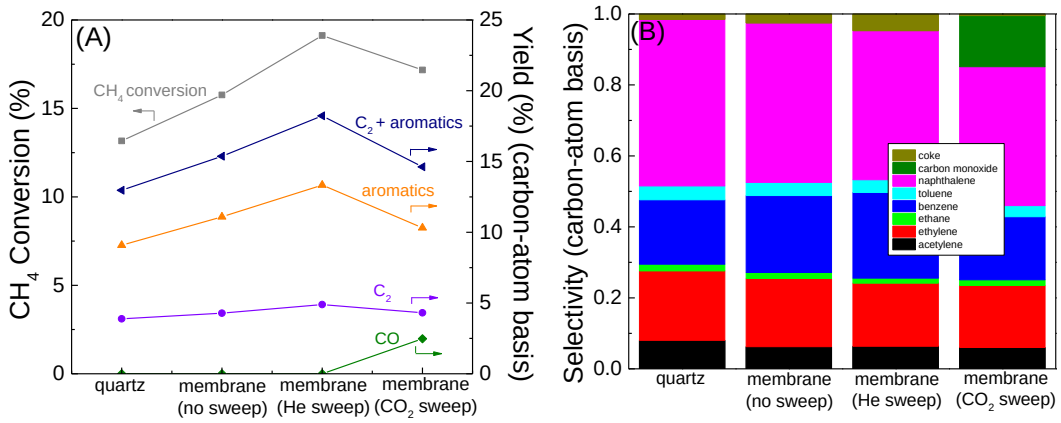

Figure 4.5. (A) CH_4 conversion and product yield over Fe/SiO_2 catalyst in fixed-bed reactor and membrane reactor with different sweep gases. (B) Product selectivity over Fe/SiO_2 catalyst in fixed-bed reactor and membrane reactor with different sweep gases. (Reaction condition: 1303 K, space velocity in DNMC reaction tests: 3200 $mL \cdot g^{-1} \cdot h^{-1}$, sweep gas flow rate: 20 $mL \cdot min^{-1}$, N_2 used as internal standard.)

The CH_4 conversion and DNMC product yield for different sweep side CO_2 concentrations are shown in **Figure 4.6(A)**. Similar CH_4 conversions were observed for all concentrations (5, 15, 25, 50 and 100 mol%, balanced by He) of CO_2 used in the sweep gas. This can be explained by two competing phenomena. First, the addition of CO_2 increases the partial pressure of O_2 on the sweep side, which decreases the ambipolar (electronic) conductivity of the membrane. This phenomenon leads to a decrease in H_2 flux and consequently less (Le Chatelier) enhancement of CH_4 conversion. However, the sweep side permeated H_2 readily reacts with the CO_2 sweep gas via the RWGS reaction to form CO, leading to an increase in the H_2 partial pressure gradient. Overall, as shown by CH_4 conversion, a decrease in the ambipolar conductivity of the membrane due to the higher oxygen partial pressure from CO_2 is offset by the increase in H_2 partial pressure gradient up to the 25% CO_2 sweep concentration and then the oxygen partial pressure dependence on ambipolar

conductivity starts to dominate up to 100% sweep CO_2 concentration. As shown in **Figure 4.6(B)**, the CO product selectivity increased with increasing sweep gas CO_2 concentration due both to greater co-flux of oxygen and any transmembrane CO_2 leakage. This also had benefit of reduced coke formation.

In terms of yield, the maximum C_2, aromatic, and C_{2+} single pass yields are 4.68%, 11.66%, and 16.34% at 25%CO_2. This compares favorably with DNMC single pass yields in the literature, which mainly are zeolite-based systems, where the hydrocarbon yield ranged from only 2 to 15%[30, 31, 36, 37, 60, 61, 89]. Even though the zeolite-based systems require lower operating temperatures compared to Fe/SiO_2 system, long-term performance was not stable due to coke formation.

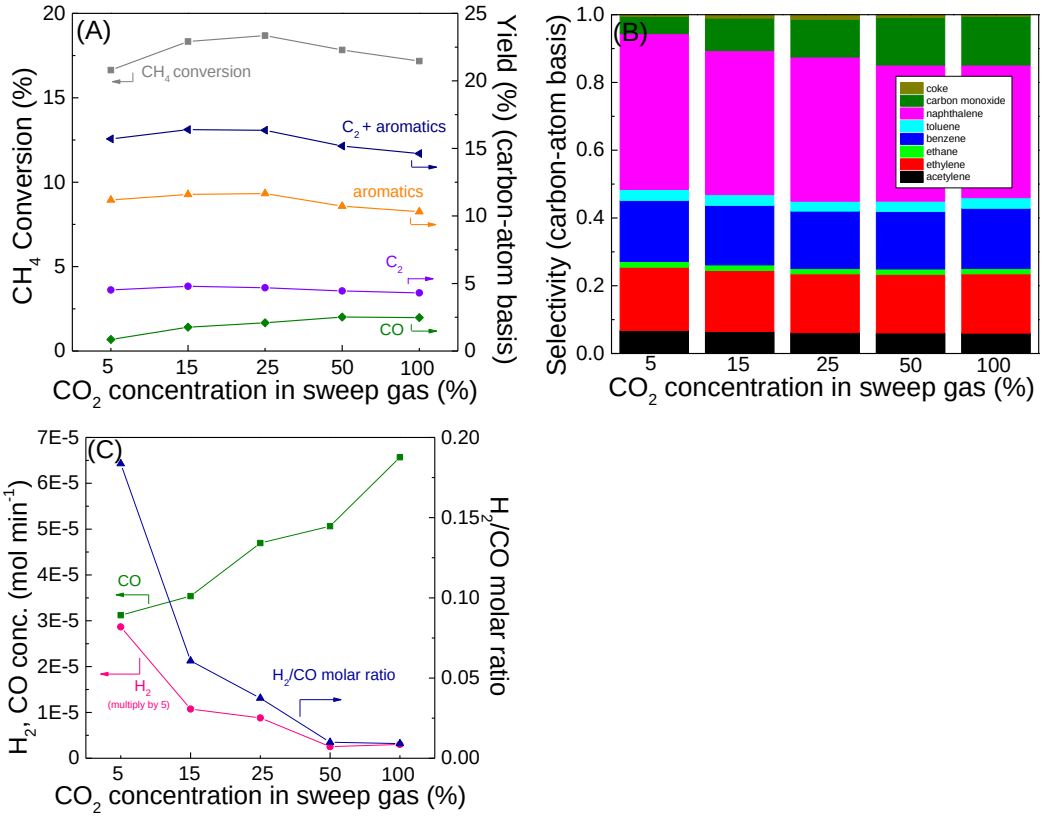

Figure 4.6. (A) CH_4 conversion and product yield in DNMC reaction side of the membrane reactor as a function of CO_2 concentration in the sweep side. (B) Product selectivity in DNMC reaction side of the membrane reactor as a function of CO_2 concentration in the sweep side. (C) H_2 and CO flow rates as well as H_2/CO molar ratio in the sweep side of the reactor. (Reaction condition: 1303 K, space velocity in DNMC reaction tests: 3200 $mL \cdot g^{-1} \cdot h^{-1}$, sweep gas flow rate: 20 $mL \cdot min^{-1}$, He used as balance gas in the sweep side, and N_2 used as internal standard.)

Compared to the oxidative coupling of methane (OCM) reaction, CH_4 conversion by this route is higher, ranging from 20-30%, with C_2 selectivity between 60-80% at the temperature ranges of 1073-1173K for the well-studied catalyst Mn_2O_3-Na_2WO_4/SiO_2[142]. However, atom efficiency (hydrocarbon products) of DNMC is superior compared to OCM, even though the C_2 yield might be higher for OCM under some operating conditions. Moreover, the undesirable oxidative products formed with OCM (e.g., CO_2) require additional downstream separation.

With our current system, the CH_4 conversion and resulting C_{2+} yields were limited by the membrane H_2 permeation flux. This is due primarily to the low porosity of the current membrane support resulting in gas diffusion limitations through the porous support. In other work by our group using a NiO-SCZ support tube where the NiO reduction provided porosity[125] (higher than this work), 40% of H_2 produced permeated through the membrane, compared to 25% (this work). In order to project the CH_4 conversion based on of membrane reactor with higher porosity of the support layer, the effect of the CH_4 conversion as a function of $\%H_2$ removal was calculated. Based on the experimental production selectivity of the fixed-bed reactor (no H_2 removal), the chemical reaction of DNMC can be calculated as follows

$$CH_4 = \frac{1}{10}C_2H_2 + \frac{6}{25}C_2H_4 + \frac{1}{50}C_2H_6 + \frac{1}{75}C_6H_6 + \frac{1}{700}C_7H_8 + \frac{19}{1000}C_{10}H_8 + \frac{2167}{1750}H_2 \quad (4.1)$$

Therefore, the equilibrium constant K, can be written as

$$K = \frac{\left(\frac{\frac{1}{10}X}{1+\frac{13272}{21000}X}\right)^{\frac{1}{10}} * \left(\frac{\frac{6}{25}X}{1+\frac{13272}{21000}X}\right)^{\frac{6}{25}} * \left(\frac{\frac{1}{50}X}{1+\frac{13272}{21000}X}\right)^{\frac{1}{50}} * \left(\frac{\frac{1}{75}X}{1+\frac{13272}{21000}X}\right)^{\frac{1}{75}} * \left(\frac{\frac{19}{1000}X}{1+\frac{13272}{21000}X}\right)^{\frac{19}{1000}} * \left(\frac{\frac{2167}{1750}X}{1+\frac{13272}{21000}X}\right)^{\frac{2167}{1750}}}{\left(\frac{1-X}{1+\frac{13272}{21000}X}\right)^{1}} \quad (4.2)$$

At 1303K, the CH_4 conversion of the fixed-bed reactor was at 14.2%, which gave the K value of 0.0272. For the case of H_2 removal, the value of K remains the same, while the concentration of H_2 in the equation changes. For example, at 10% H_2 removal, the equation for K becomes

$$K = \frac{\left(\frac{\frac{1}{10}X}{1+\frac{10672.6}{21000}X}\right)^{\frac{1}{10}} * \left(\frac{\frac{6}{25}X}{1+\frac{10672.6}{21000}X}\right)^{\frac{6}{25}} * \left(\frac{\frac{1}{50}X}{1+\frac{10672.6}{21000}X}\right)^{\frac{1}{50}} * \left(\frac{\frac{1}{75}X}{1+\frac{10672.6}{21000}X}\right)^{\frac{1}{75}} * \left(\frac{\frac{19}{1000}X}{1+\frac{10672.6}{21000}X}\right)^{\frac{19}{1000}} * \left(\frac{0.9*\frac{2167}{1750}X}{1+\frac{10672.6}{21000}X}\right)^{\frac{2167}{1750}}}{\left(\frac{1-X}{1+\frac{10672.6}{21000}X}\right)^{1}} \quad (4.3)$$

At K equals to 0.272 and with 10% H_2 removal, CH_4 conversion increases from 14.2% to 15.2%.

Figure 4.7. shows the increase in CH_4 conversion as a function of $\%H_2$ removal based on the above calculation.

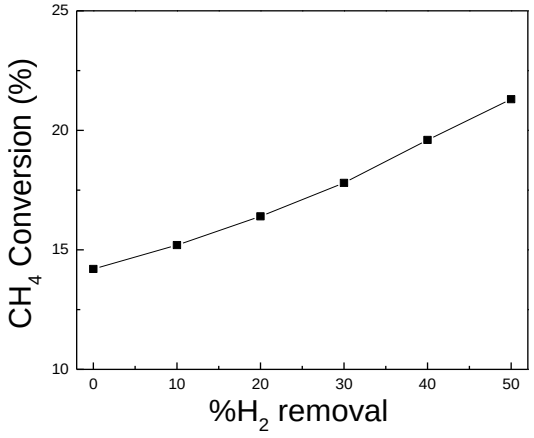

Figure 4.7. CH_4 conversion calculation as a function of $\%H_2$ removal at 1303 K and space velocity of 3200 $mL \cdot g^{-1} \cdot h^{-1}$.

If similar porosity support tubes were used here we project a CH_4 conversion and C_{2+} yield of 20% and 18% respectively, assuming similar product distribution. This would also significantly increase H_2/CO ratio on the sweep side.

Overall, on the feed side with 25%CO_2-He sweep at 1303 K, for every 1 mole of CH_4 converted, 0.200 mol of C_{2+}, 0.113 mol of CO, 0.013 mole of coke, and 1.036 mol of H_2 are produced. On the sweep side the permeated H_2 consumed 0.340 mol of CO_2 producing another 0.340 mol of CO per mole of CH_4 converted on the feed side. Therefore, each mole of CH_4 consumed produces 0.200 mol of C_{2+} (0.875 mole-C) and

0.453 mol of CO resulting in 1.328 mol-C total carbon products due to the dual utilization of CH_4 with CO_2 sweep.

Figure 4.6(C) shows the catalytic results from RWGS reaction on the sweep side of the $SrCe_{0.7}Zr_{0.2}Eu_{0.1}O_{3-\delta}$ tubular membrane reactor. As H_2 permeates through the membrane from the DNMC reaction side, it readily reacts with CO_2 in the sweep gas to form CO and H_2O. As the concentration of CO_2 in the sweep gas increased, the CO formation increased due to more reaction between H_2 permeate and CO_2 in the sweep gas. As a result, the H_2 concentration in the effluent in sweep side decreased. **Figure 4.6(C)** also shows the H_2/CO ratio decreased as the concentration of CO_2 increased in the sweep gas since there were more CO and less H_2. This offers the capability of tuning syngas ratio by simply varying CO_2 concentration in the sweep side in the $SrCe_{0.7}Zr_{0.2}Eu_{0.1}O_{3-\delta}$ tubular membrane reactor. Clearly, in one single membrane reactor, we successfully integrated two reactions from opposite sides of the membrane to produce C_{2+} hydrocarbon and CO (or syngas) from CH_4 and CO_2 feedstocks. The membrane itself is capable of H_2 separation from DNMC reaction and catalysis for RWGS, as well as tailoring the H_2/CO ratio in syngas by manipulating CO_2 concentration in sweep side.

4.3.4 Performance of the $SrCe_{0.7}Zr_{0.2}Eu_{0.1}O_{3-\delta}$ material as catalyst RWGS reaction.

To verify the catalysis function of the $SrCe_{0.7}Zr_{0.2}Eu_{0.1}O_{3-\delta}$ membrane material for RWGS reaction, a control experiment employing $SrCe_{0.8}Zr_{0.2}O_{3-\delta}$ powder in a fixed-bed reactor was carried out at the same reaction condition as that used for the membrane reactor. The RWGS reaction over a typical catalyst, Ni/Al_2O_3, was also examined for comparison. In a typical experiment, 0.375 g of $SrCe_{0.8}Zr_{0.2}O_{3-\delta}$ powder was loaded at

the center of the reactor and then heated to the desired temperature in pure Ar at the rate of 20 $mL \cdot min^{-1}$. After the reaction gas mixture (CH_4-H_2-Ar mixture) was introduced, the reaction was run at the temperature of 1303 K and at a total feed gas space velocity of 3200 $mL \cdot g^{-1} \cdot h^{-1}$. The H_2 flow rate was kept at 1 $mL \cdot min^{-1}$, while the flow rate of CO_2 was varied. Ar was used as a diluent to maintain the overall flow rate of 20 $mL \cdot min^{-1}$. The product effluents were analyzed on-line by Agilent 6890 Gas Chromatograph to determine the CO_2 and H_2 conversion and CO formation. **Figure 4.8** demonstrates the activity of the RWGS reaction over the $SrCe_{0.8}Zr_{0.2}O_{3-\delta}$ membrane powder using a fixed-bed reactor at 1303 K. The H_2 conversion **(Figure 4.8(A))**, CO_2 conversion **(Figure 4.8(B))**, and CO formation **(Figure 4.8(C))** of $SrCe_{0.8}Zr_{0.2}O_{3-\delta}$ was compared to a typical catalyst, Ni/Al_2O_3[143-145], for RWGS, and a blank reactor. From **Figure 4.8(A)**, it can be seen that $SrCe_{0.8}Zr_{0.2}O_{3-\delta}$ exhibits a significantly higher H_2, and conversion when compared to blank reactor, and similar activity when compared to the Ni/Al_2O_3 catalyst. The conversion increases as the concentration of CO_2 increases. The opposite trend can be observed for the CO_2 conversion shown in **Figure 4.8(B)**. As the concentration of CO_2 increases, the CO_2 conversion decreases. This is because there is not enough H_2 to reaction with CO_2 in order to maintain high conversion rates. **Figure 4.8(C)** shows the rate of CO formation as a function of CO_2 concentration. It can be seen that the catalysts, both $SrCe_{0.8}Zr_{0.2}O_{3-\delta}$ and Ni/Al_2O_3 exhibit higher rate of CO formation compared to a blank reactor. Since H_2 conversion increases as the concentration of CO_2 increases, CO formation also follows the same trend. Based on this data, it is clear that the surface of the membrane has the ability to catalyze the RWGS reaction, and therefore, additional catalyst is not required.

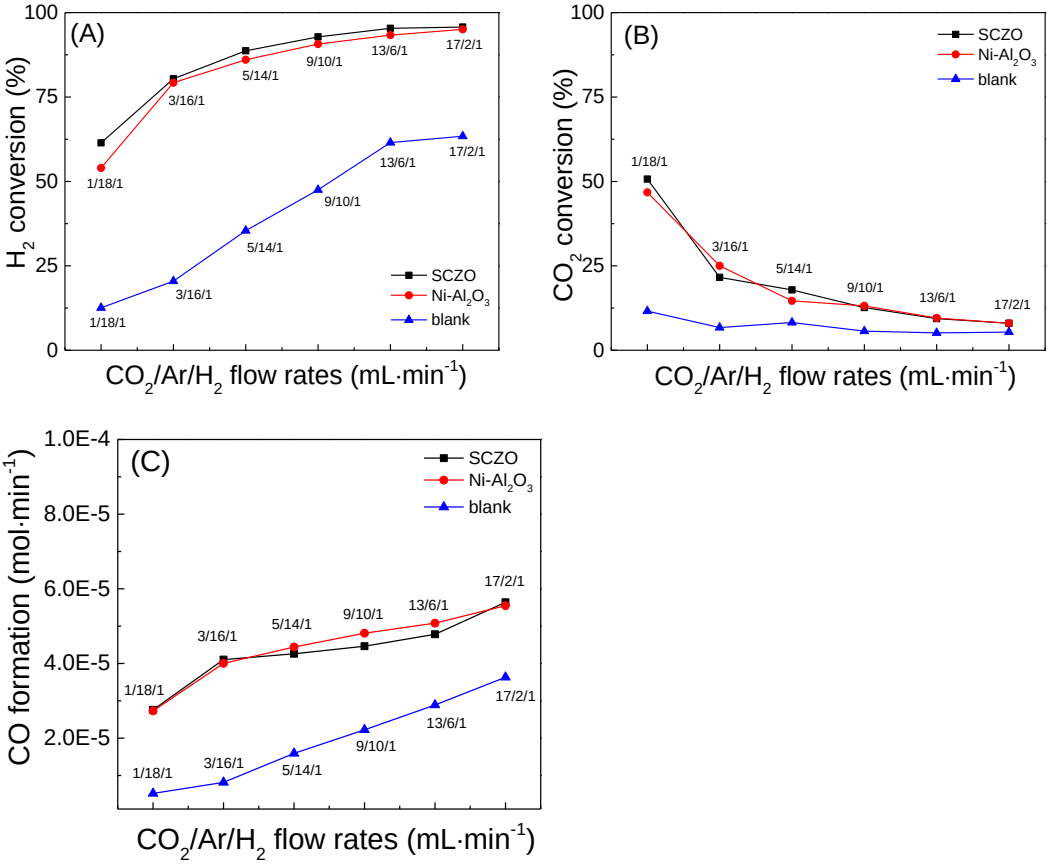

Figure 4.8. H_2 conversion (A), CO_2 conversion (B), and CO formation (C) for RWGS reaction in a fixed-bed reactor at 1303 K and space velocity of 3200 $mL \cdot g^{-1} \cdot h^{-1}$.

4.3.5 Long-term stability test of the hydrogen-permeable tubular membrane reactor for dual production of hydrocarbons and syngas

The stability of the $SrCe_{0.7}Zr_{0.2}Eu_{0.1}O_{3-\delta}$ tubular ceramic membrane reactor in dual DNMC and RWGS reactions was tested by running both reactions at 1303 K for 50 hours while flowing 25 mol% CO_2 (balanced by He) in the sweep gas. From **Figure 4.9(A)**, on the CH_4 conversion side, a slight change in catalytic performance in DNMC was observed in the initial stage of the reaction (induction period), i.e., up to time-on-stream (TOS) of ~10 h. CH_4 conversion started at ~18% and dropped to ~16% at TOS of 10 h. The coke formation rate was high at the beginning of the reaction, but decreased

with TOS dropping to nearly zero over the long-term reaction run (**Figure 4.10(A)**). The coke composition on the catalyst was analyzed by temperature programmed oxidation (TPO) experiment. Typically, the coked catalytic wall reactor was placed inside a temperature-controlled furnace. The temperature of the furnace was held constant by a Eurotherm Controller (2408 series). The catalyst temperature was monitored by a K-type thermocouple attaching to the outer wall of the catalytic wall reactor. The furnace was ramped to 1123 K at a ramp rate of 10 K min^{-1} under flowing He (35 mL min^{-1}, ultrapure, Airgas) and O_2 (5 mL min^{-1}, ultrapure, Airgas) atmosphere. The O_2-TPD profile was recorded using a mass spectrometer (ABB Extrel) during this step. The initial high coke formation is an induction period for both the Fe/SiO_2 catalyst and the membrane reactor. The induction of the Fe/SiO_2 is consistent with that observed by Guo et al.[55] and the oxide ion transport through the membrane from the CO_2 sweep, to prevent further coking, has an initiation time associated with establishing gas partial pressure equilibria on either side of the membrane. Overall, the coking/decoking events in the membrane reactor reached a balance, and thus a stable operation window for long-term tests. Analysis on the spent catalyst shows that the small amount of coke remaining on its surface is primarily comprised of elemental carbon[146], in both ordered and disordered formats (**Figure 4.10(B)**). The product yield analysis showed that C_2 (ethane, ethylene and acetylene) decreased with TOS from 0 to ~10 h, while aromatic (i.e., benzene and naphthalene) products exhibited the opposite trend. After TOS of ~10 h, the reaction achieved stable performance in which CH_4 conversion remained at approximately 16% throughout this run to TOS of ~50 h and yields to C_2, aromatics, C_{2+}, and CO were stable at approximately 4.0%, 9.8%,

13.8%, and 1.3%, respectively. The CO formation on the CH_4 side of membrane (**Figure 4.9(A)** and **4.9(B)**) is consistent with oxygen transport through the membrane from the CO_2 sweep that would limit further coke formation under steady state conditions. The coke selectivity in the DNMC side of the membrane reactor was analyzed based on the carbon balance between CH_4 consumption and C_{2+} products formation. An example calculation can be found in our previous report[38]. The overall coke formation was also confirmed by weighing method (**Section 4.3.2**). The same method has been used to quantify the coke selectivity presented in **Figure 4.5 and 4.6.** From **Figure 4.10(A)**, it can be seen that coke formation occurred almost entirely during the initial stage of reaction (≤10 hours). After the reaction reached this equilibria the coke formation rate was minimal demonstrating a decreasing trend in coke formation with TOS of the reaction which is quite different from other zeolite-based DNMC reactions in the literature that have continued issues with coke formation[31, 37, 89].

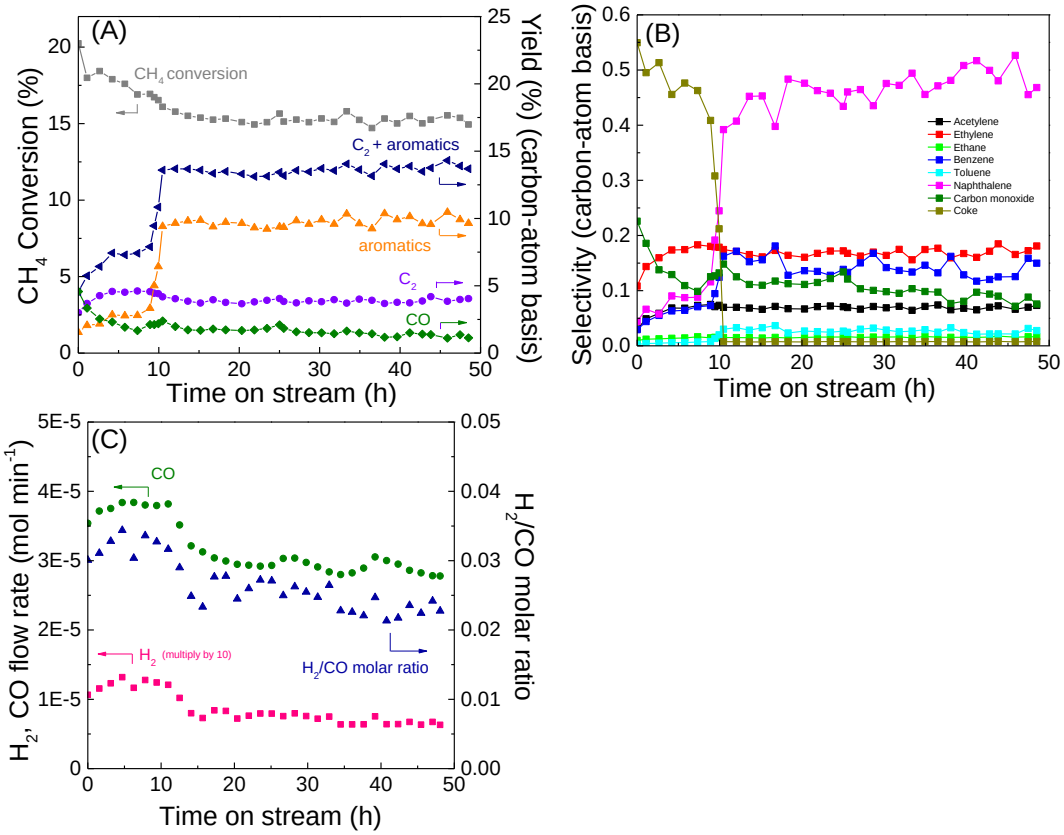

Figure 4.9. Long-term stability test of the hydrogen-permeable tubular membrane reactor for dual production of hydrocarbons and CO (or syngas) from DNMC (A) + (B), and RWGS (C) reactions on opposite sides. (Reaction condition: 1303 K, space velocity in DNMC reaction tests: 3200 $mL \cdot g^{-1} \cdot h^{-1}$, sweep gas flow rate: 20 $mL \cdot min^{-1}$, CO_2 concentration in the sweep side: 25%, balanced by He, and N_2 used as internal standard.)

On the CO_2 conversion side of the membrane reactor (**Figure 4.9(C)**), the RWGS reaction exhibits an obvious change at TOS of ~10 h, similar to that of DNMC reaction on the opposite side of the membrane. The CO formation rate was stable and relatively high before TOS of ~10 h, which gave a quite stable H_2/CO ratio at 0.030 in this TOS region. In the TOS range of 10-20 h, a decrease in CO formation rate and H_2/CO ratio was observed. In the last stage (up to TOS of 50 h), both CO formation and H_2/CO ratio seemed to reach an equilibria. In all the cases, the H_2 flow rate in the effluent stream of

the RWGS reaction was relatively low, indicating H_2 permeate was the limiting RWGS reactant and was consumed *in-situ* in the sweep side of the membrane reactor.

In addition to the transient initial stage of the reaction, long-term tests demonstrated the stability of both the Fe/SiO_2 catalyst and $SrCe_{0.7}Zr_{0.2}Eu_{0.1}O_{3-\delta}$ membrane (and catalyst for RWGS) under CO_2 atmosphere. This is due mainly to the addition of zirconium dopant in the B-site, which increase the structural stability of the perovskite with regard to CO_2[72, 88, 147, 148]. This combination of high CH_4 conversion, high and tunable selectivity of C_2 and aromatics, high production rate of synthesis gas, and durability in the H_2 permeable membrane reactor is unique among the DNMC literature and the first using CO_2 as a membrane reactor sweep gas.

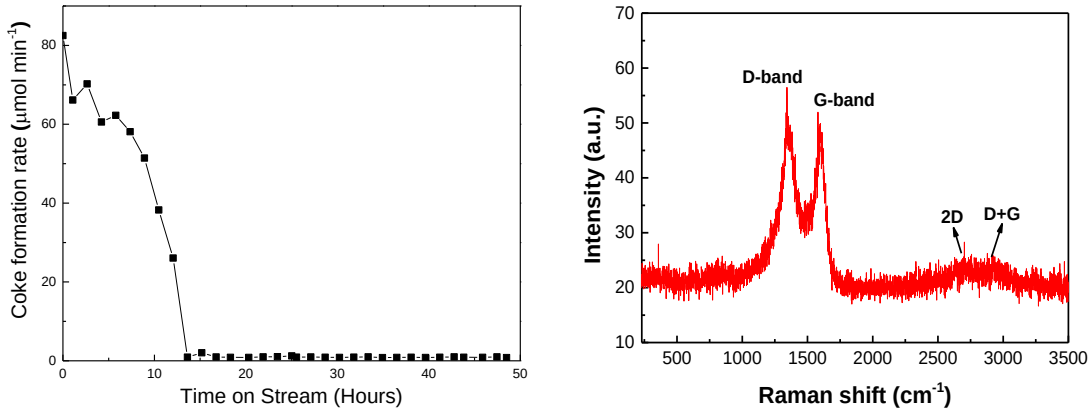

Figure 4.10. (A) Coke formation rate as a function of time-on-stream in DNMC and RWGS reactions in the membrane reactor. (Reaction condition: 1303 K, space velocity in DNMC reaction tests: 3200 $mL \cdot g^{-1} \cdot h^{-1}$, sweep gas flow rate: 20 $mL \cdot min^{-1}$, CO_2 concentration in the sweep side: 25%, balanced by He, and N_2 used as internal standard.) (B) Raman spectroscopy of spent Fe/SiO_2 catalyst in DNMC reactions. (Reaction temperature = 1273 K, total gas flow rate = 20 mL min^{-1}, CH_4:N_2 = 9:1, 1 atm pressure).

CO_2 and CH_4 are the two largest GHG contributors to climate change. Due to recent advancements in oil and gas extraction technologies, the production of natural gas has increased significantly leading to natural gas supplies from previously unattainable extraction sites. Further, methane is often flared or vented at remote oil production sites.[149] Leaked, flared, and/or vented methane represent environmental harm and lost opportunity, while stranded gas represents lost opportunity and reduced domestic energy security. Therefore, the utilization of CH_4 for both energy and chemical production would lead to potentially greater GHG emissions with conventional state-of-the-art CH_4 conversion technologies, which go through the synthesis gas production step via the steam reforming of CH_4 thus producing CO_2 as an unwanted byproduct. By coupling CH_4 conversion via DNMC with CO_2 conversion to CO via RWGS in an integrated DNMC-catalyst/hydrogen-permeable membrane reactor we create the potential to significantly reduce two of the greatest contributors to climate change. First, the membrane reactor allows for the *in situ* removal of H_2 from the effluent gas, circumventing thermodynamic limitations and leading to higher CH_4 conversion to C_{2+} hydrocarbons without producing CO_2, contrary to current technology. Second, the fact that CO_2 is used as a sweep gas and converted to CO by reacting with the permeated H_2 simultaneously transforms this GHG to a value added product. Therefore, overall, the membrane reactor system produces value added chemicals such as C_{2+} and synthesis gas, while reducing GHG emissions from abundant natural gas resources and CO_2 emissions. The one-step membrane reactor is modular and highly scalable, so it can fit the desired application with increasing number of production units. The CO_2 released by chemical and allied industries can be upgraded

via the membrane reactors, potentially reducing 0.23 GT of CO_2 emission per year if the reactor is fully deployed. Overall, the membrane reactor system achieves multiple functions in one integrated solution, i.e., dramatically increasing energy efficiency of a wide range of industrial and petrochemical processes, thus reducing GHG emissions and increasing energy security.

4.4 Conclusion of Chapter 4

In summary, a membrane reactor tube made from a protonic-electronic conducting $SrCe_{0.7}Zr_{0.2}Eu_{0.1}O_{3-\delta}$ thin-film deposited on a porous $SrCe_{0.8}Zr_{0.2}O_{3-\delta}$ support capable of hydrogen permeation and catalysis was explored for the first time for co-utilization of CH_4 and CO_2 greenhouse gases. On one side of the membrane tube, CH_4 upgrading to C_{2+} hydrocarbons was realized via DNMC reaction over the Fe/SiO_2 catalyst, with co-production of H_2 gas. On the opposite side, the hydrogen permeate reacted with CO_2 sweep to form CO and H_2O via the RWGS reaction. The *in-situ* removal of H_2 from DNMC shifted the reaction to high CH_4 conversion and heavier product formation, while the removed H_2 functions as an *in-situ* feedstock for hydrogenation of CO_2. Beyond the initial ($\leq$10 hr) transient, the long-time tests indicate that both reaction systems reached stabile conversion, selectivity, and thus product yield. The simple single membrane reactor tube packed with Fe/SiO_2 catalyst achieved simultaneous utilization of two major global greenhouse gases, i.e., CH_4 and CO_2, to produce value-added hydrocarbons and CO (or syngas), as well as the capability of tuning H_2/CO ratio in syngas by tailoring CO_2 concentration in the sweep side of the reactor.

Chapter 5: Autothermal Operation of the Direct Non-Oxidative Methane Conversion in a H_2-Permeable Membrane Reactor

5.1 Introduction

Methane is the main constituent of natural gas that is produced from gas, oil, and coalbed wells. In addition, the advancement in hydraulic fracturing technology has led to the utilization of new natural gas resources from the impermeable rocks of shale.[3] Commercially, the conventional technology consists of the conversion of CH_4 to synthesis gas (carbon monoxide (CO) + H_2) via the steam reforming of methane (SRM), followed by the Fischer-Tropsch synthesis to produce higher hydrocarbons, which led to low carbon efficiency due to the over oxidation to carbon dioxide (CO_2).[6, 12, 100, 101] In addition, the indirect route is very energy-intensive, and has high capital cost.[11, 12, 26] Recently, direct CH4 conversion paths have been explored, which include the oxidative coupling of CH_4 (OCM) to C_2 hydrocarbons (acetylene, ethylene, ethane)[103-105, 150, 151], and direct non-oxidative CH_4 conversion (DNMC) to H_2, C_2 hydrocarbons and aromatics (benzene, toluene, naphthalene).[11, 25, 35, 37, 38, 106, 138] Among all the approaches, DNMC is more simple and selective given its unique capability to form C_{2+} hydrocarbons (C_2 and aromatics) while circumventing the intermediate energy intensive steps[11, 12, 26], and avoiding the formation of over oxidation byproducts (CO, CO_2). However, the main drawbacks for the DMNC reaction is the thermodynamic limitations, and the high rate of catalyst deactivation due to carbon deposition.[6, 27, 50, 52, 106, 139] One of the promising solutions to circumvent the thermodynamic limitation by simultaneously remove H_2 from the effluent of the DNMC reaction via the utilization of the hydrogen-

permeable membrane reactor. In our previous report[38], significant improvement in CH_4 conversion was achieved upon H_2 removal from the membrane reactor compared to that in a fixed-bed reactor. The Fe/SiO_2 catalyst in the H_2 permeable membrane reactor demonstrated a stable performance with up to 30% CH_4 conversion and 99% selectivity to C_2 and aromatics.

Recently, Deckman et al.[152] proposed the utilization of a hydrogen-permeable membrane as a heat-exchange membrane for electrical power generation. On one side of the membrane, SRM reaction takes place at high temperature. The produced hydrogen permeates through the membrane, and combusts with oxygen (air) on the other side of the membrane. The steam generated from the combustion is used to drive a turbine. The product of the CH4/steam reaction contains mainly CO_2 at high pressure, which is ready for sequestration. However, the group has not reported the experimental results to demonstrate the performance of the heat-exchange membrane reactor.[152] Kniep et al.[153] applied the concept of the heat-exchange membrane to the SRM reaction. On one side of the membrane, the SRM reaction and the water-gas-shift (WGS) reaction took place over the Ni/Al_2O_3 catalyst to generation synthesis gas. A portion of the generated H_2 is transported through the dense $SrCe_0.75Zr_{0.2}Tm_{0.05}O_{3-\delta}$, which is then combusts with oxygen (or air) to form water. The heat released from the combustion of H_2 can be exchanged thermally through the $SrCe_{0.75}Zr_{0.2}Tm_{0.05}O3_{-\delta}$, which can be used to provide heat for the endothermic SRM reaction.

Heat-exchange membrane can also be applied to the DMNC reaction. On one side of the membrane, CH_4 is converted to C_2, aromatics, and H_2 over the Fe/SiO_2 catalyst. Some of the produced H_2 is permeated through the membrane, which is then

combusted with O_2 (air) to form water. The thermodynamic equilibrium is shifted due to *in-situ* transfer of H_2 from feed side to the permeate side of the membrane. In addition, the heat released from the H_2 combustion can provide heat for the endothermic DNMC reaction

In this chapter, we report a hydrogen-permeable tubular membrane reactor **(Figure 5.1)** as a heat-exchange membrane for the upgrading of CH_4 into valuable C_{2+} products. The tubular membrane reactor is comprised of a mixed ionic-electronic conducting $SrCe_{0.7}Zr_{0.2}Eu_{0.1}O_{3-\delta}$ membrane supported on a $SrCe_{0.8}Zr_{0.2}O_{3-\delta}$ porous tube coupled with a Fe/SiO_2 DNMC catalyst. The inside of the tubular membrane reactor is packed with the Fe/SiO_2 catalyst for DMNC reaction in order to convert CH_4 into C_{2+} hydrocarbons via the equation CH_4 = 3/52 C_6H_6 + 5/104 $C_{10}H_8$ +7/104 C_2H_4 +2/104 C_2H_2 + 19/13 H_2. On the outside of the membrane reactor, the exothermic combustion takes place to convert the permeated H_2 and O_2 (air) into water, which provide heat through the heat-exchange membrane for the endothermic DMNC reaction. Temperature, O_2 concentrations and flow rates of the sweep gas have effects on the permeated H_2, heat released from the H_2 combustion, and heat consumed by the DNMC reaction. As shown in **Figure 5.1**, the tubular hydrogen-permeable membrane reactor can theoretically achieve autothermal operation by utilizing the membrane reactor as a heat-exchange membrane. In addition, the thermodynamic equilibrium is shifted due to *in-situ* transfer of H_2 from feed to the permeate side of the membrane. The heat requirement for the endothermic DMNC reaction is provided by the heat release from the combustion of permeated H_2 with O_2 in the sweep gas. Even though it is not with

the application of a membrane reactor, the idea of autothermal operation for DNMC reaction has been studied in our group in a millisecond catalytic wall reactor.[146]

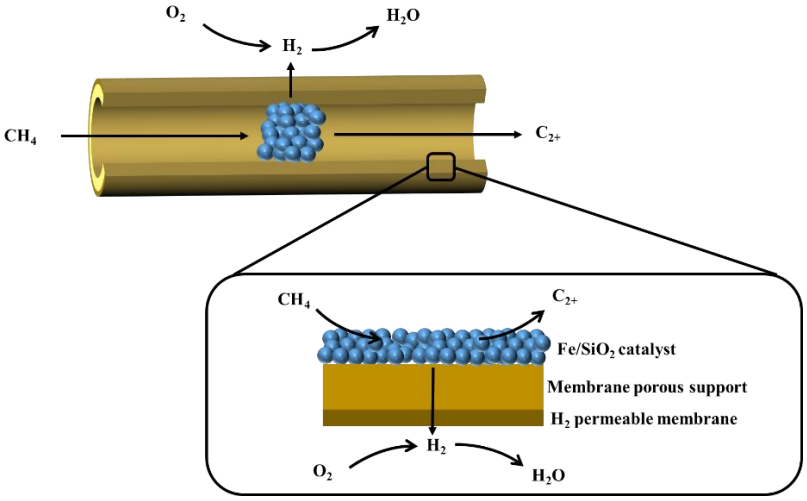

Figure 5.1. Schematic of the $SrCe_{0.7}Zr_{0.2}Eu_{0.1}O_{3-\delta}$ tubular membrane reactor as a heat-exchange membrane for DNMC reaction coupled with H_2 oxidation using O_2 as the sweep gas.

$SrCe_{0.7}Zr_{0.2}Eu_{0.1}O_{3-\delta}$ membrane was employed as the material for the tubular membrane reactor, which was coupled with the DNMC catalyst. $SrCe_{0.7}Zr_{0.2}Eu_{0.1}O_{3-\delta}$ is a perovskite-based material with high ionic and electronic conductivities, which results in the lattice diffusion of H2 from the effluent of the DMNC reaction (CH_4 side) to the sweep side (O_2 side). However, since $SrCe_{0.7}Zr_{0.2}Eu_{0.1}O_{3-\delta}$ is a mixed conductors, it has a small oxygen-ion conductivity, which results in lattice diffusion of oxygen from the O_2 sweep side to the CH_4 feed side. The diffusion of oxygen can help prevent or minimize carbon deposition during the DMNC reaction. In our group, similar type of membranes has been applied to water-gas-shift[76, 88, 140] and CO_2 reforming of methane[96] reactions. The H_2-permeable membrane reactor was prepared by tape casting of the $SrCe_{0.8}Zr_{0.2}O_3$ slurry and rolling end-capped tubular-type supports, and

then followed by colloidal coating of a thin dense $SrCe_{0.7}Zr_{0.2}Eu_{0.1}O_{3-\delta}$ layer on the supports. Details on the synthesis of the membrane materials and the fabrication of the membrane reactor are described in previous publication[38, 96, 125].

In this research, we utilized the Fe/SiO_2 catalyst for the DNMC reaction based on the work done by Guo et al.[55] As shown from TEM, the iron oxide nanoparticles are homogeneously distributed throughout the catalyst with the size ranges between 3-4 nm.[55] In addition, the iron oxide is embedded within the silica matrix through the bonding of C and Si atoms.[55] Because of increase in the stability of the iron oxide species in the silica matrix, high selectivity toward hydrocarbons and low coke formation can be achieved. For this work, the Fe/SiO_2 catalyst was synthesized by mixing Fe_2SiO_4 and SiO_2 for 12 hours via ball milling. Ball milling was utilized in order to homogeneously mix of the Fe_2SiO_4 and SiO_2 particles. Then, the mixture was fused at 1973 K for 6 hours. Fe_2SiO_4 was prepared via the sol-gel method published by DeAngelis et al.[98] XRD and BET measurements of our Fe/SiO_2 can be found in our previous report.[38] The tests for leakage, hydrogen permeation and DNMC reactions in the tubular membrane reactors were described in details in our previous work.[38]

5.2 Experiments

5.2.1. H_2 permeation and Leakage tests for H_2 permeable tubular membrane reactor. Prior to the usage of the H_2 permeable membrane reactor for DNMC over Fe/SiO_2 catalyst, the membrane reactor underwent leakage and H_2 permeation tests. The tubular membrane reactor was used for these experiments. The feed side (inside of the membrane) was exposed to H_2 diluted to the tested concentration using Ar tracer.

The total flow rate of the feed gas (mixture of H_2 and Ar) was set at 20 mL·min^{-1}. The sweep side (outside of the membrane) was exposed to He at 20 mL·min^{-1}, and connected to a gas chromatography (Agilent 6890) for quantifying the permeated H_2. **Figure 5.2** shows the assembly of H_2-permeable membrane reactor for the permeation tests. In addition to being a diluent, the Ar in the feed gas was used as a tracer. A leak will be indicated by an increase in Ar signal in the gas chromatography. A CO_2 leakage test was also performed on the H_2 permeable tubular membrane reactor. The procedure is similar to the H_2 permeation test, but with CO2/He mixtures in the feed gas.

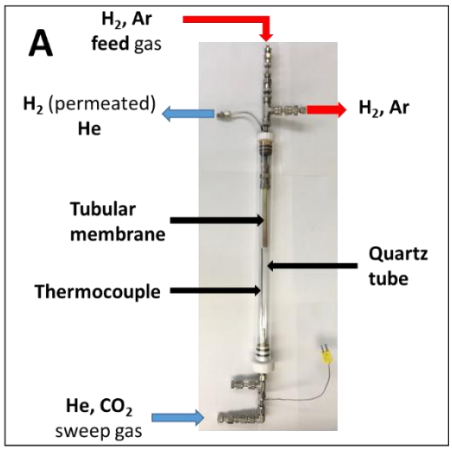

Figure 5.2. The assembly of H_2-permeable membrane reactor for the permeation tests

5.2.2. DNMC reaction in fixed-bed and H_2 permeable $SrCe_{0.7}Zr_{0.2}Eu_{0.1}O_{3-\delta}$ membrane reactors. The DNMC reaction was run at atmospheric pressure in either a fixed-bed (without H_2 permeation, **Figure 5.3(B)** or tubular membrane reactor (with H_2 permeation, **Figure 5.3(A)**). In a typical experiment, 0.375 g of catalyst was loaded at the center of the reactor and then heated to the desired temperature in pure Ar at the rate of 20 mL·min^{-1}. After the reaction gas mixture (90%CH_4-10%Ar) was introduced, the reaction was run at the temperature range of 1223-1323 K and at a feed gas space

velocity of 3200 $mL \cdot g^{-1} \cdot h^{-1}$. During the reaction in the tubular membrane reactor, the sweep gas, mixture of CO_2 and He, was introduced. The reactant (CH_4 mixed with a 10 mol% Ar tracer) was introduced through the inner tube in the top center section of the reactor and the products exited through the top left side of the reactor. The outer annular region of the membrane reactor was exposed to CO_2/He sweep gas to carry the permeated H_2 away from the reactor system or to feed H_2 into the reactor system. The effluent gases from the feed side and the sweep side were analyzed on-line by Agilent 6890 Gas Chromatograph to determine the CH_4 conversion and product selectivity.

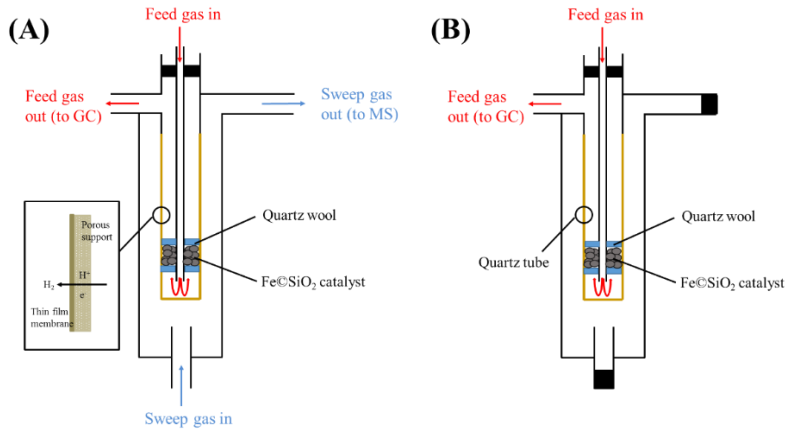

Figure 5.3. Detailed reactor set-up for (A) H_2 permeable $SrCe_{0.7}Zr_{0.2}Eu_{0.1}O_{3-\delta}$ membrane reactor and (B) fixed-bed reactor.

5.3 Results and Discussions

5.3.1 Performance of the $SrCe_{0.7}Zr_{0.2}Eu_{0.1}O_{3-\delta}$ tubular membrane reactor coupled with Fe/SiO_2 catalyst. Figure 5.4 shows the effects of different sweep gas on the DNMC reaction, which is on the inside of the hydrogen-permeable membrane reactor. As a reference, a control experiment was also performed with a fixed-bed reactor to

demonstrate the DNMC performance without H_2 removal. **Figure 5.4(A)** shows an increase in CH_4 conversion when comparing the fixed-bed reactor (without H_2 removal) to the membrane rector with both He and O_2 as sweep gases. Without a sweep gas, CH_4 conversion in DNMC in the membrane reactor was slightly higher compared to the non-catalytic quartz tube. This is due to the activity of the membrane reactor itself. By using the sweep gas to simultaneously remove the permeated H_2 from the membrane reactor, the equilibrium conversion is shifted to the product side which increase the CH_4 conversion in accordance with Le Chatelier's principle. When switching the reactor from fixed-bed reactor to membrane reactors with both He and O_2 sweep gases, the products yields of all products also increased especially for aromatics. **Figure 5.4(B)** shows the selectivity comparison among the fixed-bed reactor and membrane reactors with different sweep gases. When comparing to the fixed-bed reactor, the membrane reactor without sweep gas showed a slight decrease in C_2 selectivity, and a slight increase in benzene, while both had small selectivity to coke formation. Adding a He sweep to simultaneously remove H_2 shifted the equilibrium to the product side, which resulted in greater CH_4 conversion and an increase in coke selectivity.

When O_2 was used as sweep gas, almost no carbon deposition was observed. However, CO was observed as a byproduct in the effluent of the DNMC reaction. This is due to the fact that $SrCe_{0.7}Zr_{0.}2Eu_{0.1}O_{3-\delta}$ is a mixed ionic-electronic conductor, which can acted as an oxygen-permeable membrane at certain conditions.[72] Therefore, carbon deposition can be oxidized to form CO from the back diffusion of O_2 from the sweep side to the feed side. Similar idea was reported by Morejudo et al.[116], who

used electrical circuit to control co-permeation fluxes of both H_2 and O_2 to alleviate carbon deposition. The use of oxygen-permeable membrane to supply O_2 to alleviate carbon deposition for DNMC reaction was also reported by Cao et al.[141] In addition, a small O_2 leak from the permeated side of the membrane also contributed to the appearance of CO in the DNMC reaction side of the membrane reactor.

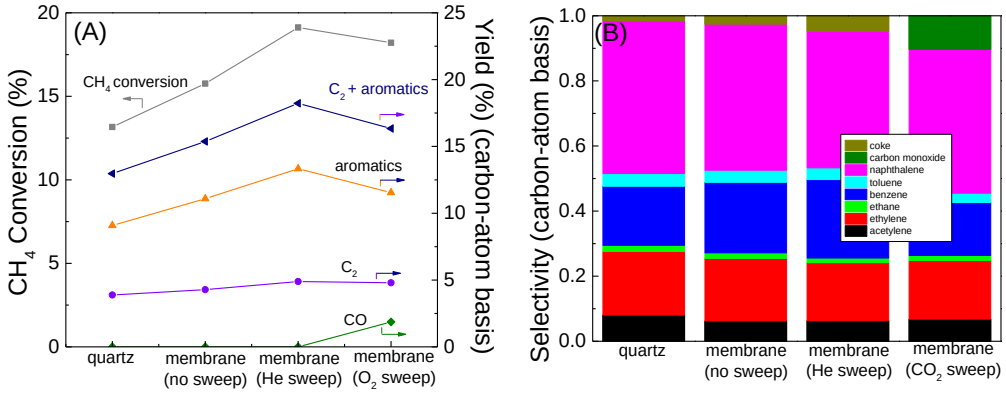

Figure 5.4. (A) CH_4 conversion and product yield over Fe/SiO_2 catalyst in fixed-bed reactor and membrane reactor with different sweep gases. (B) Product selectivity over Fe/SiO_2 catalyst in fixed-bed reactor and membrane reactor with different sweep gases. (Reaction condition: 1303 K, space velocity in DNMC reaction tests: 3200 $mL \cdot g^{-1} \cdot h^{-1}$, sweep gas flow rate: 20 $mL \cdot min^{-1}$)

Figure 5.5 shows the CH_4 conversion and product yields for the DNMC reaction with different sweep side O_2 concentrations and sweep side flow rates. From **Figure 5.5(A)**, at 1303 K, by maintaining the O_2 concentration at 20% and the increasing the total flow rates from 10 – 80 $mL \cdot min^{-1}$, the overall CH_4 conversion slightly decreased. The change in conversions can be explained by two competing phenomena. First, the increase in the O_2 flow rates increases the amount of O2 exposure to the membrane per unit time, which can increase the surface exchange rate of oxygen with the membrane material. This increase in the O_2 surface exchange rate has a negative effect (lower) on the ambipolar (electronic) conductivity of the membrane,

which leads to a decrease in the flux of the permeated H_2 and therefore lowered CH_4 conversion. However, the permeated H_2 is combusted with the O_2 sweep gas at a higher rate, which leads to an increase in H_2 partial pressure gradient and an increase in CH_4 conversion. Overall, as shown by CH_4 conversion, a decrease in the ambipolar conductivity of the membrane due to the higher oxygen partial pressure from O_2 dominates the overall performance, even though it is somewhat offset by the increase in H_2 partial pressure gradient. **Figure 5.5(A)** also demonstrates the effects of the increase on O_2 concentrations (5, 10, 20, 30 and 40 mol%, balanced by He), while keeping the total flow rates at 20 $mL \cdot min^{-1}$. The overall CH_4 conversion displayed similar trend compared to the case of increasing total sweep gases flow rates. The increase in the O_2 concentration increases the overall O_2 partial pressure on the sweep side. This increase in the O_2 partial pressure leads to lower ambipolar conductivity of the membrane, which leads to a decrease in the flux of the permeated H_2, and therefore lowered CH_4 conversion. However, the increase in O_2 concentration also leads to higher combustion rate of permeated H_2, which increases the partial pressure of H_2 across the membrane. Overall, the decrease in ambipolar conductivity slightly dominated over the increase in H_2 partial pressure for the higher rate of H_2 combustion. As shown in **Figure 5.5(B)**, the selectivity for all the different O_2 concentrations and flow rates showed similar product selectivity. CO was presented in all concentration of O_2 and flow rates due both to greater co-flux of oxygen and any transmembrane CO_2 leakage. This also had benefit of reduced coke formation.

Figure 5.5(C) compares the heat requirement for DMNC reaction and heat released from the combustion of the permeated H_2 at different sweep side O_2

concentrations and sweep side flow rates. The results showed that the heat released from the combustion of permeated H_2 was not enough to supply heat for the DNMC reaction. This is due to the insufficient H_2 flux across the membrane, which is directly related to the ambipolar conductivity of the $SrCe_{0.7}Zr_{0.2}Eu_{0.1}O_{3-\delta}$ membrane. The low porosity of our current membrane support (limitation of our current fabrication method) has also led to some mass transport limitation, which contributed to the low H_2 flux. In addition, the carbon deposition during the induction period also contributed to the decrease in the performance of the $SrCe_{0.7}Zr_{0.2}Eu_{0.1}O_{3-\delta}$ membrane.

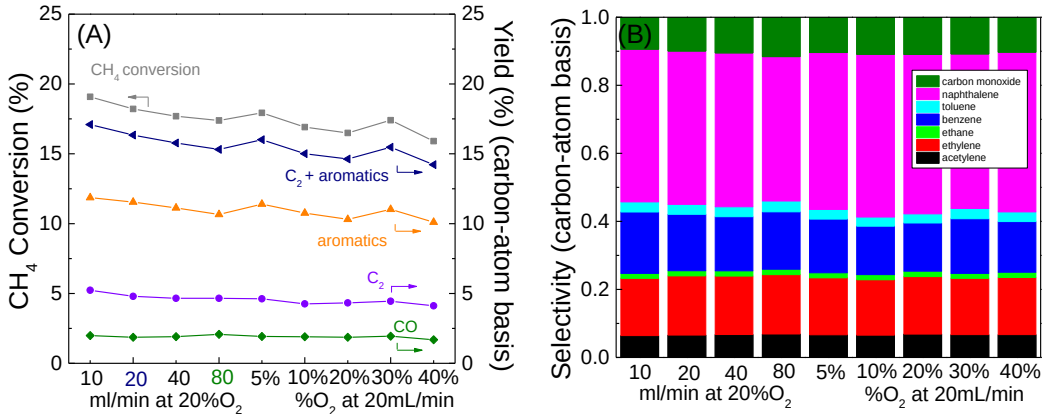

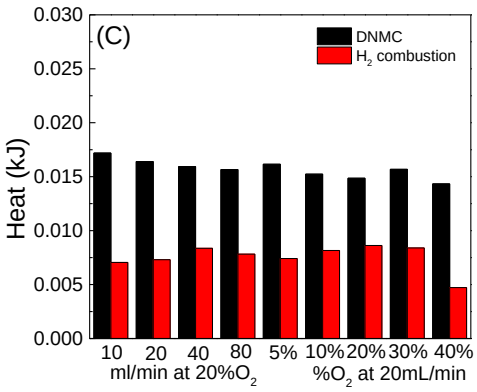

Figure 5.5. (A) CH_4 conversion and product yield in DNMC reaction side of the membrane reactor as a function of O_2 concentrations and flow rates in the sweep side. (B) Product selectivity in DNMC reaction side of the membrane reactor as a function of O_2 concentrations and flow rates in the sweep side. (C) Heat requirement for DMNC reaction and heat released from the combustion of the permeated H_2 as a function of O_2 concentrations and flow rates in the sweep side. (Reaction condition: 1303 K, space velocity in DNMC reaction tests: 3200 $mL \cdot g^{-1} \cdot h^{-1}$, sweep gas flow rate: 20 $mL \cdot min^{-1}$, He used as balance gas in the sweep side)

In order to match the heat released from the H_2 combustion to the heat requirement of the DNMC reaction at 1303 K, the H_2 permeation needs to be improved significantly, which requires the improvement in the membrane formulation. Another potential way to demonstrate the possibility of matching the heat requirements is to lower the operating temperature in order to lower the heat requirement for the DMNC reaction. In addition, at lower operating temperature, the percentage of the produced H_2 permeated is higher at lower temperature due to less carbon deposition on the surface of the membrane during the induction period, which lowers the H_2 permeation. This agrees with our previous report.[38] **Figure 5.6** shows the CH_4 conversion and product yields for the DNMC reaction with different sweep side O_2 concentrations and sweep side flow rates at 1273 K. The CH_4 conversion and product yields at 1273 K were significantly lowered compared to the membrane performance at 1303 K.

However, the general trends of the CH_4 conversion, product yields, and product selectivity between the two temperatures were the same. **Figure 5.6(C)** compares the heat requirement for DMNC reaction and heat released from the combustion of the permeated H_2 at different sweep side O_2 concentrations and sweep side flow rates at 1273 K. At 1273 K, the heat requirement of the DNMC reaction was balanced by the heat released from the H_2 combustion at all conditions, which meant that autothermal operation was achieved.

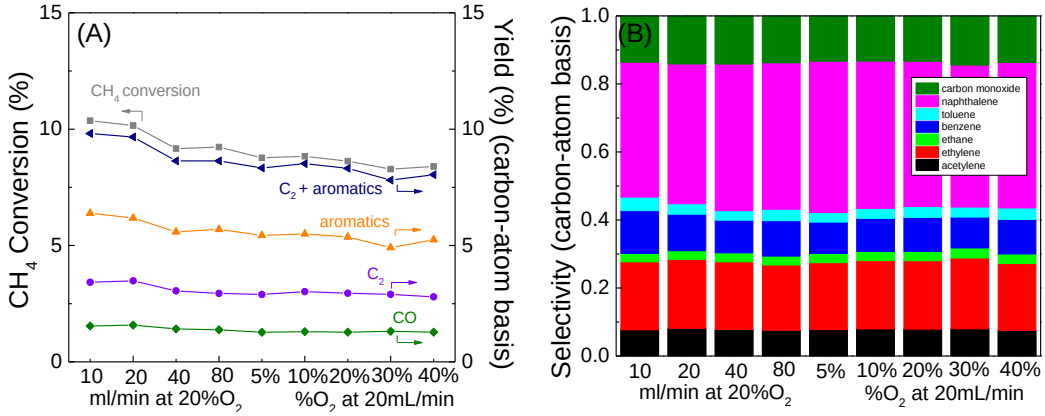

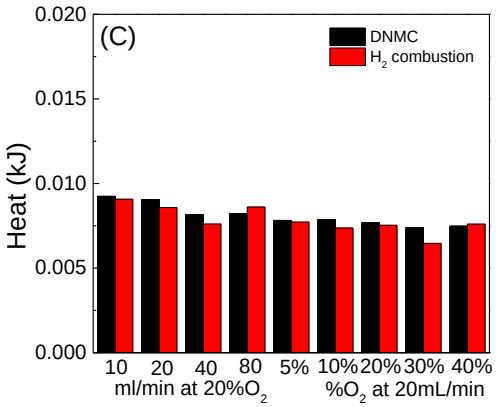

Figure 5.6. (A) CH_4 conversion and product yield in DNMC reaction side of the membrane reactor as a function of O_2 concentrations and flow rates in the sweep side. (B) Product selectivity in DNMC reaction side of the membrane reactor as a function of O_2 concentrations and flow rates in the sweep side. (C) Heat requirement for DMNC reaction and heat released from the combustion of the permeated H_2 as a function of O_2 concentrations and flow rates in the sweep side. (Reaction condition: 1273 K, space velocity in DNMC reaction tests: 3200 $mL \cdot g^{-1} \cdot h^{-1}$, sweep gas flow rate: 20 $mL \cdot min^{-1}$, He used as balance gas in the sweep side)

Figure 5.7 shows the CH_4 conversion and product yields for the DNMC reaction with different sweep side O_2 concentrations and sweep side flow rates at 1253 K. As the temperature decreased from1303K to 1273K, and then to 1253K, the CH_4 conversion decreased from ~18% to ~9% to ~6%. Overall, there was a shift in the selectivity of the hydrocarbon products from aromatics to C_2 when going from 1303K to 1253K. **Figure 5.7(C)** compares the heat requirement for DMNC reaction and heat released from the combustion of the permeated H_2 at different sweep side O_2 concentrations and sweep side flow rates at 1253 K. At 1253K, the overall CH_4 conversion has decreased when compared to 1273K, and therefore lessen the heat requirement from the DNMC side. The results showed that the heat released from the combustion of permeated H_2 was more than the required heat input for the DNMC reaction. This results follow the trend from 1303K to 1273K, and then to 1253K.

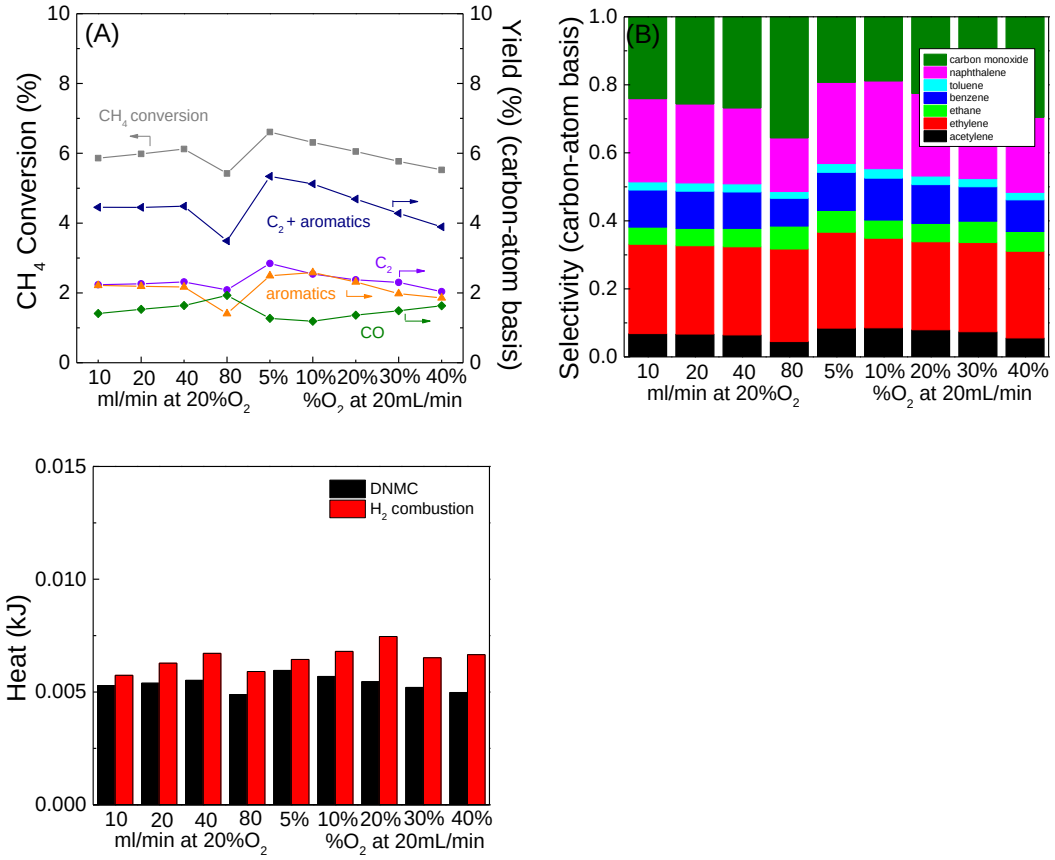

Figure 5.7. (A) CH_4 conversion and product yield in DNMC reaction side of the membrane reactor as a function of O_2 concentrations and flow rates in the sweep side. (B) Product selectivity in DNMC reaction side of the membrane reactor as a function of O_2 concentrations and flow rates in the sweep side. (C) Heat requirement for DMNC reaction and heat released from the combustion of the permeated H_2 as a function of O_2 concentrations and flow rates in the sweep side. (Reaction condition: 1253 K, space velocity in DNMC reaction tests: 3200 $mL \cdot g^{-1} \cdot h^{-1}$, sweep gas flow rate: 20 $mL \cdot min^{-1}$, He used as balance gas in the sweep side)

5.3.2 Long-term stability test of the hydrogen-permeable tubular membrane reactor

The stability of the $SrCe_{0.7}Zr_{0.2}Eu_{0.1}O_{3-\delta}$ tubular ceramic membrane reactor in dual DNMC and H_2 combustion reactions was tested by running both reactions at 1303 K for 50 hours while flowing 20 mol% O_2 (balanced by He) in the sweep gas. **Figure 5.8(A)** shows the DNMC catalytic performance with the CH4 conversion stable at ~18%. There was an induction period of ~8 h where the rate of carbon formation was

high. After the induction period, the rate of carbon formation decreased with TOS dropping to nearly zero over the long-term reaction run. The induction period is contributed by both the Fe/SiO_2 and the $SrCe_{0.7}Zr_{0.2}Eu_{0.1}O_{3-\delta}$ tubular membrane reactor. After the induction period (TOS of ~8 h), the membrane reactor reached a stable performance, where the CH4 conversion remained at ~18% throughout the whole experimental run. The product yields of C_2, aromatics, C_{2+}, and CO were stable at approximately 4.6%, 11.9%, 16.5%, and 0.7%, respectively. The CO formation on the membrane side is consistent with oxygen transport through the membrane, which help limits the carbon formation under stable conditions. Since $SrCe_{0.7}Zr_{0.2}Eu_{0.1}O_{3-\delta}$ is a mixed conductors, it has a small oxygen-ion conductivity, which is consistent with the formation of CO on the CH_4 side of the membrane (**Figure 5.8(A) and 5.8(B)**). Even though the formation of CO lowers the overall hydrocarbon yield, O_2 sweep gas limits coke formation under steady-state conditions. After the reaction reached this equilibria the coke formation rate was minimal demonstrating a decreasing trend in coke formation with TOS of the reaction.

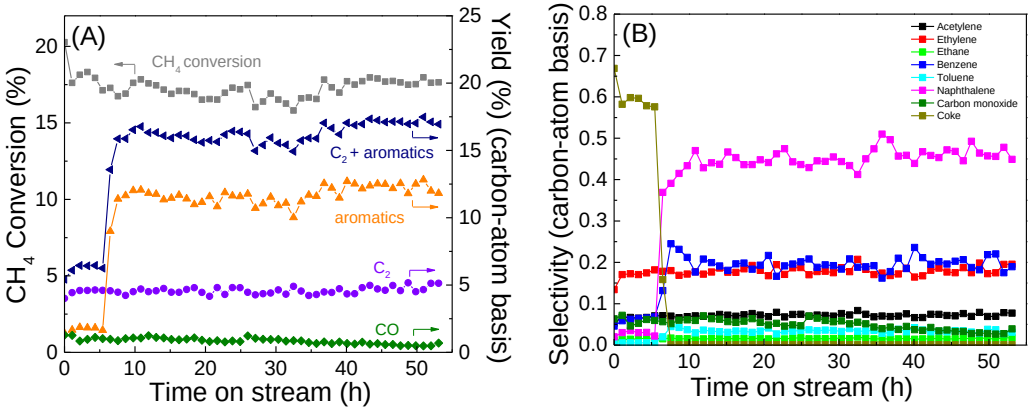

Figure 5.8. Long-term stability test of the hydrogen-permeable tubular membrane reactor for DNMC reaction coupled with H_2 oxidation on opposite sides. (Reaction

condition: 1303 K, space velocity in DNMC reaction tests: 3200 $mL \cdot g^{-1} \cdot h^{-1}$, sweep gas flow rate: 20 $mL \cdot min^{-1}$, O_2 concentration in the sweep side: 20%, balanced by He)

5.4 Conclusion of Chapter 5

In summary, a tubular membrane reactor made from a ionic-electronic conducting $SrCe_{0.7}Zr_{0.2}Eu_{0.1}O_{3-\delta}$ thin-film deposited on a porous $SrCe_{0.8}Zr_{0.2}O_{3-\delta}$ support combined with a Fe/SiO_2 DNMC catalyst was explored for the use as a heat-exchange membrane reactor for DNMC reaction coupled with the oxidation of the membrane-permeated H_2. On the inside of the membrane reactor tube, CH_4 is upgraded to C_{2+} hydrocarbons and H_2 via the DMNC reaction over the Fe/SiO_2 catalyst. On the other side of the membrane, the permeated H_2 reacted with O_2 in the sweep gas via the exothermic combustion reaction to form water and released heat. The heat released can be used to provide energy for the endothermic DMNC reaction. At 1273 K, the heat balance between the endothermic DNMC reaction and the exothermic H_2 combustion reaction was achieved (autothermal). The results have demonstrated the feasibility of the heat-exchange membrane reactor for the enhancement of the endothermic DMNC reaction via in situ H_2 removal with heat supplied by the exothermic oxidation of the permeated H_2. Autothermal operation at higher operating temperatures can be achieved by improving the H_2 flux though the membrane reactor.

Chapter 6: Enhancement of the Production of Liquid Hydrocarbons (Aromatics) for the Direct Non-Oxidative Methane Conversion via a Dual Reactor/H_2-Membrane Separator

6.1 Introduction

Due to the advancement of the oil and gas extraction technologies, the production of natural gas has increased significantly in the past few decades.[2, 3] These technologies have led to natural gas supplies from then unattainable extraction sites like impermeable rocks of shale.[3] The major obstacle which prevents the utilization of these sources is the transportation cost from the remote areas to the

utilization sites. One way to circumvent this problem is to have modular unit at the extraction sites, which convert natural gas into liquid fuels, which is easier and less costly to transport. In addition, natural gas conversion units will also lead to less flaring, which reduces natural gas waste and release of CO_2 to the atmosphere. Methane (CH_4) is an abundant fossil resource and the main constituent of natural gas and oil-associated gases. Traditionally, CH_4 is converted to value-added hydrocarbons via the steam reforming of CH_4 reaction to produce syngas ($CO + H_2$), followed by Fischer-Trøpsch process, which lead to low carbon and energy efficiencies.[6, 12, 100-102] Direct CH_4 conversion routes such as oxidative coupling of methane (OCM)[103-105], and direct non-oxidative methane conversion (DNMC)[6, 25, 35, 37, 38, 106, 138] have also been explored. Compared with other approaches, DNMC is more selective given its unique capability in forming C_{2+} hydrocarbons (C_2 and aromatics) and H_2 while circumventing the intermediate energy intensive steps.[6, 12] DNMC is a viable approach because it can convert CH_4 to liquid hydrocarbons in a single step. In addition, DNMC only requires CH_4 as the only reactant, which is beneficial for the modular unit at remote extraction sites.[154] The molybdenum/zeolite (Mo/ZSM-5) has been the most effective and extensively studied catalyst for DNMC.[6, 27, 50, 52, 106, 139, 155] DNMC, however, is typically hindered by thermodynamic limitations and high rate of catalyst deactivation from coke formation.[6, 27, 50, 52, 106, 139, 155]

Considerable efforts have been placed on the development of novel methods to alleviate the thermodynamic limitations and the catalyst deactivation barriers. To alleviate the deactivation of the Mo/ZSM-5 catalyst, different methods have been experimented including varying the type of zeolite[6, 155-159] and silica-to-alumina

ratio[156], and periodic regeneration using H_2 or oxidants.[157-159] H_2 or O_2 permeable membranes, such as metal alloys[59, 60, 89, 92] and ionic/electronic conducting ceramics,[30, 31, 35, 37, 38, 113] capable of H_2 withdrawal from or O_2 addition into the reactor were exploited to alleviate the barrier for thermodynamic limitations. Based on theoretical calculation, a substantial enhancement is predicted when a H_2-permeable membrane is coupled with a DNMC catalyst. However, parallel experimental studies were not favorable due to the low H_2 permeation flux of the membrane, and due to accelerated catalyst deactivation under H_2 removal conditions.[37, 113]

In this chapter, we report a reactor/separator recycle system for the effective strategy to circumvent the thermodynamic limitations of DNMC, produce high purity H_2, and maximize aromatics production. **(Figure 6.1)** In the process, CH_4 is first passed through the Fe/SiO_2 catalyst for the DNMC reaction at 1303 K, producing equilibrated mixtures of CH_4, H_2, C_2 (acetylene, ethylene, ethane), and aromatics (benzene, toluene, naphthalene) (step 1). Then, the aromatics are removed from the effluent gases via s simple condenser (step 2). The remaining gases (CH_4, H_2, C_2) are passed through the H_2-permeable $SrCe_{0.7}Zr_{0.2}Eu_{0.1}O_{3-\delta}$ tubular membrane for H_2 separation (step 3). The effluent from step 3 is used as the feed to the DMNC reactor of the subsequent cycle. By increasing the number of cycles, the CH_4 conversion beyond its equilibrium conversion could be achieved. Based on our previous research[38], the H_2 permeation of the membrane during the DNMC is lower than those during the permeation tests. This phenomenon can be explained by the coking of the membrane surface during the DNMC induction period. One of the ways to avoid coking is to have a separate DNMC

reactor and H_2 separator unit. The H_2 permeation through the $SrCe_{0.7}Zr_{0.2}Eu_{0.1}O_{3-\delta}$ membrane in the membrane reactor was measured as a function of temperature and H_2 partial pressure.

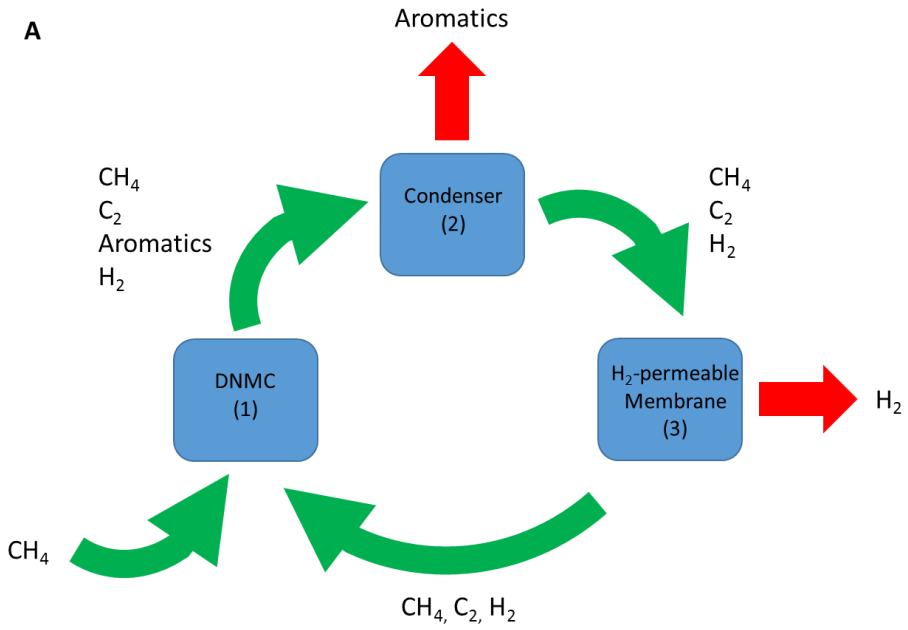

Figure 6.1. Proposed combined DNMC reactor and H_2-permeable membrane for enhancement of aromatics production

6.2 Experiments

6.2.1. H_2 permeation and Leakage tests for H_2 permeable tubular membrane reactor. Prior to the usage of the H_2 permeable membrane reactor for DNMC over Fe/SiO_2 catalyst, the membrane reactor underwent leakage and H_2 permeation tests. The tubular membrane reactor was used for these experiments. The feed side (inside of the membrane) was exposed to H_2 diluted to the tested concentration using Ar tracer. The total flow rate of the feed gas (mixture of H_2 and Ar) was set at 20 $mL \cdot min^{-1}$. The

sweep side (outside of the membrane) was exposed to He at 20 mL·min^{-1}, and connected to a gas chromatography (Agilent 6890) for quantifying the permeated H_2. **Figure 6.2** shows the assembly of H_2-permeable membrane reactor for the permeation tests. In addition to being a diluent, the Ar in the feed gas was used as a tracer. A leak will be indicated by an increase in Ar signal in the gas chromatography. A CO_2 leakage test was also performed on the H_2 permeable tubular membrane reactor. The procedure is similar to the H_2 permeation test, but with CO2/He mixtures in the feed gas.

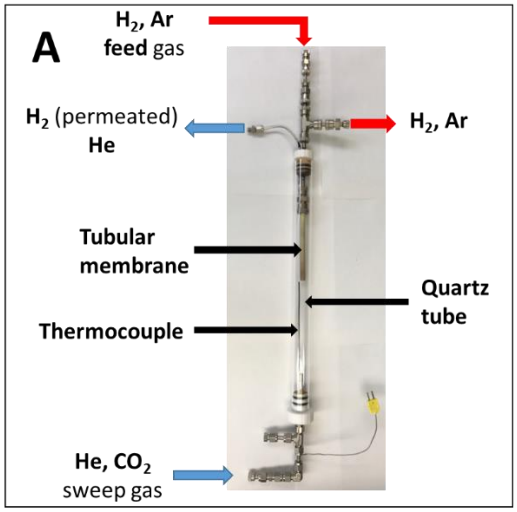

Figure 6.2. The assembly of H_2-permeable membrane reactor for the permeation tests

6.2.2. DNMC reaction in fixed-bed reactor. The DNMC reaction was run at atmospheric pressure in a fixed-bed (without H_2 permeation, **Figure 6.3**. In a typical experiment, 0.375 g of catalyst was loaded at the center of the reactor and then heated to the desired temperature in pure Ar at the rate of 20 mL·min^{-1}. After the reaction gas mixture (90%CH_4-10%Ar) was introduced, the reaction was run at the temperature range of 1223-1323 K and at a feed gas space velocity of 3200 mL·g^{-1}·h^{-1}. The effluent

gases from the feed side was analyzed on-line by Agilent 6890 Gas Chromatograph to determine the CH_4 conversion and product selectivity.

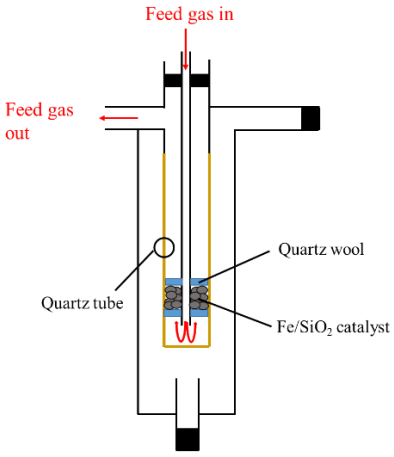

Figure 6.3. Detailed reactor set-up for the fixed-bed reactor.

6.3 Results and Discussions

6.3.1 H_2 permeation through the $SrCe_{0.7}Zr_{0.2}Eu_{0.1}O_{3-\delta}$ tubular membrane reactor.

To demonstrate the performance of the proposed reactor/separator recycle system, the DNMC reactor and the H_2-permeable membrane were investigated separately with simulated feeds. Pure CH_4 feed at 1303 K at 3200 $mL \cdot g^{-1} \cdot h^{-1}$ gave the CH_4 conversion of 14%, with C_2 product yield of 5.4%, and aromatics yield of 8.5%. The Fe/SiO_2 showed a stable CH_4 conversion and product selectivity. Mixtures of CH_4, C_2H_4, and H_2 with varying molar ratios were used as feeds to simulate the feed in the subsequent cycles. Assuming that all aromatics are removed via a condenser and all of the C_2 species in the effluent gases were assumed to be C_2H_4 for the subsequent stage, the composition of the simulated feed can determined. For example, $CH_4/C_2H_4/H_2$ ratio

of 1/0.03/0.20 is used to simulate the feed for the second cycle, based on the experimental CH_4 conversion and product selectivity in the first cycle.

For the permeation performance of the $SrCe_{0.7}Zr_{0.2}Eu_{0.1}O_{3-\delta}$ membrane, a series of permeation fluxes data at different temperatures and H_2 partial pressures were collected. **Figure 6.4(A)** shows that the permeated H_2 flux was increased with the H_2 concentration on the feed side. In addition, the H_2 permeation flux increased as the temperature increased due to the increase in ambipolar ionic/electronic conductivity of the $SrCe_{0.7}Zr_{0.2}Eu_{0.1}O_{3-\delta}$ membrane. These two observations are consistent with the Wagner equation. After each cycle was run in the DNMC reactor, the $\%H_2$ in the effluent gas was calculated, the amount of H_2 permeation through the membrane can be determined from the permeation database. A control experiment was performed in order to select the appropriate temperature for the membrane reactor. A small amount of CH_4 was included in the permeation gas to evaluate the effects of hydrocarbons on the H_2 permeation flux. As shown in **Figure 6.4(B)**, it was found that at 1173 K, there was a significant reduction in H_2 flux due to coke formation on the surface of the membrane. Therefore, the temperature of 1073 K was selected for the membrane reactor. After the determination of the H_2 permeation flux, that amount was subtracted from the effluent gas. Then the simulated feed content of the next cycle can be determined.

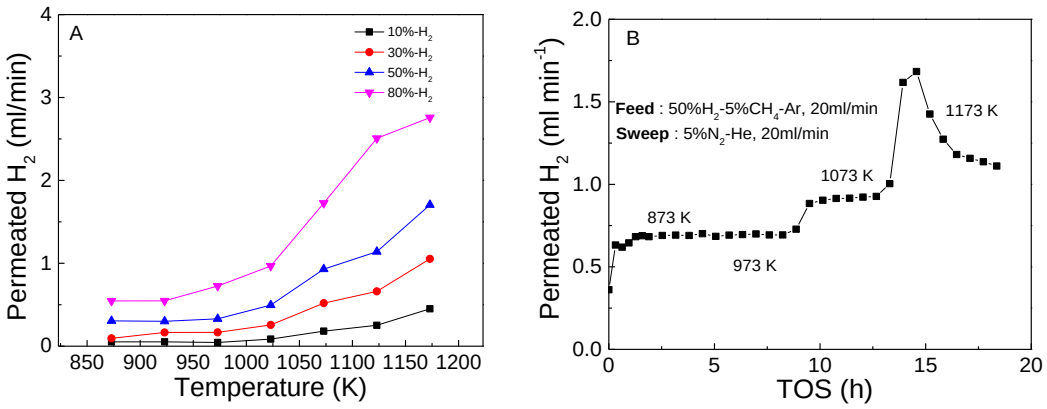

Figure 6.4. (A) H_2 permeation flux through $SrCe_{0.8}Zr_{0.2}O_{3-\delta}$ membrane as a function of temperature and H_2 partial pressure. (B) Effect of hydrocarbons on the H_2 permeation flux of the $SrCe_{0.7}Zr_{0.2}Eu_{0.1}O_{3-\delta}$ membrane reactor at different temperatures.

6.3.2 Performance of the Fe/SiO_2 at different stages of the dual DNMC/H_2-permeable membrane reactor system.

Figure 6.5 demonstrates the CH4 conversion and product selectivity at different cycle number as a function of H_2 removal (permeation). From **Figure 6.5(A)**, which is the performance of the $SrCe_{0.8}Zr_{0.2}O_{3-\delta}$ membrane (~10% permeation), CH_4 conversion decreased as the cycle number increased. There are two different phenomena governing the effects of the CH_4 conversion trend. From the second cycle onward, C_2 and H_2 were included in the feed gas as a result of the DNMC reaction from the previous cycle, which will affect the equilibrium CH_4 conversion. According to the Le Châtelier's principle, the inclusion of H_2 will shift the equilibrium to the reactant side, which will lower the CH_4 conversion. From the feed composition at each cycle (**Figure 6.6**), an increase in $\%H_2$ of the feed gas was observed, which agreed with the decreasing trend of the CH_4 conversion. In addition, from **Figure 6.6(A)**, the total flow rates of the subsequent cycles were slightly higher than the 1st cycle, which means

higher space velocities for the DNMC reaction. Higher space velocities led to lower CH_4 conversion. As for the selectivity, the product selectivity shifted toward lighter products as the cycle number increased. This is because of the addition of H_2 in the feed of the subsequent cycles, which shifts the overall equilibrium of the DNMC reaction. In addition, the slight increase in the space velocities also has a small effect in shifting the products to lighter hydrocarbons.

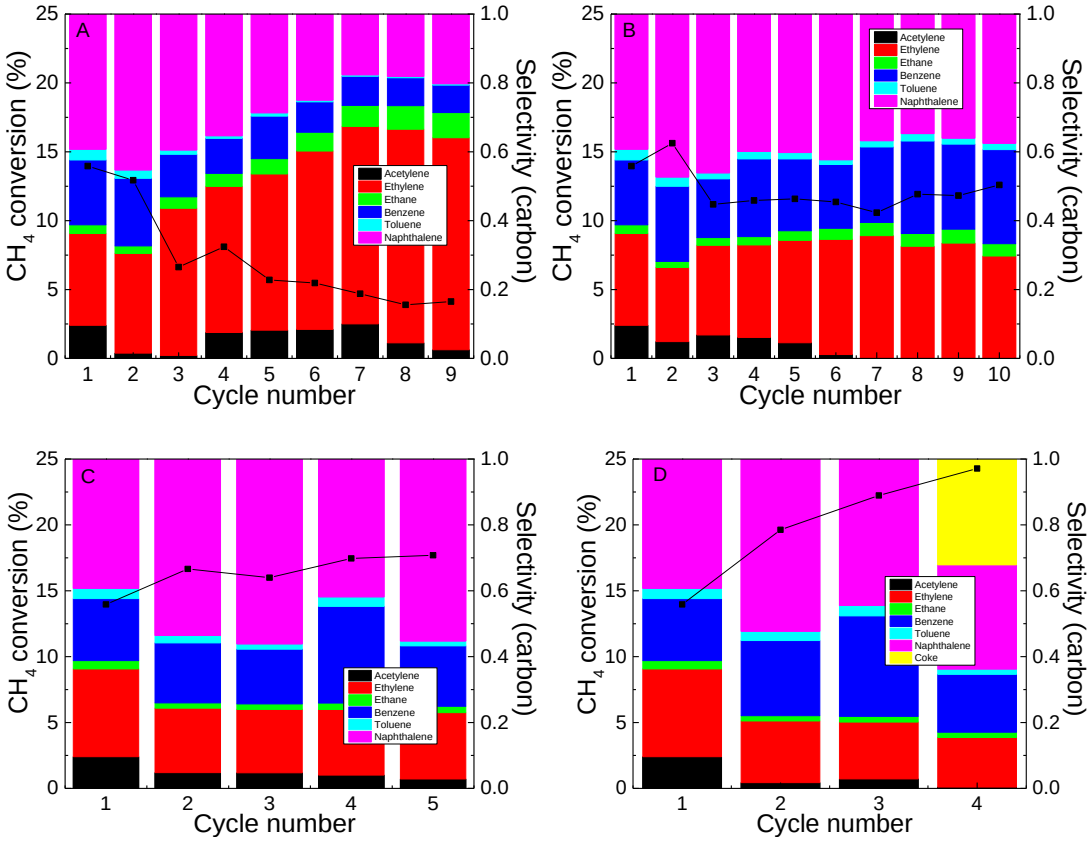

Figure 6.5. CH_4 conversion and product selectivity at different cycle number as a function of H_2 removal, (A) ~10% H_2 removal ($SrCe_{0.7}Zr_{0.2}Eu_{0.1}O_{3-\delta}$ membrane), (B) 40% H_2 removal, (C) 70% H_2 removal, and (D) 100% H_2 removal.

From the case of using the $SrCe_{0.7}Zr_{0.2}Eu_{0.1}O_{3-\delta}$ membrane, it can be postulated that the aromatics liquid production from DMNC reaction can be enhanced further if the H_2 permeation is improved. The following data covered the cases with higher H_2

permeation. **Figure 6.5(B)** shows the performance of the reactor-gas separator system with 40% H_2 removal. At 40% H_2 removal, the H_2 content leftover in the feed of the subsequent cycles (**Figure 6.6(B)**) were less compared to the case of the removal using membrane reactor. However, this should still lead to lower CH_4 conversion, and product selectivity shift to lighter hydrocarbons. However, 40% removal of H_2 lowered the overall flow rates significantly, which led to lower space velocities for the DNMC reaction. Lower space velocities of DNMC should lead to higher CH_4 conversion and shift the product selectivity toward larger hydrocarbons. These two effects seemed to balance each other out at 40% H_2 removal, which led to relatively stable CH_4 conversion and product selectivity.

At significant levels of H_2 removal of 70% and 100% (**Figure 6.5(C)** and **Figure 6.5(D)**), the effects of lowering DNMC reaction space velocities dominates over the inclusion of H_2 in the subsequent cycles. Therefore, the CH_4 conversion increased as the cycle number increased at 70% and 100% H2 removal. In addition, the product selectivity shifted toward larger hydrocarbons (liquid). Too high of a reduction in the DMNC space velocities can lead to coke formation, which was demonstrated at the 4^{th} cycle of the reaction with 100% H_2 removal.

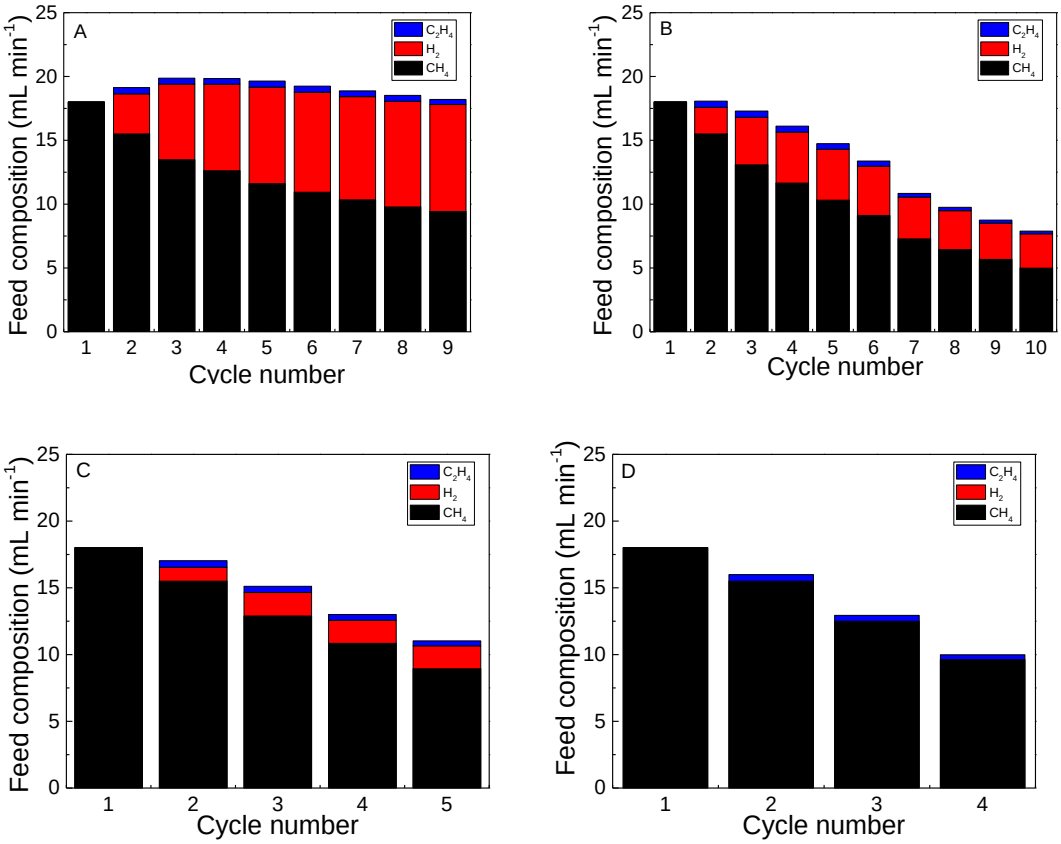

Figure 6.6. Feed composition at different cycle number as a function of H_2 removal, (A) ~10% H_2 removal ($SrCe_{0.7}Zr_{0.2}Eu_{0.1}O_{3-\delta}$ membrane), (B) 40% H_2 removal, (C) 70% H_2 removal, and (D) 100% H_2 removal.

After each cycle of the DNMC reactor/H_2-permeable membrane system was calculated, the overall performance of the system was analyzed in order to understand the overall CH_4 conversion and product selectivity and yields. **Figure 6.7** shows the overall CH_4 conversion and product selectivity at different level of H_2 removal. All of the H_2 removal levels showed similar trends. As the number of cycles increased, the overall CH_4 conversion increased. Based on our results, the overall CH_4 conversion can reached over 70%, and has the potential to reach even higher. The product selectivity also exhibited the same trend. As the number of cycles increased, the product selectivity

shifted toward larger aromatic hydrocarbons (liquid). The liquid portion of the products reached over 95%. As the amount of H_2 removal increased, it takes less number of cycles to reach the same level of CH_4 conversion, since the equilibrium conversion is enhanced by shifting toward the product side according to the Le Châtelier's principle.

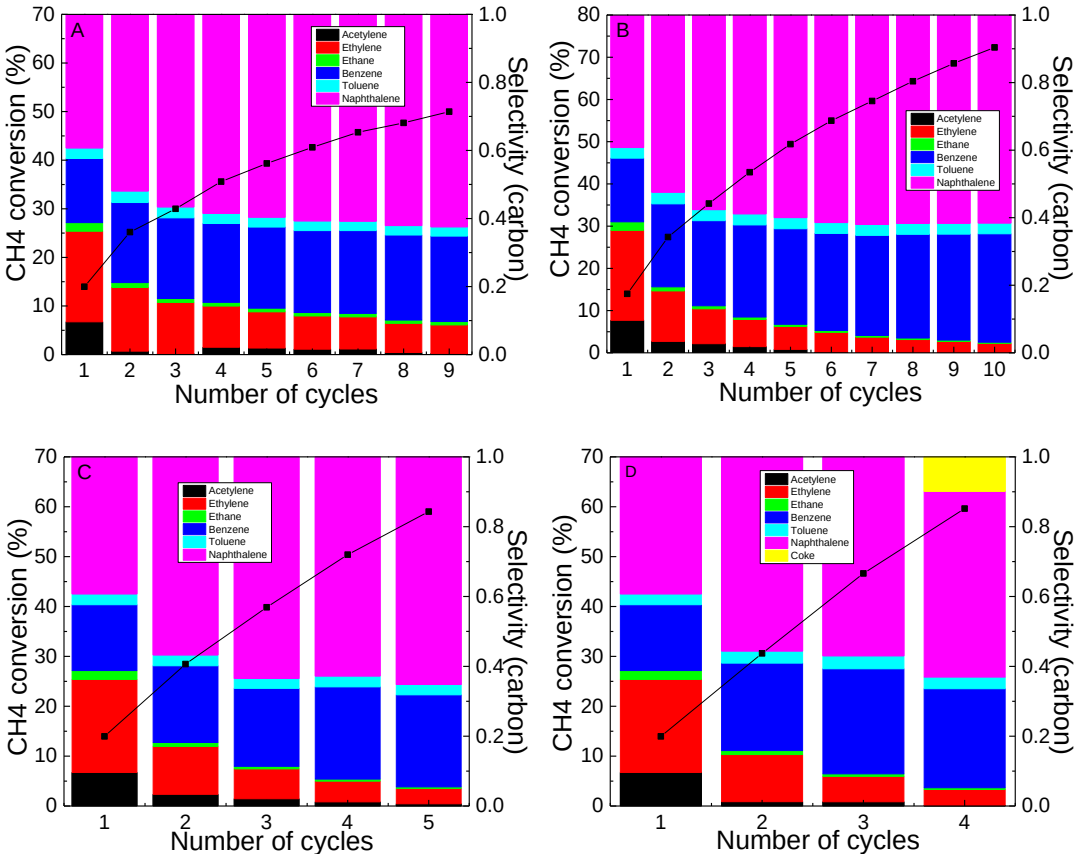

Figure 6.7. Overall CH_4 conversion and product selectivity as a function of H_2 removal, (A) ~10% H_2 removal ($SrCe_{0.7}Zr_{0.2}Eu_{0.1}O_{3-\delta}$ membrane), (B) 40% H_2 removal, (C) 70% H_2 removal, and (D) 100% H_2 removal.

Figure 6.8 demonstrates the overall aromatics yields at different H_2 removal rates. In terms of yield, the yield of aromatics is >40% after nine cycles at the current performance of the $SrCe_{0.7}Zr_{0.2}Eu_{0.1}O_{3-\delta}$ membrane. With higher removal rate of H_2, the system has the potential to reach even higher aromatics yield. For example, at 40%

H_2 removal rate, the aromatics yield can reach over 70%. Comparing the aromatics yields of the system with different H_2 removal rates clearly shows that the higher H_2 removal rates lead to higher aromatics yield. Again, this is because removal of H_2 shifts the equilibrium to the product side, which increase the equilibrium CH_4 conversion.

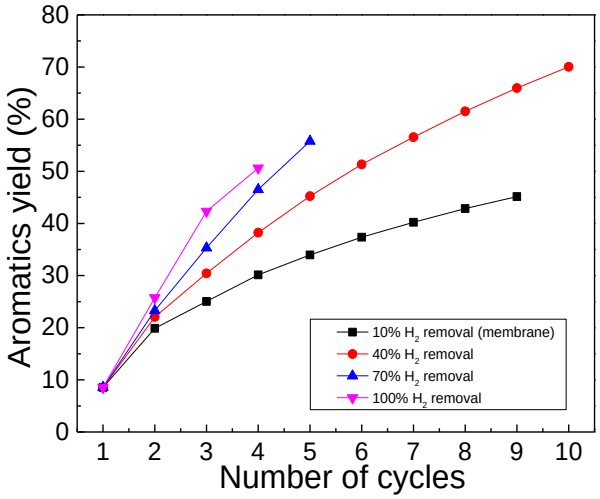

Figure 6.8. Overall aromatics yields at different H_2 removal rates

6.4 Conclusion of Chapter 6

In conclusion, a dual DNMC reactor and H_2-permeable membrane system was proposed in order to enhance the production of aromatics from CH_4, with pure H2 as a beneficial byproduct. The feasibility of the DNMC reactor and the $SrCe_{0.7}Zr_{0.2}Eu_{0.1}O_{3-\delta}$ membrane reactor were demonstrated individually. In certain conditions, the aromatics yield reached >50%, which is significantly higher than single-pass results.

Chapter 7: Conclusions (Major contributions) and future works

7.1 Conclusions

This research was motivated by the necessity to advance the methane upgrading technology in order to move away from the conventional indirect, energy intensive pathways. DNMC offers a more economical, more carbon and energy efficient pathway, even though several challenges need to be overcome. DNMC pathway's main limitations include low equilibrium CH_4 conversion due to thermodynamics, high endothermicity of the DNMC reaction, and high selectivity toward carbon deposition. In this study, we aim to circumvent the limitations of the DMNC reaction via the development of active DNMC catalysts, and the utilization of the H_2-permeable membrane reactor to simultaneously remove H_2 from the effluent in order to shift the equilibrium and increase overall CH_4 conversion. The principle objectives of this work include (i) fabrication of the H_2-permeable membrane reactor and synthesis of the Fe/SiO_2 catalyst, (ii) enhancement of the CH_4 conversion and product selectivity via the H_2-permeable membrane reactor over the Fe/SiO_2 catalyst, (iii) dual utilization of greenhouse gases to produce C_{2+} hydrocarbons and syngas in a H_2-permeable membrane reactor, (iv) autothermal direct non-oxidative methane conversion in a H_2-permeable membrane reactor, and (v) enhancement of the production of liquid hydrocarbons (aromatics) for DNMC via a dual reactor/H_2-Membrane separator.

Fe/SiO_2 has shown to be active for the DNMC reaction with minimal carbon deposition. By coupling the Fe/SiO_2 catalyst with the $SrCe_{0.7}Zr_{0.2}Eu_{0.1}O_{3-\delta}$ H_2-permeable membrane, we have shown the capability of the system to shift the

equilibrium of the DNMC reaction via the *in-situ* removal of the H_2 from the effluent gas.

In chapter 2, the fabrication of the $SrCe_{0.7}Zr_{0.2}Eu_{0.1}O_{3-\delta}$ H_2-permeable tubular membrane and the synthesis of the Fe/SiO_2 catalyst were demonstrated. The 25-μm thick $SrCe_{0.7}Zr_{0.2}Eu_{0.1}O_{3-\delta}$ membrane layer coated on the $SrCe_{0.8}Zr_{0.2}O_{3-\delta}$ porous support was successfully fabricated via tape casting and colloidal coating methods for the H_2 permeation from the effluent of the DNMC reaction. SEM of the membrane surface and cross-section showed dense and pinhole-free membrane. The Fe/SiO_2 was synthesized by fusing Fe_2SiO_4 and SiO_2 at 1973 K for 6 hours in air. The Fe/SiO_2 was demonstrated to be active for the DNMC reaction.

In chapter 3, the integration of a mixed ionic–electronic H_2-permeable $SrCe_{0.7}Zr_{0.2}Eu_{0.1}O_{3-\delta}$ membrane and Fe/SiO_2 catalyst into a catalytic tubular membrane reactor was demonstrated for for DNMC reaction. The removal of H_2 from DNMC reaction led to a significant increase in CH_4 conversion. The product selectivity to C_2 and aromatics as well as catalyst durability were not influenced significantly by the H_2 removal, which is distinctly different from all the previous studies in literature. The capability of tuning products (by either removing or adding H_2) towards C_2 (ethylene and acetylene) or aromatic (benzene and naphthalene) products was also demonstrated with high single-pass yields. The integration of Fe/SiO_2 catalyst in the high temperature H_2-permeable $SrCe_{0.7}Zr_{0.2}Eu_{0.1}O_{3-\delta}$ tubular membrane reactor enables new routes for transformation of CH_4 into high value-added chemicals and fuels.

In chapter 4, the RWGS reaction capability was added to the membrane reaction by using CO_2 as a sweep gas to produce syngas. The single $SrCe_{0.7}Zr_{0.2}Eu_{0.1}O_{3-\delta}$

membrane reactor tube packed with Fe/SiO_2 catalyst achieved simultaneous utilization of two major global greenhouse gases, i.e., CH_4 and CO_2, to produce value-added hydrocarbons (C_2 + aromatics) and CO (or syngas), as well as the capability of tuning H_2/CO ratio in syngas by tailoring CO_2 concentration in the sweep side of the reactor. On one side of the membrane tube, CH_4 upgrading to C_{2+} hydrocarbons was realized via DNMC reaction over the Fe/SiO_2 catalyst, with co-production of H_2 gas. On the opposite side, the hydrogen permeate reacted with CO_2 sweep to form CO and H_2O via the RWGS reaction. The *in-situ* removal of H_2 from DNMC shifted the reaction to high CH_4 conversion and heavier product formation, while the removed H_2 functions as an *in-situ* feedstock for hydrogenation of CO_2.

In chapter 5, O_2 was used as the sweep gas in order to react with the permeated H_2 through the membrane reactor, which is an exothermic reaction. The released heat can be used to supply heat for the endothermic DNMC reaction. The temperature and the concentration of O_2 in the sweep gas were optimized in order to balance the heat requirement of the DNMC reaction with the heat release from the H_2 combustion.

In chapter 6, a dual DNMC reactor and H_2-permeable membrane system was proposed in order to enhance the production of aromatics from CH_4, with pure H_2 as a beneficial byproduct. The feasibility of the DNMC reactor and the $SrCe_{0.7}Zr_{0.2}Eu_{0.1}O_{3-\delta}$ membrane reactor were demonstrated individually. In certain conditions, the aromatics yield reached >50%, which is significantly higher than single-pass results.

7.2 Future Works

(1) Fabrication of the optimized $SrCe_{0.7}Zr_{0.2}Eu_{0.1}O_{3-\delta}$ tubular ceramic membrane reactor.

Based on our results, it was found that the support layer of the $SrCe_{0.7}Zr_{0.2}Eu_{0.1}O_{3-\delta}$ tubular ceramic membrane reactor has some gas transport limitation due to lack of porosity. It was difficult to fabricate leak-free membrane reactors with increased porosity with the current fabrication method. The fabrication parameters such as sintering temperature, coating slurry, and coating method need to be optimized for the higher porosity support tube. In addition, if the $SrCe_{0.7}Zr_{0.2}Eu_{0.1}O_{3-\delta}$ membrane was coated inside the tubular support, the contact between CH_4 and the porous support could be avoided, which would reduce to the carbon formation.

(2) Optimization of the H_2-permeable membrane to maximize the H_2-flux

Based on the Wagner equation, two parameters of the membrane material that have an effect on the permeation flux are the ambipolar conductivity and the membrane thickness. Our lab has previously investigated the effect of dopant concentration in $SrCe_{1-x}Eu_xO_{3-\delta}$ ($0.05 \leq x \leq 0.2$) on ambipolar conductivity. We have found that the maximum ambipolar conductivity increases with temperature and Eu dopant concentration. The current dopant level of Eu is at 10%. Theoretically, the dopant level can be increased to enhance the H_2 permeation flux. The Wagner permeation shows that the permeation flux is inversely proportional to the thickness of the membrane when permeation across the membrane is controlled by transport through the solid phase and not by boundary layer transport or by the activation of H_2 at membrane

surfaces. Therefore, the H_2 permeable membranes should be prepared as thin as possible in order to maximize the H_2 permeation flux. The thickness of the current $SrCe_{0.7}Zr_{0.2}Eu_{0.1}O_{3-\delta}$ tubular ceramic membrane reactor is between 25-30 microns. Since the membrane is coated on the tubular support via colloidal coating process, therefore the colloidal coating solutions (concentration, numbers of layer coated) can be adjusted in order to minimize the thickness of the membrane layer. In trying to adjust both the Eu dopant level, and the membrane thickness, other parameters, such as porosity of the porous layer, and the particle size of the $SrCe_{1-x}Eu_xO_{3-\delta}$ membrane may have to be adjusted to accommodate the change in the Eu dopant level and thickness in order to maintain the integrity of the tubular membrane reactor.

(3) Optimization of the integration of the Fe/SiO_2 catalyst and the $SrCe_{0.7}Zr_{0.2}Eu_{0.1}O_{3-\delta}$ tubular ceramic membrane reactor

Once the formulation of the membrane is optimized to maximize the H_2 flux, then the operating conditions such as, temperature, feed and sweep gas flowrates have to be optimized in tandem in order to maximize the CH_4 conversion and hydrocarbon product selectivity. For the CO_2 sweep study, the concentration of CO_2 in the sweep has be optimized. For the sweep side, the rate of synthesis gas production and the CO/H_2 ratio can be optimized. For the O_2 sweep gas study, the temperature and concentration of O_2 in the sweep gas have to be optimized in order to find the right conditions for autothermality.

Appendix A: Conversion and product selectivity calculation analysis in DNMC reaction

The quantification of reactant and products after the catalysis reaction was carried out in the gas chromatography (GC, Agilent 6890), as noted above, equipped with a (5%-Phenyl)-methylpolysiloxane capillary column (HP5-MS, 30.0 m x 0.25 mm x 0.25 μm) connected to a flame ionization detector (FID) and a packed column (ShinCarbon ST80/100 packed column, 2 m in length, 2 mm ID x 1/8" OD, Silco HP) connected to a thermal conductivity detector (TCD) was used to calibrate and separate the reactants and products. The typical settings in the GC instrument are shown in Table S1 below. The thermal conductivity detector was used to analyze C_2H_2, C_2H_4, C_2H_6, and CH_4; while the flame ionization detector was used to analyze the aromatics products (C_6H_6, C_7H_8, and $C_{10}H_8$), respectively. **Figure A1** shows a *representative* GC spectrum in the measurement.

Table A1. Typical settings of GC instrument for DNMC catalysis studies.

GC element	**Settings**
Inlet 1 (connected to capillary column and FID)	Temperature = 473 K; split ratio = 45; total flow rate = 24.9 mL·min^{-1}.
Inlet 2 (connected to packed column and TCD)	Temperature = 473 K; flow rate = 10 mL·min^{-1}.
Capillary Column	Flow rate = 0.5 mL·min^{-1}; Carrier gas = He.
Packed Column	Flow rate = 9 mL·min^{-1}; Carrier gas = He.
Oven program	Started from 313 K and held at this temperature for 5 min; ramp at 15 K·min^{-1} to 473 K and held at this temperature for 20 min; cooled to 313 K for next injection
FID detector	Temperature = 573 K; H_2 flow rate = 35 mL·min^{-1}; air flow rate = 350 mL·min^{-1}; make up flow rate = 34 mL·min^{-1}.

TCD detector	Temperature = 509 K; reference flow rate = 25 mL·min^{-1}; make up flow rate = 2 mL·min^{-1}.

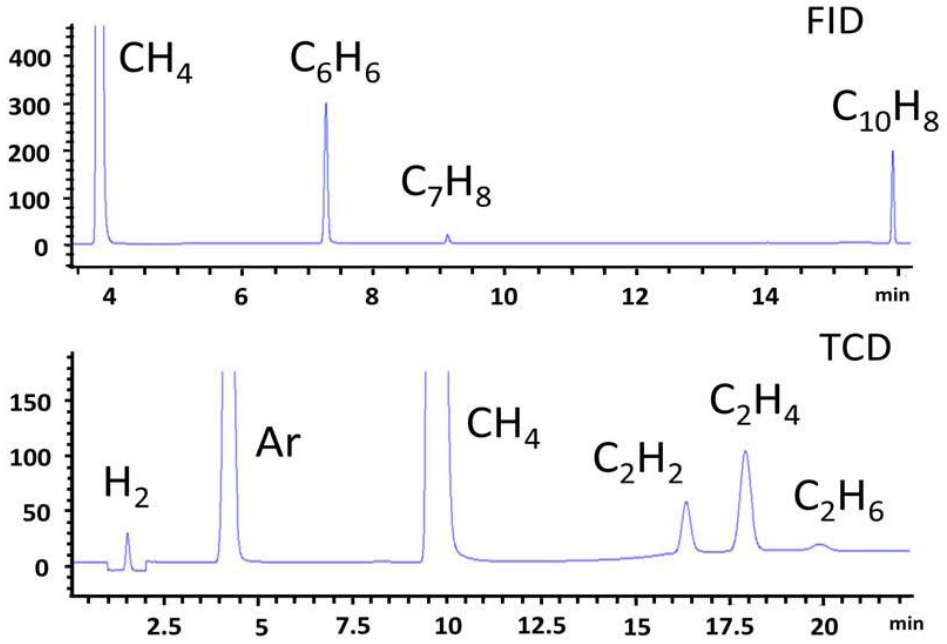

Figure A1. FID and TCD chromatography spectra for a typical experiment (*x*-axis has unit of min).

Calibration with internal standard Ar gas was run for all species (*i*) in order to determine the response factor (RF), where i = CH_4, C_2H_2, C_2H_4, C_2H_6, C_6H_6, C_7H_8, and $C_{10}H_8$. Then, based on the peak areas of each species (P_i), peak area of Ar (P_{Ar}), and flow rates of Argon (F_{Ar}), the flow rate for each species (F_i) in the effluent gas can be calculated according to the equation (1) below,

$$F_i = \frac{P_i}{R_i \times (\frac{P_{Ar}}{F_{Ar}})} \quad (1)$$

and methane conversion (X_{CH4}) was determined by the following equation (2).

$$X_{CH4} = \frac{(F_{CH4,in} - F_{CH4,out})}{F_{CH4,in}} \times 100 \quad (2)$$

The carbon balance can be evaluated by comparing both sides of the equation (2) below,

$$F_{CH4,in} - F_{CH4,out} = [2 \times (F_{C2H2} + F_{C2H4} + F_{C2H6})] + (6 \times F_{C6H6}) + (7 \times F_{C7H8}) + (7 \times F_{C10H8}) \quad (3)$$

The molecular selectivity (S_i) of each species can be calculated by the equation (4).

$$S_i = \frac{F_i}{\sum F_i} \times 100 \quad (4)$$

Below is an example of our analysis (**Table A2**) for the methane conversion using the analysis method listed above. We would like to note that two differences are observed in our reaction system compared to work reported by Bao and co-worker[55]: acetylene was one of our products and lower space velocity was required to reach comparable methane conversion and product selectivity.

Table A2. Exemplary analysis for methane conversion and product selectivity in DNMC reactions in the H_2-permeable membrane reactor (1303 K, space velocity of 3200 mL·g^{-1}·h^{-1}, He as sweep gas with a flow rate of 50 mL·min^{-1}).

Conversion and selectivity analysis based on GC measurement						
Bypass condition (FID)	Chemical type	CH_4				
	Peak area (picoAmp·s)	40855.5				
	Flow rate (x10^4, mol·min^{-1})	7.40923				
Bypass condition (TCD)	Chemical type	Ar	CH_4			
	Peak area (microVolt·s)	15503.7	100469.8			
	Flow rate (x10^4, mol·min^{-1})	0.821134	7.40923			
Reaction condition (FID)	Chemical type	CH_4 +C_2	Benzene	Toluene	Naphthalene	

	Peak area (picoAmp·s)	30416.9	2893.3	333.9	9014.4	
	Flow rate ($x10^4$, $mol \cdot min^{-1}$)	N/A	0.046705	0.0042104	0.0872699	
Reaction condition (TCD)	Chemical type	Ar	CH_4	C_2H_2	C_2H_4	C_2H_6
	Peak area (microVolt·s)	13462.7	68858.1	816.3	2569.6	197.4
	Flow rate ($x10^4$ $mol \cdot min^{-1}$)	0.821134	5.80278	0.043038	0.138787	0.0110218
Conversion and selectivity analysis	CH_4 conversion (based on reactant consumption)	X_{CH4} = (7.40923-5.80278)/7.40923 x 100% = 21.68 %				
	CH_4 conversion (based on production formation)	X_{CH4} = [2 x (0.043038 + 0.138787 + 0.0110218) + 6 x 0.046705 + 7 x 0.0042104 + 10 x 0.0872699]/7.40923 x 100% = 21.16 %				
	Carbon balance analysis	= (21.68% - 21.16%)/21.68% = 2.4% (*carbon balance within 5%)*				
	Product percentage selectivity	C_2H_2	C_2H_4	C_2H_6	Benzene	Toluene	Naphthalene
		13.0%	41.9%	3.3%	14.1%	1.3%	26.4%

Bibliography

1. Holmen, A., *Direct conversion of methane to fuels and chemicals.* Catalysis Today, 2009. **142**(1): p. 2-8.
2. Bruijnincx, P.C. and B.M. Weckhuysen, *Shale gas revolution: an opportunity for the production of biobased chemicals?* Angewandte Chemie International Edition, 2013. **52**(46): p. 11980-11987.
3. King, G.E. *Hydraulic fracturing 101: what every representative, environmentalist, regulator, reporter, investor, university researcher, neighbor and engineer should know about estimating frac risk and improving frac performance in unconventional gas and oil wells*. in *SPE hydraulic fracturing technology conference*. 2012. Society of Petroleum Engineers.
4. Dietl, N., M. Schlangen, and H. Schwarz, *Thermal hydrogen-atom transfer from methane: the role of radicals and spin states in oxo-cluster chemistry.* Angewandte Chemie International Edition, 2012. **51**(23): p. 5544-5555.
5. Mesters, C., *A selection of recent advances in C1 chemistry.* Annual Review of Chemical and Biomolecular Engineering, 2016. **7**: p. 223-238.
6. Pakhare, D. and J. Spivey, *A review of dry (CO_2) reforming of methane over noble metal catalysts.* Chemical Society Reviews, 2014. **43**(22): p. 7813-7837.
7. Wilhelm, D., et al., *Syngas production for gas-to-liquids applications: technologies, issues and outlook.* Fuel Processing Technology, 2001. **71**(1-3): p. 139-148.
8. Tian, P., et al., *Methanol to olefins (MTO): from fundamentals to commercialization.* ACS Catalysis, 2015. **5**(3): p. 1922-1938.
9. Unni, O., et al., *Conversion of methanol to hydrocarbons: how zeolite cavity and pore size controls product selectivity.* Angewandte Chemie International Edition, 2012. **51**(24): p. 5810-5831.
10. Olah, G.A., A. Goeppert, and G.S. Prakash, *Beyond oil and gas: the methanol economy*. 2011: John Wiley & Sons.
11. Spivey, J.J. and G. Hutchings, *Catalytic aromatization of methane.* Chemical Society Reviews, 2014. **43**(3): p. 792-803.
12. Horn, R. and R. Schlogl, *Methane activation by heterogeneous catalysis.* Catalysis Letters, 2015. **145**(1): p. 23-39.
13. Gueret, C., M. Daroux, and F. Billaud, *Methane pyrolysis: Thermodynamics.* Chemical Engineering Science, 1997. **52**(5): p. 815-827.
14. Alvarez-Galvan, M.C., et al., *Direct methane conversion routes to chemicals and fuels.* Catalysis Today, 2011. **171**(1): p. 15-23.
15. Gesser, H. and N. Hunter, *A review of C-1 conversion chemistry.* Catalysis Today, 1998. **42**(3): p. 183-189.

16. San Su, Y., J.Y. Ying, and W.H. Green Jr, *Upper bound on the yield for oxidative coupling of methane.* Journal of Catalysis, 2003. **218**(2): p. 321-333.

17. Wang, W. and Y. Lin, *Analysis of oxidative coupling of methane in dense oxide membrane reactors.* Journal of Membrane Science, 1995. **103**(3): p. 219-233.

18. Choudhary, T.V., E. Aksoylu, and D. Wayne Goodman, *Nonoxidative activation of methane.* Catalysis reviews, 2003. **45**(1): p. 151-203.

19. Holmen, A., O. Olsvik, and O. Rokstad, *Pyrolysis of natural gas: chemistry and process concepts.* Fuel Processing Technology, 1995. **42**(2-3): p. 249-267.

20. Khan, M. and B.L. Crynes, *Survey of recent methane pyrolysis literature.* Industrial & Engineering Chemistry, 1970. **62**(10): p. 54-59.

21. Holmen, A., O. Rokstad, and A. Solbakken, *High-temperature pyrolysis of hydrocarbons. 1. Methane to acetylene.* Industrial & Engineering Chemistry Process Design and Development, 1976. **15**(3): p. 439-444.

22. Holmen, A., O. Olsvik, and O.A. Rokstad, *Pyrolysis of natural gas: chemistry and process concepts.* Fuel Processing Technology, 1995. **42**(2): p. 249-267.

23. Olsvik, O. and F. Billaud, *Modelling of the decomposition of methane at 1273 K in a plug flow reactor at low conversion.* Journal of Analytical and Applied Pyrolysis, 1993. **25**: p. 395-405.

24. Ding, W., et al., *Methane Conversion to Aromatics on Mo/H-ZSM5: Structure of Molybdenum Species in Working Catalysts.* The Journal of Physical Chemistry B, 2001. **105**(2): p. 506-513.

25. Wang, L., et al., *Dehydrogenation and aromatization of methane under non-oxidizing conditions.* Catalysis Letters, 1993. **21**(1-2): p. 35-41.

26. Wang, D., J.H. Lunsford, and M.P. Rosynek, *Catalytic conversion of methane to benzene over Mo/ZSM-5.* Topics in Catalysis, 1996. **3**(3-4): p. 289-297.

27. Borry, R.W., et al., *Structure and density of Mo and acid sites in Mo-exchanged H-ZSM5 catalysts for nonoxidative methane conversion.* The Journal of Physical Chemistry B, 1999. **103**(28): p. 5787-5796.

28. Andersen, A., et al., *Hydrogen acceptor and membrane concepts for direct methane conversion.* Catalysis Today, 1989. **4**(3-4): p. 389-397.

29. Hamakawa, S., T. Hibino, and H. Iwahara, *Electrochemical hydrogen permeation in a proton-hole mixed conductor and its application to a membrane reactor.* Journal of the Electrochemical Society, 1994. **141**(7): p. 1720-1725.

30. Borry III, R.W., et al., *Non-oxidative catalytic conversion of methane with continuous hydrogen removal*, in *Studies in surface science and catalysis*. 1998, Elsevier. p. 403-410.

31. Liu, Z., L. Li, and E. Iglesia, *Catalytic pyrolysis of methane on Mo/H-ZSM5 with continuous hydrogen removal by permeation through dense oxide films.* Catalysis Letters, 2002. **82**(3-4): p. 175-180.

32. Hamakawa, S., T. Hibino, and H. Iwahara, *Electrochemical methane coupling using protonic conductors.* Journal of the Electrochemical Society, 1993. **140**(2): p. 459-462.

33. Hamakawa, S., et al., *Synthesis and hydrogen permeation properties of membranes based on dense $SrCe_{0.95}Yb_{0.05}O_{3-\alpha}$ thin films.* Solid State Ionics, 2002. **148**(1-2): p. 71-81.

34. Cao, Z., et al., *Natural gas to fuels and chemicals: improved methane aromatization in an oxygen-permeable membrane reactor.* Angewandte Chemie International Edition, 2013. **52**(51): p. 13794-13797.

35. Morejudo, S.H., et al., *Direct conversion of methane to aromatics in a catalytic co-ionic membrane reactor.* Science, 2016. **353**(6299): p. 563-566.

36. Liu, Y., X. Tan, and K. Li, *Nonoxidative methane coupling in a $SrCe_{0.95}Yb_{0.05}O_{3-\alpha}$ (SCYb) hollow fiber membrane reactor.* Industrial & Engineering Chemistry Research, 2006. **45**(11): p. 3782-3790.

37. Xue, J., et al., *Gas to liquids: natural gas conversion to aromatic fuels and chemicals in a hydrogen-permeable ceramic hollow fiber membrane reactor.* ACS Catalysis, 2016. **6**(4): p. 2448-2451.

38. Sakbodin, M., et al., *Hydrogen-Permeable Tubular Membrane Reactor: Promoting Conversion and Product Selectivity for Non-Oxidative Activation of Methane over an Fe©SiO_2 Catalyst.* Angewandte Chemie International Edition, 2016. **128**(52): p. 16383-16386.

39. Csicsery, S.M., *Shape-selective catalysis in zeolites.* Zeolites, 1984. **4**(3): p. 202-213.

40. Flanigen, E.M., *A review and new perspectives in zeolite crystallization in molecular sieves.* 1973, American Chemical Society. p. 119-139.

41. Ma, Y., et al., *A review of zeolite-like porous materials.* Microporous and Mesoporous Materials, 2000. **37**(1): p. 243-252.

42. Vermeiren, W. and J.-P. Gilson, *Impact of zeolites on the petroleum and petrochemical industry.* Topics in Catalysis, 2009. **52**(9): p. 1131-1161.

43. Marcilly, C., *Evolution of refining and petrochemicals: what is the place of zeolites.* Oil & Gas Science and Technology, 2001. **56**(5): p. 499-514.

44. Kulprathipanja, S., *Zeolites in industrial separation and catalysis*. 2010: John Wiley & Sons.

45. Tanabe, K. and W.F. Hölderich, *Industrial application of solid acid–base catalysts.* Applied Catalysis A: General, 1999. **181**(2): p. 399-434.

46. Rabo, J.A. and M.W. Schoonover, *Early discoveries in zeolite chemistry and catalysis at Union Carbide, and follow-up in industrial catalysis.* Applied Catalysis A: General, 2001. **222**(1-2): p. 261-275.

47. Zhang, C.-L., et al., *Aromatization of methane in the absence of oxygen over Mo-based catalysts supported on different types of zeolites.* Catalysis Letters, 1998. **56**(4): p. 207-213.

48. Liu, S., et al., *Bifunctional catalysis of Mo/HZSM-5 in the dehydroaromatization of methane to benzene and naphthalene XAFS/TG/DTA/MASS/FTIR characterization and supporting effects.* Journal of Catalysis, 1999. **181**(2): p. 175-188.

49. Zhang, W. and P.G. Smirniotis, *Dealuminated zeolite-based composite catalysts for reforming of an industrial naphthene-rich feedstock.* Applied Catalysis A: General, 1998. **168**(1): p. 113-130.

50. Weckhuysen, B.M., et al., *Conversion of methane to benzene over transition metal ion ZSM-5 zeolites: I. Catalytic characterization.* Journal of Catalysis, 1998. **175**(2): p. 338-346.

51. Weckhuysen, B.M., M.P. Rosynek, and J.H. Lunsford, *Characterization of surface carbon formed during the conversion of methane to benzene over Mo/H-ZSM-5 catalysts.* Catalysis Letters, 1998. **52**(1-2): p. 31-36.

52. Ding, W., et al., *Methane conversion to aromatics on Mo/H-ZSM5: structure of molybdenum species in working catalysts.* The Journal of Physical Chemistry B, 2001. **105**(2): p. 506-513.

53. Karakaya, C. and R.J. Kee, *Progress in the direct catalytic conversion of methane to fuels and chemicals.* Progress in Energy and Combustion Science, 2016. **55**: p. 60-97.

54. Taifan, W. and J. Baltrusaitis, *CH_4 conversion to value added products: potential, limitations and extensions of a single step heterogeneous catalysis.* Applied Catalysis B: Environmental, 2016. **198**: p. 525-547.

55. Guo, X., et al., *Direct, nonoxidative conversion of methane to ethylene, aromatics, and hydrogen.* Science, 2014. **344**(6184): p. 616-619.

56. Phair, J. and S. Badwal, *Review of proton conductors for hydrogen separation.* Ionics, 2006. **12**(2): p. 103-115.

57. Eichenauer, W., *FA Lewis: The palladium hydrogen system. Academic Press, London and New York 1967. 178 Seiten, 87 Abbildungen. Preis: 45 s.* Berichte der Bunsengesellschaft für physikalische Chemie, 1967. **71**(9-10): p. 1160-1161.

58. Yun, S. and S.T. Oyama, *Correlations in palladium membranes for hydrogen separation: a review.* Journal of Membrane Science, 2011. **375**(1-2): p. 28-45.

59. Rival, O., et al., *Oxygen-free methane aromatization in a catalytic membrane reactor.* Industrial & Engineering Chemistry Research, 2001. **40**(10): p. 2212-2219.

60. Wang, L., et al., *Production of ultra highly pure H_2 and higher hydrocarbons from methane in one step at mild temperatures and development of the catalyst*

under non-equilibrium reaction conditions. Chemical Communications, 2001(19): p. 1952-1953.

61. Larachi, F., et al., *Ru-Mo/HZSM-5 catalyzed methane aromatization in membrane reactors.* Catalysis Letters, 2002. **84**(3-4): p. 183-192.

62. Rogers, H., *Hydrogen embrittlement of metals: atomic hydrogen from a variety of sources reduces the ductility of many metals.* Science, 1968. **159**(3819): p. 1057-1064.

63. Collins, J.P., et al., *Catalytic dehydrogenation of propane in hydrogen permselective membrane reactors.* Industrial & Engineering Chemistry Research, 1996. **35**(12): p. 4398-4405.

64. Paglieri, S. and J. Way, *Innovations in palladium membrane research.* Separation and Purification Methods, 2002. **31**(1): p. 1-169.

65. Cheng, Y. and K. Yeung, *Palladium–silver composite membranes by electroless plating technique.* Journal of Membrane Science, 1999. **158**(1-2): p. 127-141.

66. Bryden, K.J. and J.Y. Ying, *Nanostructured palladium–iron membranes for hydrogen separation and membrane hydrogenation reactions.* Journal of Membrane Science, 2002. **203**(1-2): p. 29-42.

67. Fort, D., J. Farr, and I. Harris, *A comparison of palladium-silver and palladium-yttrium alloys as hydrogen separation membranes.* Journal of the Less Common Metals, 1975. **39**(2): p. 293-308.

68. Jun, C.-S. and K.-H. Lee, *Palladium and palladium alloy composite membranes prepared by metal-organic chemical vapor deposition method (cold-wall).* Journal of Membrane Science, 2000. **176**(1): p. 121-130.

69. Uemiya, S., et al., *Fabrication of thin palladium-silver alloy film by using electroplating technique.* Materials Transactions, 2007. **48**(5): p. 1119-1123.

70. Katoh, M., et al., *Characterization of palladium and palladium-silver alloy layers on stainless steel support.* International Journal Of Modern Physics B, 2006. **20**(25n27): p. 3866-3871.

71. Kreuer, K., *Proton-conducting oxides.* Annual Review of Materials Research, 2003. **33**(1): p. 333-359.

72. Fabbri, E., D. Pergolesi, and E. Traversa, *Materials challenges toward proton-conducting oxide fuel cells: a critical review.* Chemical Society Reviews, 2010. **39**(11): p. 4355-4369.

73. Nowick, A. and Y. Du, *High-temperature protonic conductors with perovskite-related structures.* Solid State Ionics, 1995. **77**: p. 137-146.

74. Li, J., H. Yoon, and E.D. Wachsman, *Hydrogen permeation through thin supported $SrCe_{0.7}Zr_{0.2}Eu_{0.1}O_{3-\delta}$ membranes; dependence of flux on defect equilibria and operating conditions.* Journal of Membrane Science, 2011. **381**(1-2): p. 126-131.

75. Zhang, K., et al., *Research progress and materials selection guidelines on mixed conducting perovskite-type ceramic membranes for oxygen production.* RSC Advances, 2011. **1**(9): p. 1661-1676.

76. Li, J., et al., *High temperature $SrCe_{0.9}Eu_{0.1}O_{3-\delta}$ proton conducting membrane reactor for H2 production using the water–gas shift reaction.* Applied Catalysis B: Environmental, 2009. **92**(3-4): p. 234-239.

77. Uchida, H., N. Maeda, and H. Iwahara, *Relation between proton and hole conduction in $SrCeO_3$-based solid electrolytes under water-containing atmospheres at high temperatures.* Solid State Ionics, 1983. **11**(2): p. 117-124.

78. Iwahara, H., et al., *Performance of solid oxide fuel cell using proton and oxide ion mixed conductors based on $BaCe_{1-x}Sm_xO_{3-\alpha}$.* Journal of the Electrochemical Society, 1993. **140**(6): p. 1687-1691.

79. Bonanos, N., K. Knight, and B. Ellis, *Perovskite solid electrolytes: structure, transport properties and fuel cell applications.* Solid State Ionics, 1995. **79**: p. 161-170.

80. Wu, J., et al., *Atomistic study of doped $BaCeO_3$: dopant site-selectivity and cation nonstoichiometry.* Chemistry of Materials, 2005. **17**(4): p. 846-851.

81. Haile, S., G. Staneff, and K. Ryu, *Non-stoichiometry, grain boundary transport and chemical stability of proton conducting perovskites.* Journal of Materials Science, 2001. **36**(5): p. 1149-1160.

82. Wu, J., et al., *Defect chemistry and transport properties of $Ba_xCe_{0.85}M_{0.15}O_{3-\delta}$.* Journal of Materials Research, 2004. **19**(8): p. 2366-2376.

83. Davies, R., M. Islam, and J. Gale, *Dopant and proton incorporation in perovskite-type zirconates.* Solid State Ionics, 1999. **126**(3-4): p. 323-335.

84. Glöckner, R., M. Islam, and T. Norby, *Protons and other defects in $BaCeO_3$: a computational study.* Solid State Ionics, 1999. **122**(1-4): p. 145-156.

85. Buscaglia, M.T., et al., *Atomistic simulation of dopant incorporation in barium titanate.* Journal of the American Ceramic Society, 2001. **84**(2): p. 376-84.

86. Iwahara, H., T. Yajima, and H. Ushida, *Effect of ionic radii of dopants on mixed ionic conduction ($H^+ + O^{2-}$) in $BaCeO_3$-based electrolytes.* Solid State Ionics, 1994. **70**: p. 267-271.

87. Sammells, A.F., et al., *Rational selection of advanced solid electrolytes for intermediate temperature fuel cells.* Solid State Ionics, 1992. **52**(1-3): p. 111-123.

88. Li, J., et al., *Stability of $SrCe_{1-x}Zr_xO_{3-\delta}$ under water gas shift reaction conditions.* Journal of the Electrochemical Society, 2010. **157**(3): p. B383-B387.

89. Iliuta, M.C., et al., *Methane nonoxidative aromatization over Ru-Mo/HZSM-5 in a membrane catalytic reactor.* Industrial & Engineering Chemistry Research, 2002. **41**(10): p. 2371-2378.

90. Iliuta, M.C., B.P.A. Grandjean, and F. Larachi, *Methane Nonoxidative Aromatization over Ru−Mo/HZSM-5 at Temperatures up to 973 K in a Palladium−Silver/Stainless Steel Membrane Reactor.* Industrial & Engineering Chemistry Research, 2003. **42**(2): p. 323-330.

91. Kinage, A.K., R. Ohnishi, and M. Ichikawa, *Marked enhancement of the methane dehydrocondensation toward benzene using effective Pd catalytic membrane reactor with Mo/ZSM-5.* Catalysis Letters, 2003. **88**(3-4): p. 199-202.

92. Natesakhawat, S., et al., *Improved benzene production from methane dehydroaromatization over Mo/HZSM-5 catalysts via hydrogen-permselective palladium membrane reactors.* Catalysis Science & Technology, 2015. **5**(11): p. 5023-5036.

93. Iliuta, M.C., B.P. Grandjean, and F. Larachi, *Methane nonoxidative aromatization over Ru−Mo/HZSM-5 at temperatures up to 973 K in a palladium−silver/stainless steel membrane reactor.* Industrial & Engineering Chemistry Research, 2003. **42**(2): p. 323-330.

94. Yoon, H., et al., *Fabrication of Thin-Film $SrCe_{0.9}Eu_{0.1}O_{3-\delta}$ Hydrogen Separation Membranes on Ni-$SrCeO_3$ Porous Tubular Supports.* Journal of the American Ceramic Society, 2009. **92**(8): p. 1849-1852.

95. Oh, T., et al., *Hydrogen permeation through thin supported $SrZr_{0.2}Ce_{0.8-x}Eu_xO_{3-\delta}$ membranes.* Journal of Membrane Science, 2009. **345**(1-2): p. 1-4.

96. Li, J., H. Yoon, and E.D. Wachsman, *Carbon dioxide reforming of methane in a $SrCe_{0.7}Zr_{0.2}Eu_{0.1}O_{3-\delta}$ proton conducting membrane reactor.* International Journal of Hydrogen Energy, 2012. **37**(24): p. 19125-19132.

97. Li, J.L., H. Yoon, and E.D. Wachsman, *Carbon dioxide reforming of methane in a $SrCe_{0.7}Zr_{0.2}Eu_{0.1}O_{3-\delta}$ proton conducting membrane reactor.* International Journal of Hydrogen Energy, 2012. **37**(24): p. 19125-19132.

98. DeAngelis, M.T., et al., *Sol-gel synthesis of nanocrystalline fayalite (Fe_2SiO_4).* American Mineralogist, 2012. **97**(4): p. 653-656.

99. Pakhare, D. and J. Spivey, *A review of dry (CO_2) reforming of methane over noble metal catalysts.* Chemical Society Reviews, 2014. **43**(22): p. 7813-7837.

100. Hickman, D.A. and L.D. Schmidt, *Production of Syngas by Direct Catalytic-Oxidation of Methane.* Science, 1993. **259**(5093): p. 343-346.

101. Ashcroft, A., et al., *Selective oxidation of methane to synthesis gas using transition metal catalysts.* Nature, 1990. **344**(6264): p. 319.

102. Gupta, M., M.L. Smith, and J.J. Spivey, *Heterogeneous catalytic conversion of dry syngas to ethanol and higher alcohols on Cu-based catalysts.* ACS Catalysis, 2011. **1**(6): p. 641-656.

103. Keller, G. and M. Bhasin, *Synthesis of ethylene via oxidative coupling of methane: I. Determination of active catalysts.* Journal of Catalysis, 1982. **73**(1): p. 9-19.

104. Lee, J.S. and S. Oyama, *Oxidative coupling of methane to higher hydrocarbons.* Catalysis Reviews Science and Engineering, 1988. **30**(2): p. 249-280.

105. Tonkovich, A.L., R.W. Carr, and R. Aris, *Enhanced C2 yields from methane oxidative coupling by means of a separative chemical reactor.* Science, 1993. **262**(5131): p. 221-223.

106. Ismagilov, Z.R., E.V. Matus, and L.T. Tsikoza, *Direct conversion of methane on Mo/ZSM-5 catalysts to produce benzene and hydrogen: achievements and perspectives.* Energy & Environmental Science, 2008. **1**(5): p. 526-541.

107. Wang, L.S., et al., *Dehydrogenation and aromatization of methane under nonoxidizing conditions.* Catalysis Letters, 1993. **21**(1-2): p. 35-41.

108. Wang, D.J., J.H. Lunsford, and M.P. Rosynek, *Catalytic conversion of methane to benzene over Mo/ZSM-5.* Topics in Catalysis, 1996. **3**(3-4): p. 289-297.

109. Li, L., R.W. Borry, and E. Iglesia, *Reaction-transport simulations of non-oxidative methane conversion with continuous hydrogen removal - homogeneous-heterogeneous reaction pathways.* Chemical Engineering Science, 2001. **56**(5): p. 1869-1881.

110. Caro, J., *Catalytic Membrane Reactors - Lab Curiosity or Key Enabling Technology?* Chemie Ingenieur Technik, 2014. **86**(11): p. 1901-1905.

111. Cao, Z.W., et al., *Natural Gas to Fuels and Chemicals: Improved Methane Aromatization in an Oxygen-Permeable Membrane Reactor.* Angewandte Chemie-International Edition, 2013. **52**(51): p. 13794-13797.

112. Iliuta, M.C., B.P.A. Grandjean, and F. Larachi, *Methane nonoxidative aromatization over Ru-Mo/HZSM-5 at temperatures up to 973 K in a palladium-silver/stainless steel membrane reactor.* Industrial & Engineering Chemistry Research, 2003. **42**(2): p. 323-330.

113. Li, L., R.W. Borry, and E. Iglesia, *Design and optimization of catalysts and membrane reactors for the non-oxidative conversion of methane.* Chemical Engineering Science, 2002. **57**(21): p. 4595-4604.

114. Rival, O., et al., *Oxygen-free methane aromatization in a catalytic membrane reactor.* Industrial & Engineering Chemistry Research, 2001. **40**(10): p. 2212-2219.

115. Liu, S.M., et al., *Methane coupling using catalytic membrane reactors.* Catalysis Reviews-Science and Engineering, 2001. **43**(1-2): p. 147-198.

116. Morejudo, S., et al., *Direct conversion of methane to aromatics in a catalytic co-ionic membrane reactor.* Science, 2016. **353**(6299): p. 563-566.

117. Weckhuysen, B.M., et al., *Conversion of methane to benzene over transition metal ion ZSM-5 zeolites - II. Catalyst characterization by x-ray photoelectron spectroscopy.* Journal of Catalysis, 1998. **175**(2): p. 347-351.

118. Wang, D.J., J.H. Lunsford, and M.P. Rosynek, *Characterization of a Mo/ZSM-5 catalyst for the conversion of methane to benzene.* Journal of Catalysis, 1997. **169**(1): p. 347-358.

119. Hamakawa, S.H., T.; Iwahara, H., *Electrochemical hydrogen permeation in a proton-hole mixed conductor snd its application to a membrane reactor.* Journal of Electrochemical Society , 1994. **141**(7): p. 1720-1725.

120. Kniep, J. and Y. Lin, *Effect of zirconium doping on hydrogen permeation through strontium cerate membranes.* Industrial & Engineering Chemistry Research, 2010. **49**(6): p. 2768-2774.

121. Qi, X. and Y. Lin, *Electrical conduction and hydrogen permeation through mixed proton–electron conducting strontium cerate membranes.* Solid State Ionics, 2000. **130**(1): p. 149-156.

122. Song, Y., et al., *A clue to exploration of the pathway of coke formation on Mo/HZSM-5 catalyst in the non-oxidative methane dehydroaromatization at 1073 K.* Applied Catalysis A: General, 2014. **482**: p. 387-396.

123. Wu, Y.Q., et al., *Spatial distribution and catalytic performance of metal-acid sites in Mo/MFI catalysts with tunable meso-/microporous lamellar zeolite structures.* Journal of Catalysis, 2015. **323**: p. 100-111.

124. Wu, Y.Q., et al., *Textural and catalytic properties of Mo loaded hierarchical meso-/microporous lamellar MFI and MWW zeolites for direct methane conversion.* Applied Catalysis A: General, 2014. **470**: p. 344-354.

125. Yoon, H., et al., *Fabrication of Thin-Film $SrCe_{0.9}Eu_{0.1}O_{3-\delta}$ Hydrogen Separation Membranes on Ni–$SrCeO_3$ Porous Tubular Supports.* Journal of the American Ceramic Society, 2009. **92**(8): p. 1849-1852.

126. Oh, T., et al., *Hydrogen permeation through thin supported $SrZr_{0.2}Ce_{0.8-x}Eu_xO_{3-\delta}$ membranes.* Journal of Membrane Science, 2009. **345**(1-2): p. 1-4.

127. Li, J., H. Yoon, and E. Wachsman, *Hydrogen permeation through thin supported $SrCe_{0.7}Zr_{0.2}Eu_{0.1}O_{3-\delta}$ membranes; dependence of flux on defect equilibria and operating conditions.* Journal of Membrane Science, 2011. **381**(1): p. 126-131.

128. Qiao, J., et al., *A review of catalysts for the electroreduction of carbon dioxide to produce low-carbon fuels.* Chemical Society Reviews, 2014. **43**(2): p. 631-675.

129. Cui, G., J. Wang, and S. Zhang, *Active chemisorption sites in functionalized ionic liquids for carbon capture.* Chemical Society Reviews, 2016. **45**(15): p. 4307-4339.

130. Daza, Y.A. and J.N. Kuhn, *CO_2 conversion by reverse water gas shift catalysis: comparison of catalysts, mechanisms and their consequences for CO_2 conversion to liquid fuels.* RSC Advances, 2016. **6**(55): p. 49675-49691.

131. Kawi, S., et al., *Progress in synthesis of highly active and stable nickel-based catalysts for carbon dioxide reforming of methane.* ChemSusChem, 2015. **8**(21): p. 3556-3575.

132. Kondratenko, E.V., et al., *Status and perspectives of CO_2 conversion into fuels and chemicals by catalytic, photocatalytic and electrocatalytic processes.* Energy & Environmental Science, 2013. **6**(11): p. 3112-3135.

133. Taheri Najafabadi, A., *CO_2 chemical conversion to useful products: an engineering insight to the latest advances toward sustainability.* International Journal of Energy Research, 2013. **37**(6): p. 485-499.

134. von der Assen, N., et al., *Life cycle assessment of CO_2 capture and utilization: a tutorial review.* Chemical Society Reviews, 2014. **43**(23): p. 7982-7994.

135. Du, X.L., et al., *Research progress on the indirect hydrogenation of carbon dioxide to methanol.* ChemSusChem, 2016. **9**(4): p. 322-332.

136. Jadhav, S.G., et al., *Catalytic carbon dioxide hydrogenation to methanol: a review of recent studies.* Chemical Engineering Research and Design, 2014. **92**(11): p. 2557-2567.

137. Wang, W., et al., *Recent advances in catalytic hydrogenation of carbon dioxide.* Chemical Society Reviews, 2011. **40**(7): p. 3703-3727.

138. Alvarez-Galvan, M., et al., *Direct methane conversion routes to chemicals and fuels.* Catalysis today, 2011. **171**(1): p. 15-23.

139. Wang, D., J.H. Lunsford, and M.P. Rosynek, *Characterization of a Mo/ZSM-5 catalyst for the conversion of methane to benzene.* Journal of Catalysis, 1997. **169**(1): p. 347-358.

140. Li, J., et al., *$SrCe_{0.7}Zr_{0.2}Eu_{0.1}O_3$-based hydrogen transport water gas shift reactor.* International Journal of Hydrogen Energy, 2012. **37**(21): p. 16006-16012.

141. Cao, Z., et al., *Natural gas to fuels and chemicals: improved methane aromatization in an oxygen-permeable membrane reactor.* Angewandte Chemie, 2013. **125**(51): p. 14039-14042.

142. Arndt, S., et al., *$Mn–Na_2WO_4/SiO_2$ as catalyst for the oxidative coupling of methane. What is really known?* Applied Catalysis A: General, 2012. **425**: p. 53-61.

143. Hou, K. and R. Hughes, *The kinetics of methane steam reforming over a Ni/α-Al_2O catalyst.* Chemical Engineering Journal, 2001. **82**(1-3): p. 311-328.

144. Yang, L., et al., *Highly efficient Ni/CeO_2-Al_2O_3 catalysts for CO_2 upgrading via reverse water-gas shift: Effect of selected transition metal promoters.* Applied Catalysis B: Environmental, 2018. **232**: p. 464-471.

145. Wolf, A., A. Jess, and C. Kern, *Syngas production via reverse water-gas-shift reaction over a Ni-Al_2O_3 catalyst: catalyst stability, reaction kinetics, and modeling.* Chemical Engineering & Technology, 2016. **39**(6): p. 1040-1048.

146. Oh, S.C., et al., *Direct non-oxidative methane conversion in a millisecond catalytic wall reactor.* Angewandte Chemie International Edition, 2019.

147. Katahira, K., et al., *Protonic conduction in Zr-substituted $BaCeO_3$.* Solid State Ionics, 2000. **138**(1-2): p. 91-98.

148. Ryu, K.H. and S.M. Haile, *Chemical stability and proton conductivity of doped $BaCeO_3$–$BaZrO_3$ solid solutions.* Solid State Ionics, 1999. **125**(1-4): p. 355-367.

149. Elvidge, C., et al., *A fifteen year record of global natural gas flaring derived from satellite data.* Energies, 2009. **2**(3): p. 595-622.

150. Oh, S.C., et al., *Catalytic consequences of cation and anion substitutions on rate and mechanism of oxidative coupling of methane over hydroxyapatite catalysts.* Fuel, 2017. **191**: p. 472-485.

151. Oh, S.C., et al., *Influences of cation and anion substitutions on oxidative coupling of methane over hydroxyapatite catalysts.* Fuel, 2016. **167**: p. 208-217.

152. Deckman, H.W., et al., *Electric power generation with heat exchanged membrane reactor*. 2007, US7217304B2.

153. Kniep, J., M. Anderson, and Y. Lin, *Autothermal reforming of methane in a proton-conducting ceramic membrane reactor.* Industrial & Engineering Chemistry Research, 2011. **50**(22): p. 12426-12432.

154. Brady, C., B. Murphy, and B. Xu, *Enhanced methane dehydroaromatization via coupling with chemical looping.* ACS Catalysis, 2017. **7**(6): p. 3924-3928.

155. Ma, S., et al., *Recent progress in methane dehydroaromatization: From laboratory curiosities to promising technology.* Journal of Energy Chemistry, 2013. **22**(1): p. 1-20.

156. Tessonnier, J.-P., et al., *Methane dehydro-aromatization on Mo/ZSM-5: About the hidden role of Brønsted acid sites.* Applied Catalysis A: General, 2008. **336**(1-2): p. 79-88.

157. Kosinov, N., et al., *Selective coke combustion by oxygen pulsing during Mo/ZSM-5-catalyzed methane dehydroaromatization.* Angewandte Chemie International Edition, 2016. **55**(48): p. 15086-15090.

158. Sun, C., et al., *Methane dehydroaromatization with periodic CH_4-H_2 switch: A promising process for aromatics and hydrogen.* Journal of Energy Chemistry, 2015. **24**(3): p. 257-263.

159. Xu, Y., et al., *The catalytic stability of Mo/HZSM-5 in methane dehydroaromatization at severe and periodic CH_4–H_2 switch operating conditions.* Chemical Engineering Journal, 2011. **168**(1): p. 390-402.

List of Publications

Journals:

1. Mann Sakbodin, Oh S.C., Liu D.* Direct Non-oxidative Methane Conversion in Membrane Reactor. *SPR Catalysis, Volume 30. RSC Advances, Book Chapter*, **2018**.
2. Mann Sakbodin, Wu, Y. Oh, S.C., Wachsman, E.D.*, Liu, D.* Hydrogen Permeable Tubular Membrane Reactor: Promoting Conversion and Product Selectivity for Non-oxidative Activation of Methane over Fe©SiO_2 Catalyst. *Angew. Chem. Int. Ed.,* **2016**, 128, 16383-16386
3. Mann Sakbodin, Oh, S.C., Wachsman, E.D.*, Liu, D.* Dual Production of Higher Hydrocarbons (C_2 and Aromatics) and Synthesis Gas via the Hydrogen-Permeable Tubular Membrane Reactor, *manuscript submitted to Nature Energy*
4. Mann Sakbodin, Schulman, E., Wachsman, E.D.*, Liu, D.* Autothermal Operation of the Direct Non-Oxidative Methane Conversion in a H_2-Permeable Membrane Reactor, *manuscript under preparation.*
5. Mann Sakbodin, Schulman, E., Wachsman, E.D.*, Liu, D.* Enhancement of the CH_4 conversion to C_{2+} hydrocarbons via the membrane reaction/separation system, *manuscript under preparation.*
6. Mann Sakbodin, Qin D., Oh S.C., Wu W., Liu D.* Hydroxyapatite Hollow Fiber Membranes for Oil-Water Separation, *manuscript under preparation.*
7. Huang Y.L., Pellegrinelli C, Mann Sakbodin, Wachsman E.D.* Molecular Reactions of O_2 and CO_2 on Ionically Conducting Catalyst. *ACS Catalysis*. **2018**, 8(2), 1231-1237.
8. Wu Y., Emdadi L., Oh S.C., Mann Sakbodin, Liu D.* Spatial distribution and catalytic performance of metal–acid sites in Mo/MFI catalysts with tunable meso-/microporous lamellar zeolite structures. *Journal of Catalysis*. **2015**, 323, 100-111.

Oral Presentation:

1. Mann Sakbodin, Dongxia Liu, and Eric D. Wachsman. Tubular Ceramic Membrane Reactor for Non-oxidative Methane Reaction. 2015 AIChE Annual Meeting, Oral presentation, Salt Lake City, Utah, (November 8-13, **2015**).

Awards:

1. **The 2015 Harry K. Wells Graduate Fellowship** by the University of Maryland Energy Research Center (UMERC), provided a $20,000 one-year full-time graduate fellowship to pursue new research in the field of sustainable energy generation and/or storage

2. **The 2018 Sengers PhD Candidacy Graduate Scholarship**, an award recognition of top Ph.D. students by the Department of Chemical and Biomolecular Engineering at the University of Maryland